CRYSTAL GROWTH AND NEUTRON SCATTERING STUDIES OF HIGH TEMPERATURE SUPERCONDUCTORS

by

Zhijun Xu

A dissertation submitted to the Graduate Faculty in Physics
in partial fulfill ment of the requirements for the degree of
Doctor of Philosophy, The City University of New York

2011

This manuscript has been read and accepted for the
Graduate Faculty in Physics in satisfaction of the
dissertation requirements for degree of Doctor of Philosophy.

Prof. Jiufeng Tu

Date — Chair of Examing Committee

Prof. Steven Greenbaum

Date — Executive Office

Prof. Jiufeng Tu (CCNY)

Dr. John Tranquada (BNL)

Dr. Genda Gu (BNL)

Prof. Lia Krusin (CCNY)

Prof. Carlos Meriles (CCNY)

Supervisory Committee

THE CITY UNIVERSITY OF NEW YORK

Abstract

CRYSTAL GROWTH AND NEUTRON SCATTERING STUDIES OF HIGH TEMPERATURE SUPERCONDUCTORS

by

Zhijun Xu

Adviser: Prof. J. J. Tu, Dr. G. Gu and Dr. J. M. Tranquada

Since the discovery of the first high temperature superconductor in the 1980's, there have been continuing efforts to understand the mechanism of high-T_C superconductivity. Studies on the cuprate systems seem to suggest that there is an intimate relationship between superconductivity and magnetism, and recently this has also shown to be the case for the newly discovered Fe-based superconductors. Neutron scattering is a powerful tool for studying magnetism in superconductors, which can provide important information about the momentum and energy dependence of magnetic correlations.

The work presented in this thesis is divided into two main sections. Since high-quality large-size single crystals are necessary for the neutron scattering experiments. The first section is about sample preparation, where I will introduce single crystal growths via the Floating-zone technique as well as unidirectional solidification methods. The second section is neutron scattering experiments, which will show neutron scattering and transport measurements results in two high-temperature superconductor

systems: $La_{2-x}Ba_xCuO_4$ (LBCO), and $Fe_{1+y}Te_{1-x}Se_x$ (FeTeSe). In the LBCO system, we found that static magnetic order competes with bulk superconductivity. In addition, applying a magnetic field to or adding Zn impurities in the sample will enhance the static magnetic order and suppress the superconductivity. In the FeTeSe system, we found that spin resonance is associated with superconductivity, while resonance and superconductivity are simultaneously suppressed by an applied magnetic field or adding Fe impurities. Our results suggest that the magnetic correlations are important for the superconductivity, and proper tuning of these correlations may be a key for superconductivity.

Acknowledgements

I will first and foremost thank my advisors, Prof. J.J. Tu, Dr. Genda Gu and Dr. John M. Tranquada. Without them, I would not have been able to finish this dissertation, and their instructions and encouragements have proven to be invaluable. I also wish to thank other group members, Dr. Guangyong Xu, Dr. Jinsheng Wen, Dr. Igor Zaliznyak, Dr. Markus Hücker, Dr. Steve Shapiro and Dr. Liyuan Zhang, Dr. Andrei Savici, Kim Mohanty, Eward Stein, and Eileen Levine, whose help and support were essential during my hours in the lab.

I am also many thanks to professors in Physics Department, City University of New York and graduate center, City University of New York. Their education give me abundant physics knowledge.

I am grateful to the instrument scientists in the neutron research facilities, whose help was indispensable during my neutron scattering experiments: Dr. Jae-Ho Chuang, Dr. Hye-Jung Kang, Dr. Sung Chang, Dr. Ying Chen, Dr. William Ratcliff, Dr. Deepak Singh, Dr. Jason Gardner, Dr. Songxue Chi and Dr. Jeff Lynn at National Institute of Standards and Technology; and Dr. Andrey Zheludev, Dr. Tao Hong, Dr. Wei Tian, Dr. Jerel Zarestky, Dr. Matthew Stone, Dr. Eugene Mamontov, Dr. Garrett Granroth and Dr. Barry Winn at Oak Ridge National Laboratory.

I am also grateful to my collaborators in BNL and other facilities around the

world: Dr. Qiang Li's group, Dr. Qing Jie and Dr. Juan Zhou; Dr. P. Johnson's group, Dr. C. C. Homes; Dr. Weiguo Yin and Dr. Wei Ku in theory group ; Dr. P. Gehring and Dr. C. Stock at the National Institute of Standards and Technology; Prof. A. Yazdani's group at Princeton University; Prof. Seung-Hun Lee's group at the University of Virginia; Prof. Xingjiang Zhou's group at the Institute of Physics, Chinese Academy of Sciences; Prof. E. Hudson's group at Massachusetts Institute of Technology; Prof. A. Sacuto's group at Laboratoire Matériaux et Phénoménes Quantiques; Prof. J. Campuzano's group at the University of Chicago at Illinois; Prof. L. Greene's group at the University of Illinois at Urbana-Champaign; Prof. J. A. Yarmoff's group at the University of California at Riverside; Takeshi Kondo's group at Ames Laboratory.

Coming to a close, I would like to use this opportunity to thank all my friends in the United States. There are so many names that I cannot list them all here, but their companionship give me joy in my life away from home.

Last but not least, I am deeply grateful to my family. Their love and support give me strength and motivation in my work as well as my life. I dedicate this thesis to them.

Contents

List of Figures

List of Tables

Chapter 1

Introduction

In this Chapter, I will introduce the discovery, properties and applications of superconductivity, high-T_c cuprate superconductor and iron-based superconductor. I will also briefly introduce the BCS theory and the theory of high-T_c superconductivity, which focus on the interplay between superconductivity and magnetism.

1.1 Superconductivity

1.1.1 Discovery of superconductors

Superconductivity is a phenomenon, in which exactly zero electrical resistance occurs in certain materials. It was first observed in 1911 by H. K. Onnes, [1] who was studying the resistance of Mercury (Hg) in liquid helium. His group was the first ever to liquefy helium in 1908, making it a refrigerant that could reach the low temperatures of a couple degrees Kelvin (K). H. K. Onnes was awarded the Nobel Prize in Physics in 1913 "for his investigations on the properties of matter at low temperatures which led, inter alia, to the production of liquid helium". [36] Unlike

normal metals, in which electrical resistivity decreases gradually with cooling until tending to some residual resistance, Onnes' group found that Hg abruptly loses its resistance at 4.2 K [see Fig. 1.1(a)] and becomes a superconductor. The transition temperature, when resistance suddenly disappeared, is known as the critical temperature T_c. After Hg, a series of other elements, alloys, oxides, organic molecules, etc. have also been found to be superconductors.

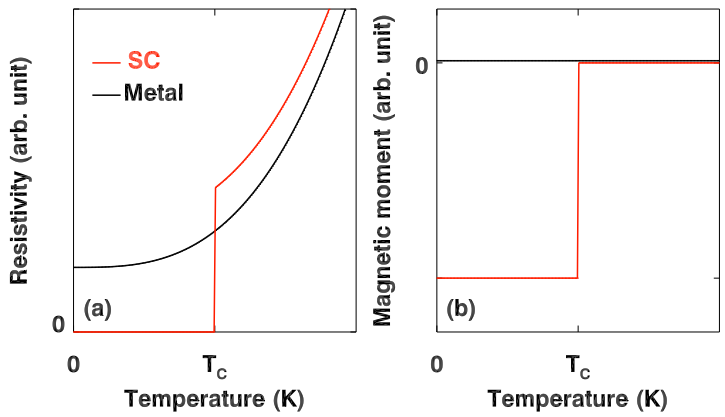

Figure 1.1: Schematic of transport measurements to determine T_c in superconductors: (a) Resistivity of superconductor (red) and normal metal (black) *vs* temperature. (b) Magnetization of superconductor (red) and normal paramagnetism (black) *vs* temperature.

Besides the lack of resistance, another characteristic of superconductivity is the "Meissner effect", discovered by W. Meissner and R. Ochsenfeld in 1933. [37] Super-

conductor can always expel the (not too strong, below H_c) applied magnetic fields completely (except for a very thin layer at the surface, penetrate depth λ_l). Therefore, superconductivity can not be understood simply as a classical perfect conductor that will keep a fixed magnetic flux since it loses electric resistivity regardless of the change in external field based on Maxwell's equations. The superconductor indeed act as a perfect diamagnet, which always creates magnetization in opposition to the applied field to cancel the interior field for temperature below T_c [see Fig. 1.1(b)]. The Meissner effect is so strong that a magnet can actually be levitated over a superconducting material. Besides practical applications for maglev devices, the Meissner effect also gives us an alternative way to measure the transition temperature of superconductors [see Fig. 1.1(b)].

1.1.2 High-T_c cuprate superconductors

For 75 years after the discovery of superconductivity, the highest T_c of conventional (elements, alloys) superconductors was still below 30 K (-243°C)(1986). In 1986, J. G. Bednorz and K. A. Müller discovered the first superconductor with T_c higher than 30 K: lanthanum barium copper oxide (LBCO). [5] J. G. Bednorz and K. A. Müller were awarded the Nobel Prize in Physics in 1987 "for their important break-through in the discovery of superconductivity in ceramic materials". [38] What made this discovery so remarkable is that the ceramic compounds usually do not conduct electricity well, and researchers had not considered them as possible high-temperature superconductor candidates before. This discovery of high-T_c (high relative to the predicted upper limit of T_c from BCS theory) superconductors aroused great interest in seeking new superconductors with higher T_c in oxide com-

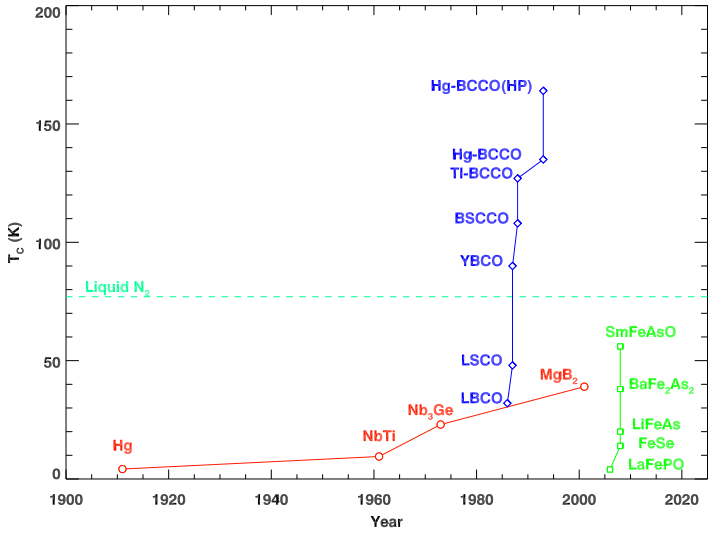

Figure 1.2: Historical record of superconductors. The convectional superconductor discovered since [1–4] (red). The high-T_c cuprate superconductors since 1986 (blue) for $La_{2-x}Ba_xCuO_4$ (LBCO) [5], $La_{2-x}Sr_xCuO_4$ (LSCO) [6], $YBa_2Cu_3O_7$ (YBCO) [7], $Bi_2Sr_2Ca_2Cu_3O_{10}$ (BSCCO) [8], $Tl_2Ba_2Ca_2Cu_3O_{10}$ (Tl-BCCO) [9], $HgBa_2Ca_2Cu_3O_8$ (Hg-BCCO) [10] and $HgBa_2Ca_2Cu_3O_8$ in high pressure (Hg-BCCO HP). [11] The iron-based superconductors (green) for LaFeOP [12, 13], $FeSe_xTe_{1-x}$ [14], LiFeAs [15], $BaFe_2As_2$ [16] $SmO_{1-x}F_xFeAs$. [17] The (teal) dash line indicate boiling point of liquid Nitrogen temperatures.

pounds, and a series of high-T_c superconductors [6–10] have been discovered since then [see Fig. 1.2]. The world record T_c at ambient pressure of 138 K is now held by $Hg_{0.8}Tl_{0.2}Ba_2Ca_2Cu_3O_{8.33}$. [39] The highest reported T_c of a superconductor is 164 K in a $HgBa_2Ca_2Cu_3O_{10}$ under quasihydrostatic pressures. [11]

The typical crystal structure of high-T_c superconductor is multi-layered perovskite structure [see Fig. 1.3 (a)]. This structure is quasi-two-dimensional and interplane coupling is weak. The common feature of these high-T_c superconductors is the copper-oxide (CuO_2) layers [see Fig. 1.3 (a)] and so they are known as cuprates. In the CuO_2 planes, squares of O^{2-} ions with a Cu^{2+} ion at the center of each square

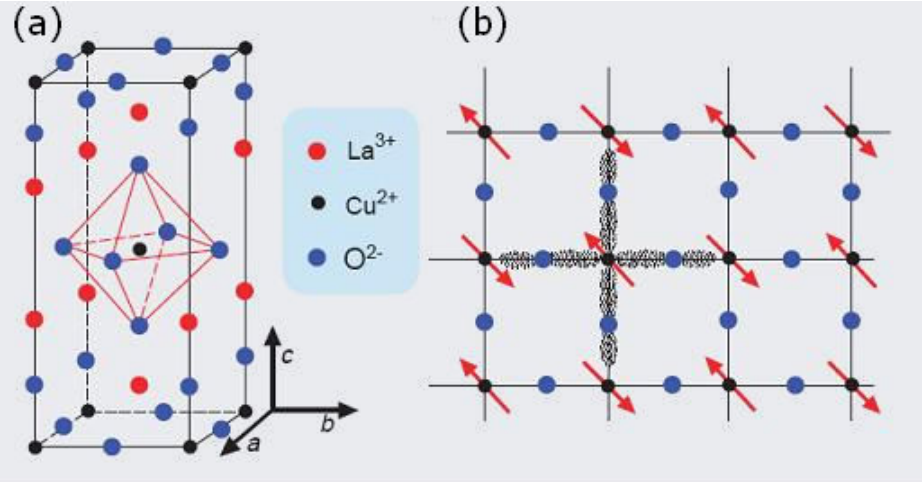

Figure 1.3: (a) Schematic of crystal structure of La_2CuO_4. (b) Schematic of copper-oxide plane. The red arrows indicate a possible alignment of spins in the antiferromagnetic ground state of La_2CuO_4. Fig. from Ref. [18]

form checkerboard lattices [see Fig. 1.3 (b)]. The layers of CuO_2 are believed to be the key structure in high-T_c superconductivity. Before the discovery of iron-based superconductors in 2008, most of ceramic high-T_c superconductors were cuprates.

1.1.3 Iron-based superconductors

In 2008, scientists discovered the first new high-temperature superconductors [12–17] containing Iron (Fe) instead of copper (Cu) and these superconductors are so called as iron-based superconductors. The first and well-known of these iron-based superconductors was $LaFeAsO_{1-x}F_x$, which has T_c about 26 K with x=0.11, and was discovered by H. Hosono group in 2008. [13] In 2006, a parent compound of the iron-based superconductor LaOFeP had been discovered by the H. Hosono group, [12] but as the T_c was only about 4 K, it did not garner much attention. The discovery of iron-based superconductors attracted great interest in searching for higher T_c su-

perconductors with similar compounds. The T_c soon after increased above 30 K by replacing La with other rare earth elements, [17, 40, 41] or under high pressure [13]. The highest record T_c of iron-based superconductor is 56 K in $Sr_{1-x}Sm_xFeAsF$ with x=0.5. [42]

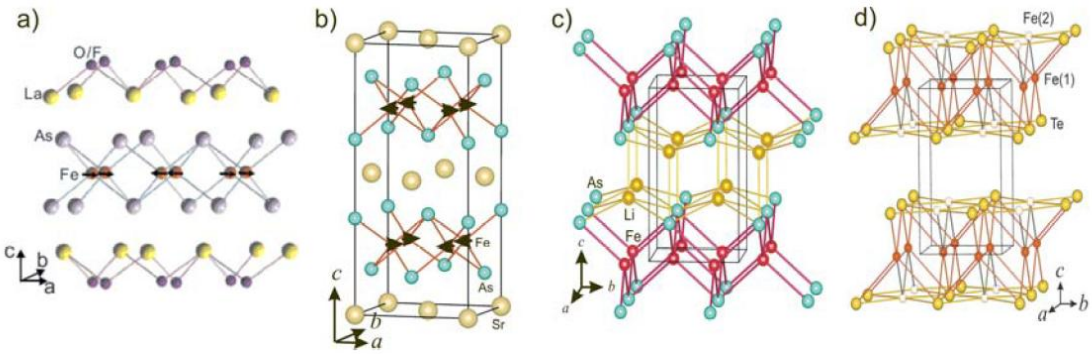

Figure 1.4: Schematic of crystal structure in a conventional unit cell [19] for (a) "1111" system, LaOFeAs. [13] (b) "122" system, $BaFe_2As_2$. [16] (c) "111" system, LiFeAs. [15] (d) "11" system, FeSe. Fig. from Ref. [14]

The RFeAsO (R=La,Ce,Pr,Nd,Gd,Sm) compound iron-based superconductors are commonly called "1111" systems because of the proportion of elements in their parent compounds. Besides the "1111" system, there are three other well-known iron-based superconductor systems: AFe_2As_2 (A=Ba,Sr,Ca) "122" system, [16, 43–45] BFeAs (B=Li,Na) "111" system [15, 46–49] and FeSe "11" system. [14, 50–53] The crystal structures of these system at room temperature are all tetragonal [15, 54–57], and are shown in Fig. 1.4. The common feature of these superconductors is the Fe^{2+} ions square-lattice layers [see Fig. 1.4], which is similar to copper-oxide layers in cuprate. The layered structure seems to be required for high T_c superconductors. The discovery of iron-based superconductors provides not only promising high-temperature superconductors systems, but also another source to study the mechanism of high-

temperature superconductors.

1.1.4 Applications of superconductors

The unique properties of superconductors are extremely conducive to applications. The zero energy loss of electric current flow in superconductors make superconductors the perfect transmitter of electric power. Replacing normal copper wires with superconducting wires will save tremendous amounts of energy that is usually lost in transmission as heat. On the other hand, superconducting magnets, without heat being generated in loops by an electric current, can be more powerful than conventional electromagnets. Strong superconducting magnets are used in Magnetic Resonance Imaging (MRI), [58] Nuclear Magnetic Resonance (NMR) machines, [59] and particle accelerators. Strong superconducting magnets are also used in magnetic levitation devices (as magnetic levitation trains), which take advantage of the Meissner effect of superconductors. Superconductors also play a role in magnetometers, power generators, electric motors, power storage devices and other instruments that bring great benefits to human life.

The discovery of high-T_c superconductors increase the potential applications of superconductors. Some superconductors with T_c higher than the boiling point of liquid Nitrogen (77 K) [see Fig. 1.2], are commercially advantageous since liquid N_2 is abundant and cheaper than liquid He and also need less cooling equipment. On the other hand, applications also benefit from the higher critical magnetic field and critical current in the high-T_c superconductors. However, even though a T_c at 160 K (-110 °C) is too cold for commercially practical use, the search for higher T_c superconductors has not ceased.

1.2 Theory of superconductivity

1.2.1 BCS theory

Either to search for new higher T_c superconductors or to develop new superconductor applications, it is essential to understand the mechanism of superconductivity. In 1957, J. Bardeen, L. N. Cooper and J. R. Schrieffer gave a quantitative explanation for many properties of superconductivity by their pairing theory. [60] Their theories became know as the BCS theory, which derived from the first letter of each man's last name. J. Bardeen, L. N. Cooper and J. R. Schrieffer were awarded the Nobel Prize in Physics in 1972 "for their jointly developed theory of superconductivity, usually called the BCS-theory". [61]

The key conceptual element in BCS theory involves Cooper pairs, in which electrons close to the Fermi level form pairs in the presence of an attractive potential. This pairing attraction was believed to lead to electron coupling with lattice vibrations (known as phonon interaction in BCS theory). Cooper pairs behave differently from single electrons, which is fermions that obey the Pauli exclusion principle. Cooper pairs act more like bosons, at sufficiently low temperatures, they form a (Bose-Einstein) condensation into same energy and momentum. The condensation of these electron pairs leaves a band gap in the order of meV, which inhibits the collision interactions that lead to ordinary resistivity. The BCS theory can also successfully explain the Meissner effect, heat capacity, penetration depth, critical magnetic field, and isotope effect in superconductors. [60]

The BCS theory works well for conventional low-temperature superconductors, such as elements and simple alloys, at temperatures close to absolute zero. However, the T_c in BCS theory is determined in terms of electron-phonon coupling, which is

too weak for T_c to be higher than 30 K. [**?**] Thus, experiments in high temperatures superconductors are beyond the capacity for BCS theory to explain, new or modified theories are essential to fully understand superconductivity.

1.2.2 Interplay between superconductivity and magnetism

One of the most promising new ideas is that electron pairing is magnetic in origin. Both experimental and theoretical evidence suggest that magnetism plays an important role in high-T_c superconductivity. High-T_c superconductors come from doping (replacing certain elements in intrinsic compounds) Mott insulators. [62] Unlike conventional insulator, conduction is blocked due to strong electron-electron repulsion and each electron is fixed in each unit cell in Mott insulator. [18] The spin of electrons have antiparallel alignment for nearest neighbor, which leads to long range antiferromagnetic order [see Fig. 1.3 (b)]. Doping restores conductivity by creating empty sites where electrons can jump without cost in Coulomb repulsion energy.

Schematic of typical phase diagram of the hole-doped, such as replacing La^{3+} by Sr^{2+}, cuprate superconductor is shown in Fig. 1.5. [18] The parent compound, where is undoped with x=0, is an antiferromagnet, which shows long-range antiferromagnetic order below Neel temperature T_N. [63] As the doping x increases, the long-range antiferromagnetic order is gradually suppressed, and the T_N rapidly decreases. Finally, the long-range antiferromagnetic order disappears and becomes short-range order spin glass . [64] When the doping x reaches certain level, superconductivity emerges. The relation of T_c and x typically shows a dome shape in phase diagram. Compounds where T_c increases with x increasing are under-doped. Compounds where T_c decreases with x increasing are over-doped. Optimal-doping occurs when T_c reaches

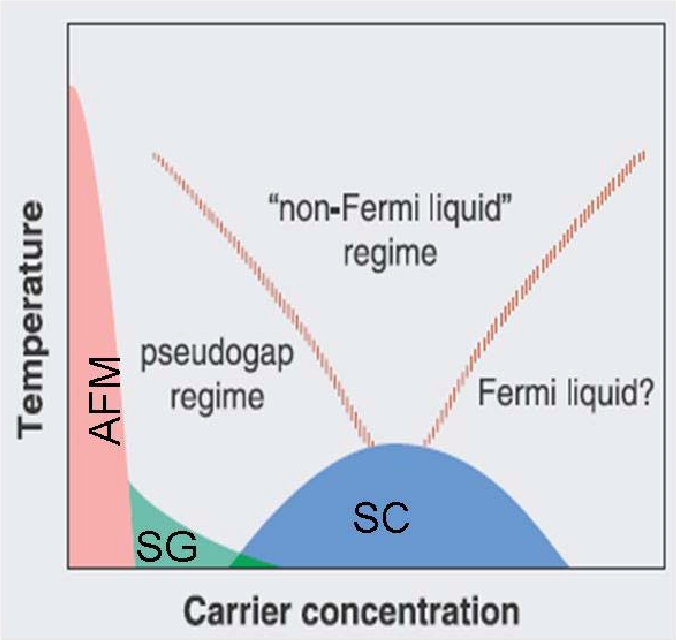

Figure 1.5: Phase diagram of the hole-doped cuprates compounds as a function of x and T. AFM, long-range antiferromagnetic order; SG, spin glass; SC, superconductivity. Upper curve is for separate some so called pseudogap, Fermi liquid and Non-Fermi liquid regions. Fig. from Ref. [18]

the maximum.

The newly discovered Fe-based superconductors have been shown to be the same case. [20, 21, 65] The experimentally determined phase diagram for $LaFeAsO_{1-x}F_x$ ("1111" system) and $Ba_{1-x}K_xFe_2As_2$ ("122" sytem) are shown in Fig. 1.6. [20, 21] The parent compounds of each system also have spin-density-wave (SDW) long range antiferromagnetic order. The long range magnetic order is suppressed with doping, while superconductivity starts to emerge after certain amount of doping. The superconductivity develops after the suppression of the long-range magnetic order, similar to what happen in the cuprates. Therefore the interplay between magnetism and

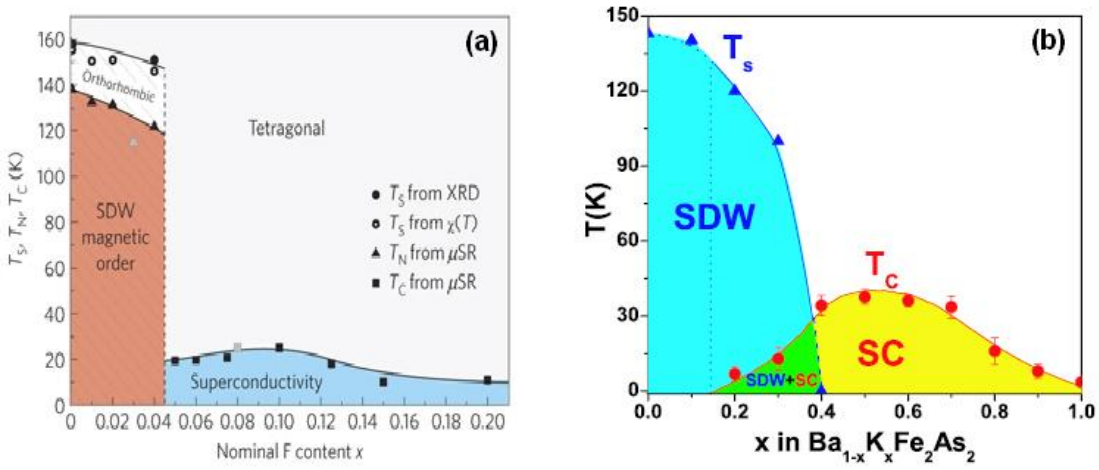

Figure 1.6: Experimentally determined phase diagram for iron-based superconductors (a) $LaFeAsO_{1-x}F_x$. Fig. from Ref. [20] (b) $Ba_{1-x}K_xFe_2As_2$. Fig. from Ref. [21] SDW, spin-density-wave antiferromagnetic order; SC, superconductivity.

superconductivity is a key issue in studies of high temperature superconductors.

1.2.3 Studying the magnetism in superconductor

To study the magnetic correlations in superconductors, neutron scattering is one of the most effective and direct probing techniques. However, large, good-quality single crystals are required for neutron scattering measurements, especially for inelastic magnetic measurements, because of the limit of neutron source and interactions. My thesis focuses on experiments studying the magnetic correlations in two superconductor systems: the $La_{2-x}Ba_xCuO_4$ and $Fe_{1+y}Te_{1-x}Se_x$ systems.

The thesis will be organized as following:

In Chapter 2, I will introduce our experimental methods , including detailed processes of single crystal growth using floating-zone technique and unidirectional solidification technique will be described. The neutron scattering techniques we used will

also be briefly introduced in this chapter.

In Chapter 3, I will show the experimental results in the $La_{2-x}Ba_xCuO_4$ system, which include Ba doping, Zn impurities, magnetic field effects on superconductivity, and magnetic "stripe" order and fluctuations in this system.

In Chapter 4, I will show the experimental results in $Fe_{1+y}Te_{1-x}Se_x$ system, including Se doping, Fe impurities, magnetic field effects on superconductivity, and magnetic correlations in this system. Detailed study of the parent compound FeTe will also be discussed in this Chapter.

Chapter 2

Experimental methods

In this chapter, I will show the single crystal growth of $La_{2-x}Ba_xCuO_4$ via floating zone technique and $Fe_{1+y}Te_{1-x}Se_x$ via unidirectional solidification technique. The theory and instruments of neutron scattering techniques will also be briefly discussed.

2.1 Crystal growth

For neutron scattering experiments, especially for inelastic magnetic scattering experiments to study the magnetic correlations, high quality large (order of gram magnitude) single crystals are necessary. Because of the limit of the flux of neutron sources and the weak interactions of magnetic scattering, only large single crystals can provide enough data in the limited beam time. However, growth of high quality large singles crystals is always a long-term challenge, especially in this case with $La_{2-x}Ba_xCuO_4$ (LBCO) single crystals, which were unavailable until 2004.

2.1.1 Growth of $La_{2-x}Ba_xCuO_4$ by Traveling-solvent floating-zone technique

We used the traveling-solvent floating-zone (TSFZ) technique [22, 66–68] to successfully grow a series of (x=0%∼15.5%) $La_{2-x}Ba_xCuO_4$ single crystals. The as-grow crystals have diameters of 6 to 8 mm and length above 20 cm [see Fig. 2.3 (a)]. [69] One advantage of the floating-zone technique is that no contamination occurs in growth, because of the floating-zone region only contacts with the rods of growth materials. Therefore we can avoid contamination, such as might come from crucibles, quartz and other containers in other crystals growth techniques. Another advantage of the floating-zone technique is that it is able to grow crystals with high melting points to sufficient lengths. This is important for the growth of $La_{2-x}Ba_xCuO_4$, where the real composition of doping deviates from nominal composition at the beginning of growth.

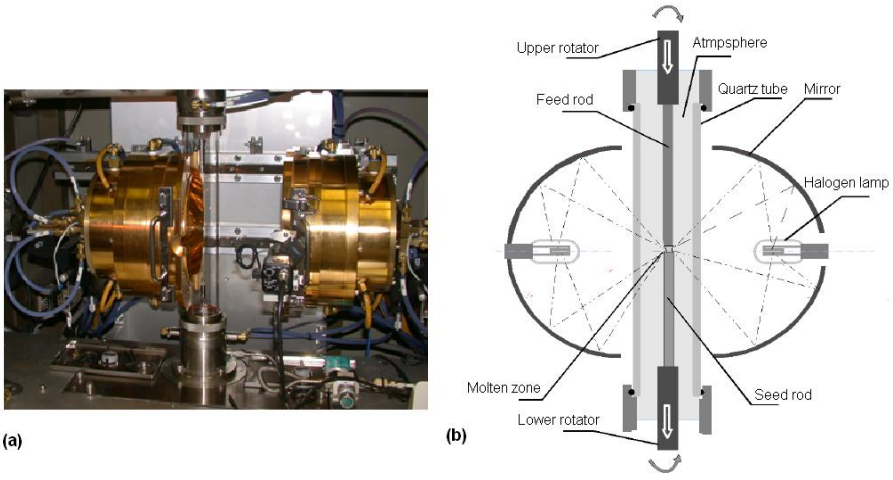

Figure 2.1: (a) The traveling-solvent floating-zone technique image furnace used in the growth of $La_{2-x}Ba_xCuO_4$. (b) Schematic of components of the TSFZ image furnace. Fig. from Ref. [22]

The image furnace we used to grow $La_{2-x}Ba_xCuO_4$ is shown in Fig. 2.1 (a) and a

schematic of the image furnace is shown in Fig. 2.1 (b). The infrared radiation furnace was equipped with two ellipsoidal mirrors as well as two (600 W, for $La_{2-x}Ba_xCuO_4$ growth) halogen lamps in the outer focus of the mirrors. The lights of both lamps were adjusted to focus at one point, the inner focus of both ellipsoidal mirrors. The floating zone in growth is typically in an hourglass shape and is held by surface tension between the feed and seed rods [Fig. 2.2 (a)]. The upper shaft and lower shaft hold the feed and seed rods separately, and during growth, rotates in the opposite direction, which stirs the floating zone to keep homogeneous growth conditions. The rods and floating zone are sealed in a quartz tube and the atmosphere in the tube is controlled to be certain pressure Oxygen for $La_{2-x}Ba_xCuO_4$ growth. In crystal growth, the upper and lower shafts move downwards together. Therefore the floating zone moves upwards on the feed rod and the feed rod gradually grows into a single crystal [see Fig. 2.2 (b)]. The final diameter of the crystal is determined by the diameter of the feed rod, and the ratio of the translation velocity of the feed and seed rods.

Before the growth in image furnace, we first needed to prepare the feed and seed rods, which are both $La_{2-x}Ba_xCuO_4$ polycrystals. To prepare the feed rod, La_2O_3, $BaCO_3$, and CuO (99.99%) in powder forms were mixed in stoichiometric ratios. The mixed powder was then ground in an agate mortar and calcined at 940 °C for 24 hours in air. The processes were repeated twice at 950 and 960 °C in order to obtain a homogeneous powder. This powder was put into a thin-wall rubber tube and compressed into cylindrical rods with about 6 mm diameter and 30 mm length under a hydrostatic pressure of 6 kbars. To avoid penetration of the molten liquid into the rod in growth, which would make the molten zone unhomogneous, extra CuO was added in order to obtain more tightly sintered feed rods and to compensate for evaporated Cu during floating-zone growth. Then we performed the sintering process

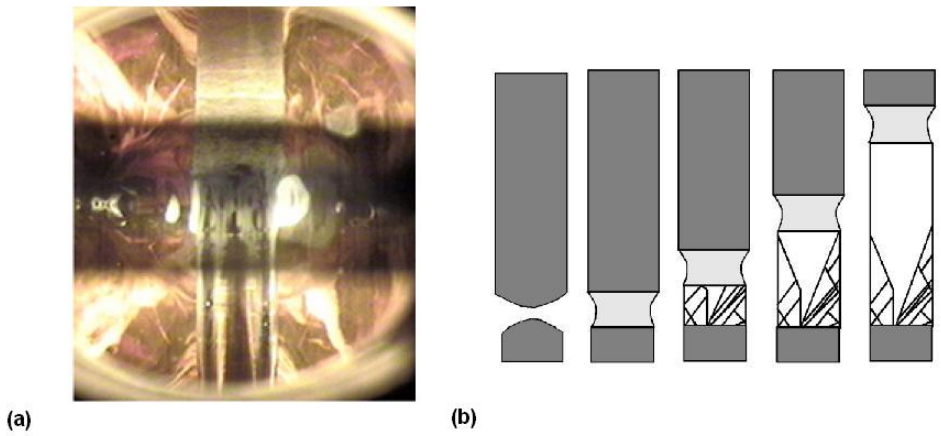

Figure 2.2: (a) Image of $La_{2-x}Ba_xCuO_4$ crystal rods in growth. (b) Schematic of the growth procedure on the feed and seed rods in TSFZ image furnace. Fig. from Ref. [22]

at the optimal sintering temperature for 48 hours in air. The amount of extra CuO to add and the temperature of optimal sintering depends on the doping x can be found in Table 2.1. There is a trend in Table 2.1 that the higher the Ba doping, the less extra CuO needed and the lower the sintering temperature. On the other hand, the seed rods were prepared in the same way as the feed rods.

At the start of growth in the image furnace, solvent (flux) is needed to help form the floating zone. We generally used $La_{2-x}Ba_xCu_4O_x$, raw materials that have rich Cu and low melting points. The solvent was compressed into cylindrical rods under a hydrostatic pressure of 4 kbars and sintered at 900 °C for 24 hours in air. After putting the feed and seed rods in the quartz tub, we adjusted the atmosphere in the quartz tub to Oxygen at the certain optimal pressure. The optimal Oxygen pressure depends on the doping x that can be found in Table 2.1. The higher the Ba doping, the higher Oxygen pressure is needed, with the highest in our image furnace system

Table 2.1: The growth conditions for $La_{2-x}Ba_xCu_{1+y}O_4$ system. Ba doping x, extra CuO y, sintering temperature T, Oxygen pressure P and transit temperature T_c.

Ba x (%)	Cu y (%)	T (°C)	P (bars)	T_c (K)
0	3	1260	1	
2	2	1260	2	
4	2	1260	2	
6	2	1260	4	
9.5	2	1260	11	32
11.5	1	1257.5	11	25
12.5	0.5	1255	11	2
13.5	0.5	1240	11	13
15.5	0	1225	11	30

being 11 bars. We first let the feed and seed rods rotate at low speeds in the same direction to build an hourglass-shaped floating zone as shown in Fig. 2.2 (a). Then we changed the rotation speeds of the two rods to 30 rpm and made them rotate in opposite directions. The feed seed rods moved downwards together at the same speed of 1 mm/hour during growth; total growth took 1-2 weeks. Throughout the entire growth procedure, the floating zone was kept stable to ensure homogeneous single crystal [see Fig. 2.2 (b)].

Sample characteristicsze

The as-grown crystal rod for $La_{2-x}Ba_xCuO_4$ (x=9.5%) is shown in Fig. 2.3 (a). The next step involved obtaining a homogeneous single crystal section from the rod for neutron scattering experiments. As shown in Fig. 2.2 (b), the crystals from the beginning of growth are small because of unstable growth condition. As growth continued, though, the [110] direction was found to be the fastest growth direction

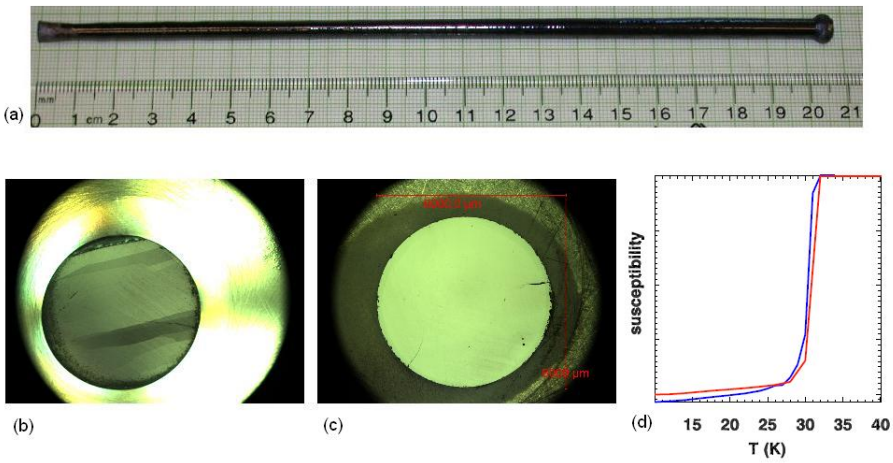

Figure 2.3: (a) The as-grown rod of $La_{2-x}Ba_xCuO_4$ crystal. Polished cross section of the rod at (b) starting part and (c) ending part of the growth under polarized light. (d) ZFC magnetization measurements by SQUID with a 5 Oe field perpendicular to the a-b plane.

for $La_{2-x}Ba_xCuO_4$. [66] The [110] orientation crystal gradually become larger and larger and finally become dominant [see Fig. 2.2 (b)]. To choose a homogeneous section, the quality of the crystal was checked by polarized light microscopes with linear-polarized light. We first polished the cross section to a roughness of 1 μm, like the smoothness of a mirror. If there were crystals with different orientations in the cross section, the refractive index would be different for different angles between the incident beams and optical axes of crystals. The differently orientated crystals show different color or brightness in the eyepiece, which is shown in Fig. 2.3 (b). To choose the single crystals for neutron scattering, we need a section of a crystal that in both faces has only one single domain crystal, as shown in Fig. 2.3 (c).

Besides the homogeneity in orientation, we also need the single crystal to have homogeneous composition. The real composition of doping mostly deviate from nominal composition at the start of the growth in $La_{2-x}Ba_xCuO_4$. The composition of

the crystals can be identified by measuring the transition temperature in the superconducting quantum interference device (SQUID). By comparing the transition temperature with the phase diagram obtained from the polycrystal samples, [25] we identified the exact compositions of the single crystals. The SQUID is a very sensitive magnetometer used to measure weak magnetic fields, based on superconducting loops containing Josephson junctions. The SQUID utilizes the Josephson effect to measure the current due to a small amount of quantum magnetic flux applied to the superconducting loop.

$$2I = 2\Delta\Phi/L \tag{2.1}$$

where L is the self inductance of the superconducting ring. The magnetization of the crystals were measured after zero-field-cooling (ZFC) and in the warming process in the field. Superconducting crystals with Meissner effect below T_c, show a large negative magnetization [see Fig. 2.3 (d)]. Moreover based on the width of the transition, we can roughly judge how homogeneous the composition of the crystal is. For a single crystal for neutron scattering, we need a section of single crystal that has sharp, correct T_c on both ends, as shown in Fig. 2.3 (d).

Before doing the neutron scattering experiment, we need to align the chosen section of single crystals. We use the back-reflection Laue mode X-ray diffraction [70] to check the crystal orientation. The camera is placed between the X-ray source and the crystal. The beams, which are diffracted in a backward direction from the crystal, are recorded. The back-reflection mode is useful if the sample is too thick for X-rays to transmit through it. As we know the crystal structure of $La_{2-x}Ba_xCuO_4$, we can identify the diffracting planes and normal orientation in the crystals by analyzing the back reflection patterns in Laue photograph. Then we can rotate the crystals

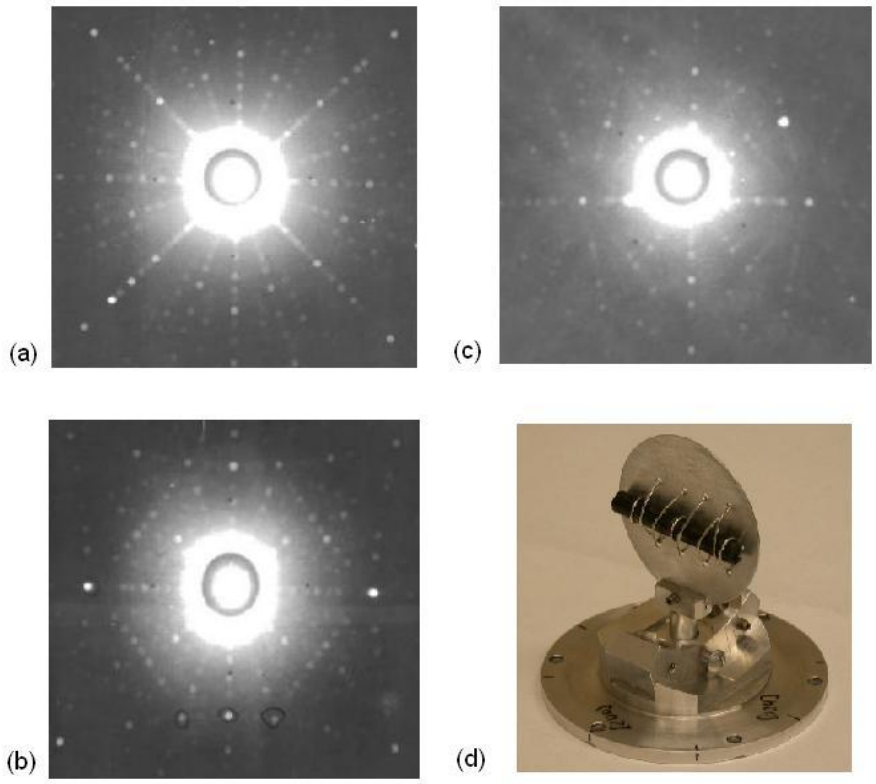

Figure 2.4: The Laue back reflection picture for incident beam along (a) [001], (b) [100] and (c) [110] directions. (d) The aligned crystal mounted on a Brookhaven designed super goniometer for neutron scattering.

to desired orientation with X-ray as shown in Fig. 2.3 (a-c). Finally, we mounted this section of single crystal on a Brookhaven designed super goniometer as shown in Fig. 2.3 (d), which has three rotational degrees of freedom to align the crystal in the direction we want.

2.1.2 Growth of $Fe_{1+y}Te_{1-x}Se_x$ by Unidirectional solidification technique

Unidirectional solidification technique is a crystal growth method that allows molten alloy to solidify along a required direction by establishing a temperature gradient. The unidirectional solidification technique utilizes the principle that crystal grains grow along the opposite direction of the heat flow. For growth of $Fe_{1+y}Te_{1-x}Se_x$ system, Te, Se (99.999%) and Fe (99.98%) grains were mixed in stoichiometric compositions in their metal ratios as raw materials. Then the raw materials were sealed in vacuum in two layers of quartz tubes. The quartz tubes were put in the furnace nearly horizontal and a temperature gradient would applied along the tube at high temperature. The furnace was then heated up to 660 °C and stayed there for 12 hrs; then heated to 900 °C and stayed there for 12 hrs, and heated to 1050 °C and stayed for 12 hrs for fully melting. At 1050 °C, when all raw materials had melted, the quartz tubes were rocked for 3 hrs to make the molten materials homogeneous. The furnace later cooled to 930 °C in 0.5 hrs, and then cooled with a cooling rate of 1 °C/hour until 300 °C. Finally, the tubes were cooled to room temperature and were taken out of the furnace. Large high quality single crystals were found in the as-grown rods. [see Fig. 2.5 (a)].

Using unidirectional solidification methods, we successfully grew a series of (x=0%$\sim$ 70% and y=0%$\sim$ 13%) $Fe_{1+y}Te_{1-x}Se_x$ single crystals above 10 g [see Fig. 2.5 (b)] We had also tried floating-zone and Bridgman methods to grow $FeTe_{1-x}Se_x$, but as-grown crystals were unsatisfactory because the abnormal expansion in cooling in the $FeTe_{1-x}Se_x$ system would make the growth unstable. The sample characterizations of $Fe_{1+y}Te_{1-x}Se_x$ by microscope and SQUID are similar to $La_{2-x}Ba_xCuO_4$ as shown

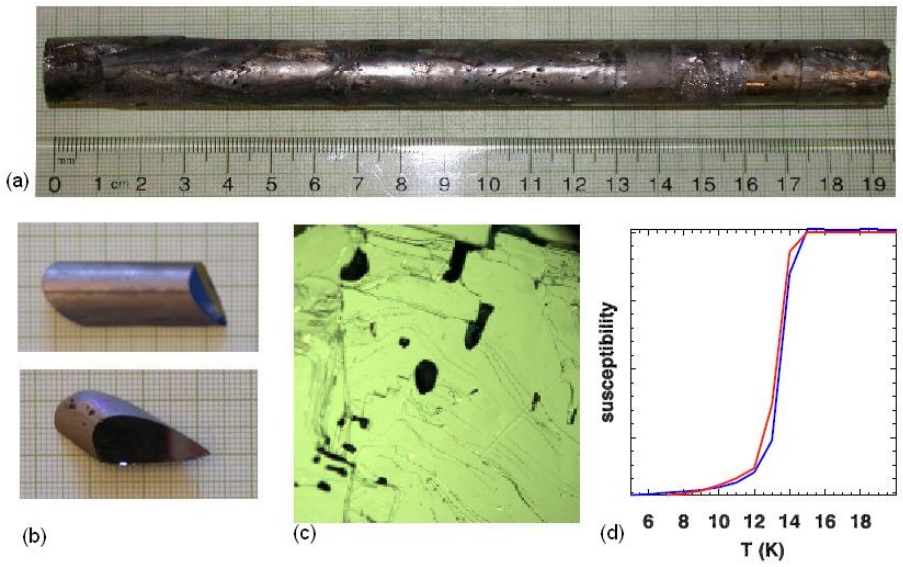

Figure 2.5: (a) The as-grown rod of $Fe_{1+y}Te_{1-x}Se_x$ crystal. (b) Some section of $Fe_{1+y}Te_{1-x}Se_x$ single crystals used for neutron scattering. (c) Cleaved crystal surface under polarized light.

in Fig. 2.5 (c-d). Unlike $La_{2-x}Ba_xCuO_4$, the $Fe_{1+y}Te_{1-x}Se_x$ single crystals have nice cleavage surfaces [see Fig. 2.5 (b)] , which are found to be the *ab*-plane. Therefore, we can simply align the crystals by eye instead of Laue X-ray measurements sometime.

2.2 Neutron scattering

2.2.1 Theory of Neutron scattering

Neutron is a powerful probe for studying condensed matters. Several properties of neutron are listed in Table 2.2, [23, 71, 72] These properties give neutrons many advantages in studying material properties. Firstly, the mass of neutron is similar to Hydrogen atom, so the neutron energy can be moderated by collisions with hydrogen or deuterium. The median energy of moderated neutron beam is proportional to

the temperature of moderating medium, which can be easily adjusted. Secondly, the zero net charge of neutron allows it to penetrate deeply into the sample to probe the bulk properties, where neutrons pass through electronic cloud to interact with atomic nuclei in very short range (fm). In addition, it also allows neutrons to penetrate the sample enclosure used to control the environment. Last but not least, neutrons have a magnetic moment which can interact with unpaired electron spins in a material. Furthermore neutrons have comparable wavelength as lattice constants and comparable kinetic energy as atoms in a solid. Therefore, neutron scattering is a perfect tool in studying the magnetic correlations and excitations in magnetic matter.

Table 2.2: Properties of neutron.

Rest mass, m_n	1.675×10^{-27} kg
charge	0
spin	1/2
magnetic moment, μ_n	1.913 nuclear magnetons
Wavelength,$\lambda[\mathring{A}]$	$9.044/\sqrt{E(meV)}$
Wave vector,$k[\mathring{A}^{-1}]$	$\sqrt{E(meV)}/2.072$

Before further discussing, it is useful to establish the notations in typical high-T_C cuprates and iron-based superconductors. As shown in Fig. 2.6 (a), a tetragonal unit cell in the ab plane is indicated by the Cu-O-Cu bond, with lattice constants $a = b \approx$ 3.81 Å. The corresponding Brillouin zone in reciprocal space is defined by two vector $[H00]$ and $[0K0]$ as shown in Fig. 2.6 (c). In reciprocal space, the general wave vector **Q**=(h, k, l) is in reciprocal lattice units (r.l.u.) of $(a^*, b^*, c^*) = (2\pi/a, 2\pi/b, 2\pi/c)$. In the parent compound, spins on neighboring Cu atoms (S=1/2) are antiparallel to each other as shown in Fig. 2.6 (b). The antiferromagnetic order causes the magnetic

unit cell to be double the size of lattice unit cell in the plane. Because the spins have a periodicity of 2 unit lattice in real space, the magnetic Bragg peak is at wave vector $\mathbf{Q}_{AF}$=(1/2,1/2) in reciprocal space. The antiferromagnetic Brillouin zone is half of lattice Brillouin zone as shown in Fig. 2.6 (c).

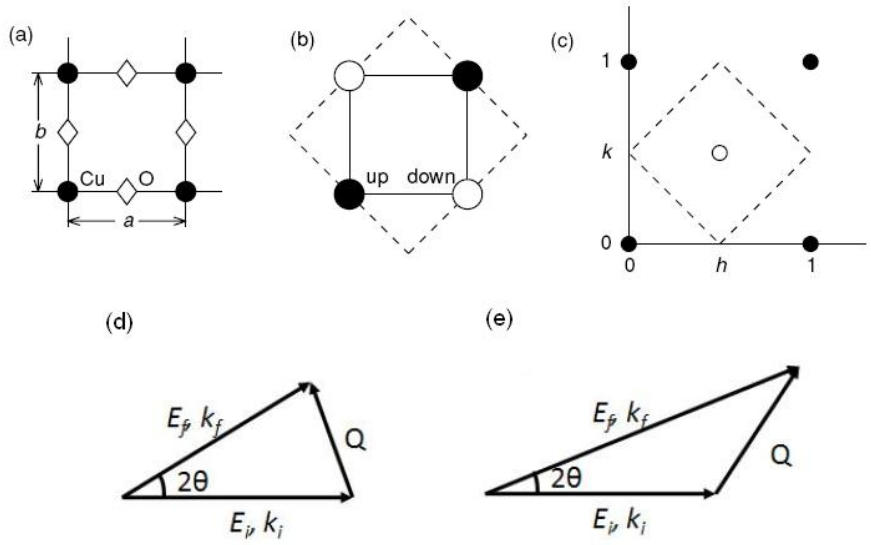

Figure 2.6: Schematic of (a) CuO2 plane, indicating positions of the Cu and O atoms and the lattice parameters, a and b. (b) Antiferromagnetic order of Cu moments, with filled (empty) circles representing up (down) spins. Solid line indicates the square lattice unit cell; dashed line denotes the magnetic unit cell. (c) Reciprocal space (hk0) plane. Filled circles: Bragg peak positions corresponding to the lattice. Empty circle: magnetic Bragg peak due to antiferromagnetic order. Dashed line indicates the antiferromagnetic Brillouin zone. (d) vector diagram of elastic scattering, and (e) inelastic scattering. Fig. from Ref. [23, 24]

Neutrons are nuclear particle with both wave and particle-like properties. The wavelength λ and wave vector $k = 2\pi/\lambda$ can be derived from its energy.

$$E = \frac{(\hbar k)^2}{2m_n} \tag{2.2}$$

Where $\hbar$ is Plank's constant divided by 2π, m_n is the mass of neutron. The neutron scattering is governed by the law of energy and momentum conservation.

$$\hbar\omega = E_i - E_f \tag{2.3}$$

$$\mathbf{Q} = \mathbf{k}_f - \mathbf{k}_i \tag{2.4}$$

Where ω is 2π times frequency, E_i, $\mathbf{k}_i$ refer to initial energy, momentum and E_f, $\mathbf{k}_f$ refer to final energy, momentum of neutrons. Then $\hbar\omega$ is the energy transferred to crystal, the momentum transferred to the crystal is $\hbar\mathbf{Q}$. When $\hbar\omega$=0 the scattering is elastic as shown in Fig. 2.6 (d). When $\hbar\omega \neq 0$ the scattering is inelastic. $\hbar\omega > 0$, neutron energy loss, while $\hbar\omega < 0$, neutron energy gain as shown in Fig. 2.6 (e).

In elastic situation, $|\mathbf{k}_i| = |\mathbf{k}_f|$=k. The conservation of momentum in Fig. 2.6 (d) give:

$$\mathbf{Q} = 2k \sin\theta, \tag{2.5}$$

where θ is half the angle between $\mathbf{k}_i$ $\mathbf{k}_f$. When the scattering meet the Bragg condition:

$$2d \sin\theta = \lambda, \tag{2.6}$$

Since $k = 2\pi/\lambda$ and $|\mathbf{Q}|=|\mathbf{G}|$, where $\mathbf{G}$ is a reciprocal-lattice vector with $\mathbf{G}=2\pi/\mathrm{d}$, where d is the interplanar spacing. By adjust scattering angle θ, energy and direction of scattering neutrons are determined.

The differential scattering cross section of monoenergetic neutron can be obtained by Fermi's golden rule. The differential cross section of nuclear scattering can be

expressed as:

$$\frac{d^2\sigma}{d\Omega_f dE_f} = N\frac{k_f}{k_i}b^2 S(\mathbf{Q},\omega) \tag{2.7}$$

where N is the number of unit cells, b is the scattering length and $S(\mathbf{Q},\omega)$ is the the scattering function. An elegant way to write the scattering function was given by Van Hove:

$$S(\mathbf{Q},\omega) = \frac{1}{2\pi\hbar N}\int_{-\infty}^{\infty} dt\, e^{-i\omega t}\langle \rho_{\mathbf{Q}}(0)\rho_{-\mathbf{Q}}(t)\rangle \tag{2.8}$$

where the angle brackets, $\langle\cdots\rangle$ denote an average over configurations of time t and ρ_Q is the atomic density operator:

$$\rho_Q(t) = \sum_l e^{i\mathbf{Q}\dot{r}_l(t)} \tag{2.9}$$

The scattering function only depends on the the momentum and energy transferred from neutron to the sample, and give information both positions and motions of atoms in the sample. Therefore, measuring $S(\mathbf{Q},\omega)$ in neutron scattering experiment let us determine the microscopic properties of the system.

For elastic nuclear Bragg scattering in a Bravais lattice, the intensity I of Bragg peaks generalized to:

$$I(\mathbf{G}) \propto N|F_N(\mathbf{G})|^2 \tag{2.10}$$

where $F(\mathbf{Q})$, the static nuclear structure factor, is given by

$$F_N(\mathbf{G}) = \sum_j b_j e^{i\mathbf{G}\cdot\mathbf{d}_j} e^{-W_j} \tag{2.11}$$

where jth atom within the unit cell at position $\mathbf{d}_j$ with scattering length b_j and e^{-W_j} is the Debye-Waller factor. The crystal structure can be determined by measuring

structure factor at enough reflections.

Since the neutron has a magnetic dipole moment equals to $-\gamma\mu_N$, where γ=1.913 is the gyromagnetic ratio and μ_N is the nuclear magneton. Neutron can scatter from the magnetic moment of an atom via the dipole-dipole interaction. Therefore neutron scattering can be used to measure the magnetic structure. For unpolarized neutron scattering from a single species of magnetic atom, the differential cross section for magnetic scattering is given by

$$\frac{d^2\sigma}{d\Omega dE_f} = \frac{N}{\hbar}\frac{k_f}{k_i}p^2 e^{-2W} S(\mathbf{Q},\omega). \tag{2.12}$$

where p is amplitude for magnetic scattering and e^{-2W} is the Debye-Waller factor, and

$$p = (\frac{\gamma r_0}{2})gf(\mathbf{Q}) \tag{2.13}$$

where $r_0 = e^2/m_e c^2$ is the classical electron radius, g is the Landé factor (g=2 for net spin moment), $f(\mathbf{Q})$ is the magnetic form factor, which is the Fourier transform of normalized unpaired spin density $\rho_s(r)$,

$$f(\mathbf{Q}) = \int \rho_s(r) e^{i\mathbf{G}\cdot\mathbf{r}} d\mathbf{r} \tag{2.14}$$

The magnetic scattering function can be written as,

$$S(\mathbf{Q},\omega) = \sum_{\alpha,\beta}(\delta_{\alpha,\beta} - \mathbf{Q}_\alpha\mathbf{Q}_\beta/\mathbf{Q}^2)S^{\alpha\beta}(\mathbf{Q},\omega). \tag{2.15}$$

with,

$$S^{\alpha\beta}(\mathbf{Q},\omega) = \frac{1}{2\pi}\int_{-\infty}^{\infty} dt\, e^{-i\omega t}\sum_r e^{iQ\dot{r}}\langle S_o^\alpha(0) S_r^\beta(t)\rangle \tag{2.16}$$

Here $S_r^\beta(t)$ is the is the $\beta(= x, y, z)$ component of the component of the atomic spin at lattice site r and time t.

For elastic magnetic scattering from a magnetic ordered crystal, the intensity of magnetic Bragg peaks $I_M(\mathbf{G}_M)$ can be expressed by,

$$I_M(\mathbf{G}_M) \propto N_M |F_M(\mathbf{G}_M)|^2 \tag{2.17}$$

where N_M is the number of magnetic atoms and $F_M(\mathbf{G}_M)$ is the static magnetic structure factor, is given by

$$F_M(\mathbf{G}_M) = \sum_j p_j S_{\perp j} e^{i\mathbf{G}_M \cdot \mathbf{d}_j} e^{-W_j} \tag{2.18}$$

where jth magnetic atom within the unit cell at position $\mathbf{d}_j$ with magnetic scattering amplitude p_j, magnetic interaction vector $S_{\perp j}$, which is component of S perpendicular to $\mathbf{Q}$ and e^{-W_j} is the Debye-Waller factor. With crystal structure obtained above, the magnetic structure can be determined from the static magnetic structure factor.

On the other hand for inelastic scattering, $S(\mathbf{Q}, \omega)$ is related to the imaginary part of the dynamical spin susceptibility, $\chi''(\mathbf{Q}, \omega)$ via the fluctuation-dissipation theorem,

$$S(\mathbf{Q}, \omega) = \frac{\chi''(\mathbf{Q}, \omega)}{1 - e^{-\hbar\omega/k_B T}} \tag{2.19}$$

where $(1 - e^{-\hbar\omega/k_B T})^{-1}$ is referred as Bose factor, or detail-balance factor.

In summary, using neutron scattering experiment we can obtain information of lattice structure and magnetic structure as well as phonon and magnetic excitations in the crystals.

2.2.2 Instruments of Neutron scattering

Triple-axis

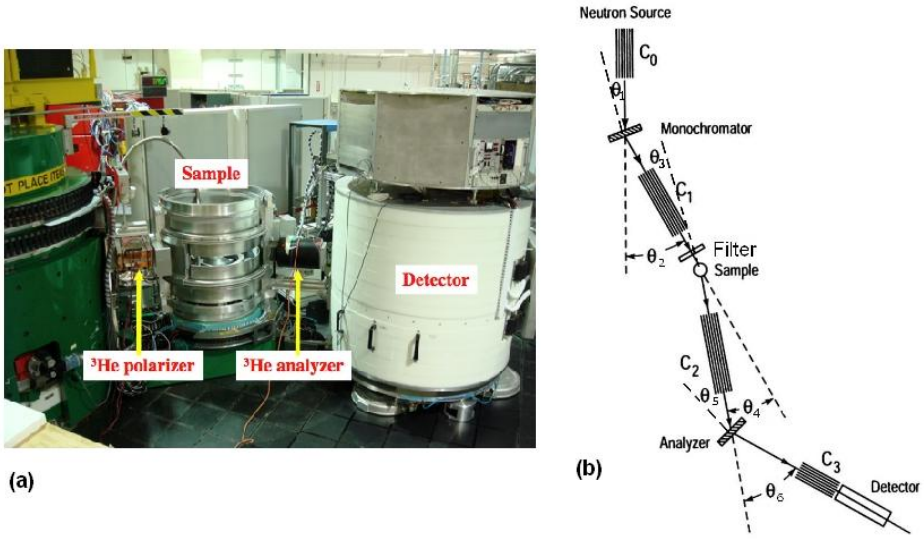

Figure 2.7: (a) Photo of BT-7 Triple-axis spectrometer at NIST center for neutron research. (b) Schematic for Triple-axis spectrometer with beam path through monochromator, sample, and analyzer. θ_i are scattering angle; C_j are collimators. Fig. from Ref. [23]

The instruments we most frequently used, such as SPINS, BT-7, BT-9 at the NIST center for neutron research and HB-1, HB-1A at HFIR of ORNL, are Triple-axis spectrometers. The Triple-axis spectrometer is the most versatile and convenient instrument to use in elastic and inelastic neutron scattering experiments, because it allows one to measure energy and momentum space in nearly any coordinates. The three axes in Triple-axis spectrometer correspond to the axes for rotation of the monochromator, the sample, and the analyzer [see Fig. 2.7]. The direction and magnitude of the incident neutron wave vector k_i is selected by Bragg scattering on

the monochromator, which is controlled by θ_1 and θ_2 [see Fig. 2.7 (b)]. The analyzer, which has a similar function as the monochromator, determines the wave vector k_f by Bragg scattering on a analyzer crystal, which is controlled by θ_5 and θ_6 [see Fig. 2.7 (b)]. The orientation of the vector k_i and k_f in the sample's reciprocal space is controlled by orienting the scattering angle at the sample, which is controlled by θ_3 and θ_4 [see Fig. 2.7 (b)]. Therefore by adjusting θ_1-θ_6, we can measure the scattering at any wave vector $\mathbf{Q} = \mathbf{k}_f - \mathbf{k}_i$ and energy transfers $\hbar\omega = E_i - E_f$ in the sample's reciprocal space.

Neutron beams from neutron sources need to be constrained on angular divergence. Neutron collimators are used to control the beam divergence in the horizontal (scattering) plane. The divergence angles on collimators determine the resolution of the measurement. On the other hand, the energy neutron in Triple-axis spectrometer is determined by Bragg scattering on monochromator and analyzer. Higher-order neutrons with wavelengths λ/n, where n is an integer, are also allowed. Filters are used to eliminate neutrons of shorter wavelengths for transmission. Generally, we use Be filter and Pyrolytic graphite (PG) filter, respectively, for energy constrained below 5.2 and 15 meV.

Time-of-flight

Neutron time-of-flight spectrometer is another form of neutron scattering instrument. The neutron time-of-flight spectrometer typically has an area detector, which can measure all allowable wave vectors simultaneously [see Fig. 2.8]. Combined phase choppers are typically used to define the energy and initial time of each neutron pulse. The initial time and velocity of each pulse of neutrons from the neutron source are confirmed, and their final positions and the time after the pulse that the neutrons

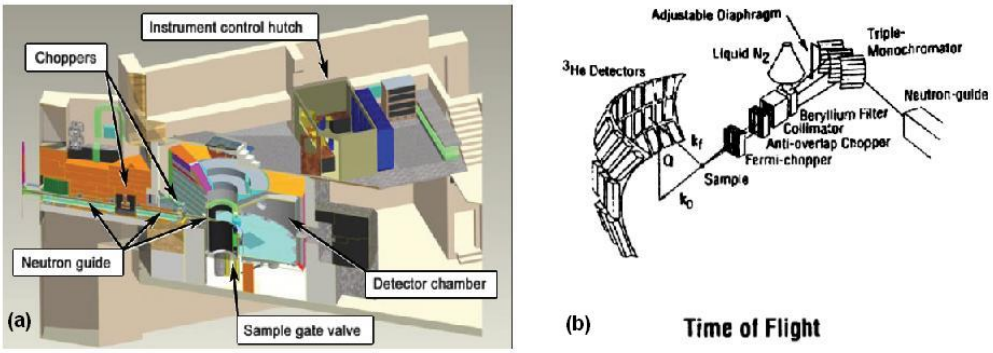

Figure 2.8: (a) Schematic of ARCS Time-of-flight spectrometer at SNS of ORNL. (b) Schematic of components in the Time-of-flight spectrometer. Fig. from Ref. [23]

are detected are measured. Then the travel time and final position on area detectors may be transformed into momenta and energies for the neutrons. By the principle of conservation of momentum and energy, the momentum and energy transferred to the sample can be calculated. It should be noted that the wave vectors $\mathbf{Q}$ is coupled with the energy transfer $\hbar\omega$ due to the conservation of momentum and energy. For example, when measured in [HK0] plane, the actual L is not equal to 0, but a function of h, k and $\hbar\omega$.

Besides Triple-axis and Time-of-flight spectrometers, there are also several neutron scattering instruments such as backscattering and neutron-spin-echo spectrometers, which would not be discussed here.

Chapter 3

$La_{2-x}Ba_xCuO_4$

In this Chapter, I will introduce the "1/8" anomaly and the "stripe" model. I will also discuss our recent experimental results in the $La_{2-x}Ba_xCuO_4$ system. The results include Ba doping, Zn impurities and magnetic field effect on superconductivity and "stripe" order and fluctuations in this system.

3.1 "1/8" anomaly and "stripe"

$La_{2-x}Ba_xCuO_4$ (LBCO) is famous as the prototypical high temperature superconductor. [5] On the other hand, LBCO is also well known for its unusual doping dependence of the bulk superconductivity. [25] The phase diagram of $La_{2-x}Ba_xCuO_4$ as a function of the temperature T and doping concentration x from polycrystalline samples [25] is illustrated in Fig. 3.1. After the antiferromagnetic order is suppressed and superconductivity appears, the T_c vs. doping x curve should have a dome shape from around 0.05 to 0.25. However the T_c shows a deep depression centered around $x = 1/8$, [25] where T_c should be nearly as high as optimal-doping. This inter-

esting phenomenon of mysterious reduction of T_c in LBCO system is known as so-called "1/8" anomaly problem. Later on, the (weaker) 1/8 anomaly is also found in $La_{2-x}Sr_xCuO_4$ (LSCO) system [26, 73–75] [see Fig. 3.1] and other cuprate systems. [28, 76, 77]

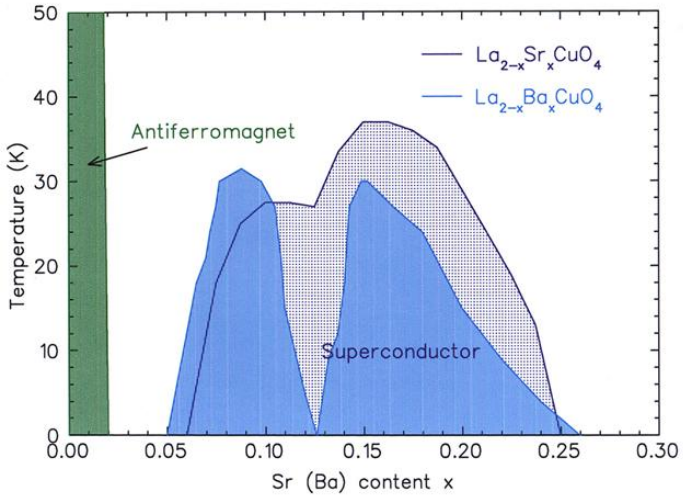

Figure 3.1: Phase diagram of $La_{2-x}Ba_xCuO_4$ and $La_{2-x}Sr_xCuO_4$ as a function of x and T, constructed from polycrystal and single crystal data from Refs. [25–27]. The shaded green area indicates the region in which long-range commensurate antiferromagnetic order. The shaded blue (dark blue point) area indicates the region in which bulk superconducting long-range order occurs for LBCO (LSCO). Fig. from J. M. Tranquada's talk.

Since the superconductivity is strongly associated with magnetism and structure, a series of neutron and X-ray diffraction experiments were performed on these systems. The parent compound of $La_{2-x}Ba_xCuO_4$ system is La_2CuO_4, which is an antiferromagnet with $T_N \sim 300$ K [78, 79]. Commensurate antiferromagnetic Bragg peaks at $\mathbf{Q}$=(0.5,0.5) (in term of reciprocal lattice unit 2π/a, where a is the Cu-Cu separation) caused by antiferromagnetic ordering is found in La_2CuO_4 in (HK0) plane [shown as stars in Fig. 3.2 (a)]. In doping 1/8 samples, the commensurate

antiferromagnetic Bragg peaks disappear and are replaced by four broadened incommensurate peaks at (0.5±δ,0.5) and (0.5,0.5±δ) [shown as blue squares and red circles in Fig. 3.2 (a)] with displacement by small amount $\delta \approx 1/8$. [28, 80] Besides the split of magnetic Bragg peaks, new peaks [shown as blue triangles and red ovals in Fig. 3.2 (a)] are observed displaced by $\delta \approx 1/4$ from the (even) lattice Bragg peaks at $(\pm 2\delta, 2)$ and $(0, 2 \pm 2\delta)$ by both neutron and X-ray. [28, 81–83] Because of the difficulty in growth of high quality LBCO single crystals, the static incommensurate peaks were first found in $La_{1.6-x}Nd_{0.4}Sr_xCuO_4$ [28, 81–83] and later on confirmed in $La_{2-x}Ba_xCuO_4$, [29, 80, 84, 85] $La_{1.875}Ba_{0.125-x}Sr_xCuO_4$, [86, 87] $La_{1.8-x}Eu_{0.2}Sr_xCuO_4$ [88, 89] and other cuprate systems, such as $YBa_2Cu_3O_{7-\delta}$ (YBCO) [90–96] and $Bi_3Sr_2CaCu_2O_{8+\delta}$ (BSCCO). [97, 98]

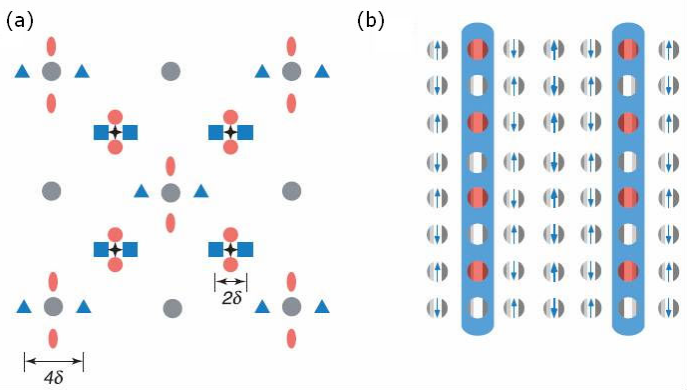

Figure 3.2: Schematic of stripe in reciprocal and real space from Refs. [18, 28, 29]. (a) Schematic of diffraction pattern of stripe ordering. Large gray dots: fundamental lattice Bragg peaks at wave vectors $\mathbf{Q} = 2\pi/a$. Stars: commensurate antiferromagnetic Bragg peaks caused by antiferromagnetic ordering. Blue squares and red circles: incommensurate spin stripe order peaks, displaced from the commensurate peak by a small amount δ related to the doping x. Blue triangles and red ovals: incommensurate charge stripe order peaks, displaced by 2δ from the fundamental lattice peaks. (b) Schematic of stripe ordering, which could give rise to the diffraction pattern shown in (a). Fig. from Ref. [18]

Among the debated interpretations for the incommensurate peaks, it is now believed that in many cases a coupled spin and charge correlations exhibit a 1D "stripe" modulation. [18, 28] The schematic illustration of stripe model is shown in Fig. 3.2 (b), the charge carriers in the CuO_2 planes segregate into hole rich charge stripes [blue shade in Fig. 3.2 (b)], which form antiphase domain well between intermediate spin stripes with locally antiferromagnetic correlations. [28] In the charge stripes, there is one vacancy for every two sites along the stripe and the distance between charge stripes is $a/2x = 4a$, which gives the charge periodicity. On the other hand, the antiphase of spin stripes have double the period of the charge stripes, or $a/x = 8a$. The period of spin stripes leads to Bragg peaks displaced from $\mathbf{Q}$ by $\delta = x$ and period of charge stripes cause Bragg peaks displaced from lattice Bragg peaks by 2δ. [28] The stripes in neighboring layers are believed to be perpendicular to each other and give the four symmetric incommensurate peaks.

The interplay of stripe and superconductivity has not been fully understood. [28, 77, 86, 99] Generally, the static stripe order seems harmful to superconductivity, which is suggested by the "1/8" anomaly. [28, 77, 100] There is also evidence suggesting that static stripe may be compatible with pairing and superconductivity; however, three-dimensional (3D) superconductivity does seem to be frustrated by the stripe order. [30, 101] Two-dimensional (2D) superconducting correlations coexist with stripe order at a temperature even high than T_c. On the other hand, fluctuating stripes seem to benefit superconductivity, where linear relationship between T_c and the incommensurability δ was found in cuprates. [90, 102, 103] Some mechanism relating the stripes to the superconductivity in term of spin-gap proximity effect have been proposed. [104] Moreover the relationship of stripes to superconductivity might not be just either friend or rival.

3.2 Doping dependence on Stripe order

To understand the relationship between stripes and superconductivity, we present our work using neutron scattering as well as static magnetization measurements for a series of $La_{2-x}Ba_xCuO_4$ samples with Ba concentrations (9.5% to 15.5%) around "1/8". [27] The correlations between stripe order, superconductivity, and crystal structure in $La_{2-x}Ba_xCuO_4$ single crystals have been studied. Temperature versus Ba-concentration phase diagram were obtained and shown in Fig. 3.3.

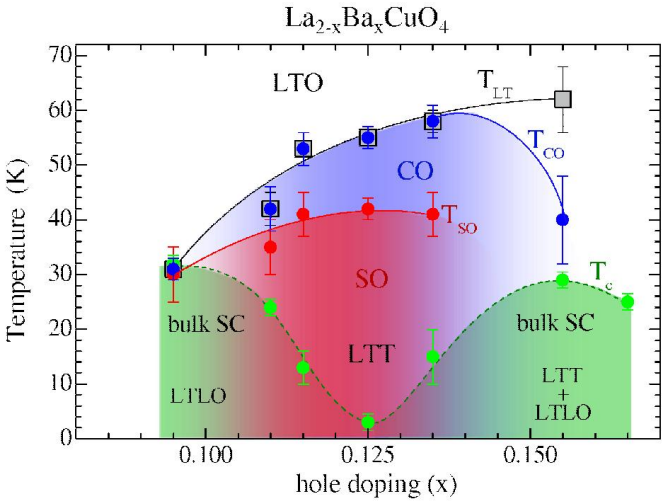

Figure 3.3: (a) Phase diagram of $La_{2-x}Ba_xCuO_4$ as a function of x around 1/8 and T from single crystals. Onset temperatures: T_c of bulk superconductivity (SC), T_{CO} of charge stripe order (CO), T_{SO} of spin stripe order (SO), and T_{LT} of the low temperature structural phases LTT and LTLO . Solid and dashed lines are guides to the eye. The data points in this figure are determined from magnetic susceptibility measurements, neutron diffraction and X-ray diffraction. Fig. from Ref. [27]

The single-crystal samples used here were grown by the traveling-solvent floating-zone method as described in Chapter 2. The neutron scattering experiments were performed at SPINS at NIST center for neutron research, with beam collimations 55'-80'-S-80'-open (S=sample) and fixed final energy of 5 meV. A cooled Be filter

was put after the sample to reduce contamination from higher-order reflections of the analyzer. Part of neutron scattering experiments on 9.5% were measured on HB-1 at High Flux Isotope Reactor, Oak Ridge National Laboratory, with beam collimations 48'-60'-S-60'-240' and fixed final energy of 14.7 meV. Pyrolytic graphite (PG) filters were put before and after the sample. The samples were mounted with ab-plane horizontal, where $(HK0)$ zone is in the scattering plane. The data are described in reciprocal lattice units (r.l.u.) of $(a^*, b^*, c^*) = (2\pi/a, 2\pi/b, 2\pi/c)$ with tetragonal lattice constant: a=b≈3.78 Åand c≈13.2 Å.

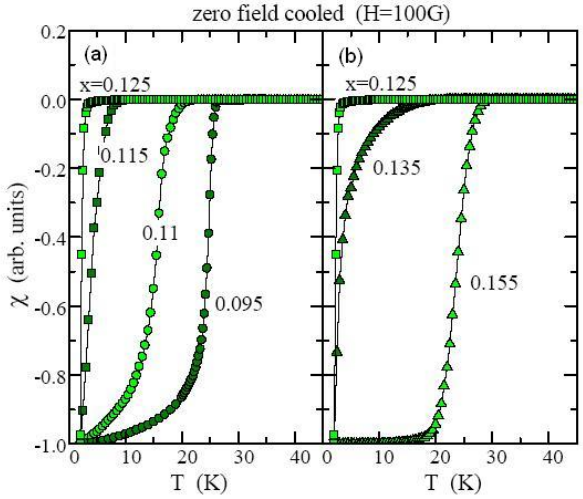

Figure 3.4: Normalized ZFC susceptibility versus temperature for a magnetic field of H = 100 Oe. applied parallel to the c-axis of a series of $La_{2-x}Ba_xCuO_4$. Data in (a) are for $x \leq 1/8$ and in (b) for $x \geq 1/8$. from Ref. [27]

The bulk susceptibility results in Fig. 3.4 were obtained using a superconducting quantum interference device (SQUID) magnetometer. Small (∼0.5 g) well-polished samples were measured with vertical 100 Oe (0.01 T) magnetic field applied perpendicular to the ab plane. In Fig. 3.4 (a), the bulk T_c decreases for $x \geq 0.095$ with increasing x and reaches a minimum at 1/8-doping, while Tc increases again for

x >1/8 by increasing x shown in Fig. 3.4 (b). The bulk SC T_c shown as green shade in phase diagram Fig. 3.3 were each determined from the intercept of the tangent to the steepest part of the curve and χ=0, except x=0.135. Susceptibility of x=0.135 has a very broad transition, which may originate from a very steep phase boundary in that region, or sample inhomogeneity. T_c for x=0.135 is identified by the onset temperature of the transition.

Cooling from room temperature, $La_{2-x}Ba_xCuO_4$ samples will undergo two structural transitions: a second-order transition from high-temperature-tetragonal (HTT) to low-temperature-orthorhombic (LTO), and a first-order transition from LTO to another low temperature phase which can either be low-temperature-tetragonal (LTT) or the low-temperature-less-orthorhombic (LTLO) phase, which is a possible intermediate phase between LTO and LTT. [105] The transition temperature T_{HT} of HTT to LTO has been measured by X-ray diffraction as shown in Fig. 3.7 (a). [27] The T_{HT} decreases linearly with increasing x, and the slope corresponds to $dT_{HT}/dx \sim 23.1K/0.01Ba$. So T_{HT} can be used to estimate the deviation of actual Ba concentration from the nominal composition of the samples.

The second transition temperature T_{LT} of LTO to either LTT or LTLO was measured by neutron scattering. To examine the T_{LT}, the temperature dependence of the (1,0,0) Bragg peak, which is allowed in the LTT and LTLO phases, but not in the LTO phase, was measured as shown in Fig. 3.5 (a). Except x=0.095, the low temperature phase is LTT, the intensities were measured by sitting on the (100) Bragg peak. For x=0.095, where the low temperature phase is LTLO, the intensities were obtained by peak intensity from scans across the peak. When a sample is cooled below T_{LT}, the (100) Bragg peak intensity increases abruptly in a parameter-order-like transition as in Fig 3.5(a), which is indicative of the transitions first order nature. On the other

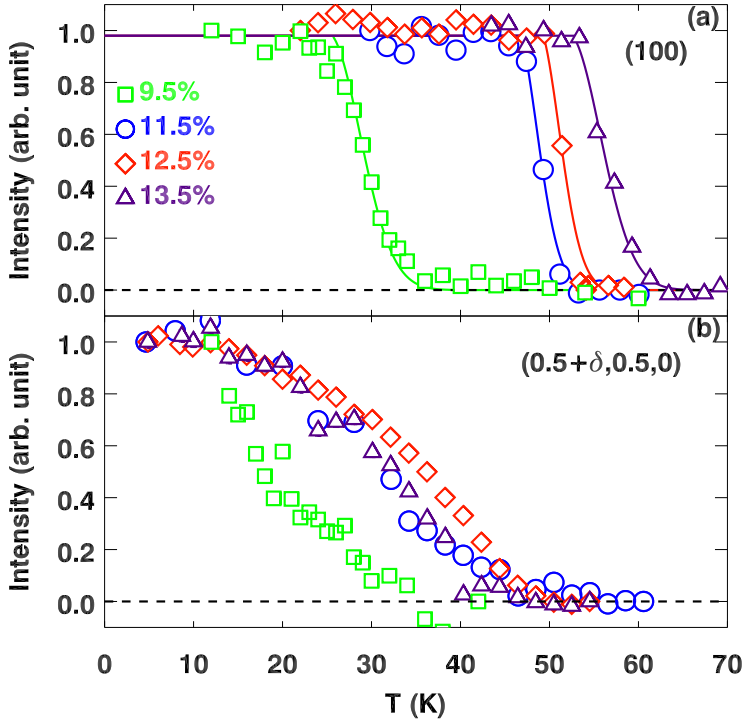

Figure 3.5: Temperature dependence of the peak intensity for (a) (100) Bragg peak superstructure peak normalized at low temperature, and, (b) super lattice peak (0.5+δ,0.5,0) corresponding to the spin-stripe order for $La_{2-x}Ba_xCuO_4$ with x=0.095 (green square), 0.115 (blue circle), 0.125 (red diamond) and 0.135 (purple triangle). The stripe-order peak intensity has been superstructure peak normalized at low temperature. Lines through data are guides to the eyes.

hand, this also indicates a high homogeneity of our crystals stoichiometry and quality.

The spin stripe order was studied by neutron scattering. The spin stripe order peaks were found in all samples with $x \leq 0.135$. The magnetic ordering wave vectors of the spin stripe order peaks are (0.5$\pm\delta$,0.5,0), which are displaced by δ from the position of the commensurate magnetic Bragg peak in the AF parent compound La_2CuO_4. The h-scan through the (0.5+δ, 0.5, 0) peak for the different dopings at 5 K are shown in Fig. 3.6. The data here were taken at SPINS with identical configuration and is normalized by the crystal volume in the beam, thus allowing

a direct comparison of the intensities. The maximum of the spin stripe order peak is for x=1/8, which has the lowest T_c and the intensity decreases for x apart from 1/8, where the T_c increases. The peak of x=0.095 is definitely much weaker, which intensity is only 1/10 of the x=1/8, while this crystal is a good bulk superconductor with highest T_c. This clearly suggests that the static spin stripe order is "bad" for bulk superconductivity, the stronger the static spin stripe order, the more reduction in the T_c. This relation is also consistent with previous results in LSCO related samples. [28, 77, 86, 106, 107]

The temperature dependence of the normalized peak intensity of the spin order peak are plotted in Fig 3.5(b). Comparing to results in Fig 3.5 (a), the onset temperatures of spin order are always below T_{LT}, suggesting that the static spin stripe developed in the LTT symmetry. [28, 80, 108, 109] The temperature dependence of the spin order and (1,0,0) peak intensities evolve differently in Fig 3.5, where the spin order peaks show very broad transitions. The T_{SO} are determined by the temperature when the spin order peaks start to broaden instead of onset of spin order peak, because truly static spin order sets in below the onset temperature seen by neutron diffraction. The difference is due to the coarser energy resolution of neutron diffraction, which can integrate over low-energy spin fluctuations at $T > T_{SO}$. [110] The spin order temperature, T_{SO}, has also been checked by muon spin rotation (μSR) spectroscopy [111] and by a single-crystal magnetization study. [27, 112]

As one can see in Fig. 3.6, the center of spin stripe peak shifts to higher h with increasing x. The incommensurability δ derived from the fitting of spin order peaks by neutron scattering are plotted in Fig. 3.7 (b). The incommensurability δ derived from charge order peaks from Ref. [27] have good agreement with the values determined with spin order peaks and are also plotted in Fig. 3.7 (b). The values of δ here well

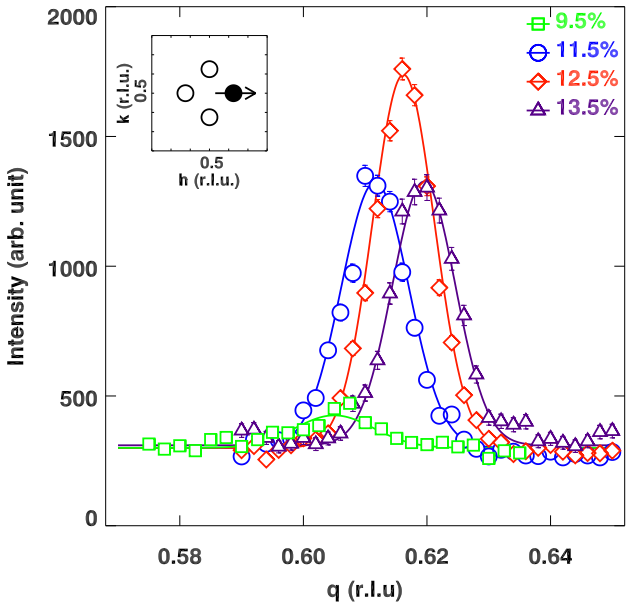

Figure 3.6: In-plane scans through one of the spin stripe order peak (0.5+δ,0.5,0) (see the inset) for different Ba concentrations, 0.095 (green square), 0.115 (blue circle), 0.125 (red diamond) and 0.135 (purple triangle), with scan direction indicated by the arrow in the inset. Errors represent square root of the counts. Lines are fits to the data with Lorentzian function convoluted with the resolution function. The peak intensity has been normalized by crystal volume to the results of the 0.125 sample.

follow the estimated trend based on experimental results in LSCO systems, where $\delta = x$ for $x \leq 1/8$ and saturates for $x > 0.125$. [28, 86, 102] Since δ is proportional to the inverse of the spin and charge modulation period, and the $\delta \sim x$ behavior suggests that the modulation period decreases with increasing x for $x \leq 1/8$. For $x > 0.125$, the modulation seems to be saturate with period of 4 for charge stripe. More hole doping seems to just increase the hole concentration in the charge stripe. [102]

The charge stripe order was studied with high energy single-crystal X-ray diffraction (XRD), where the atomic displacements affected by charge density modulation were measured. Charge stripe order peaks were found around (2$\pm$2δ,0,5.5) in all samples. [27] The onset temperature of charge order T_{CO} always coincides with the

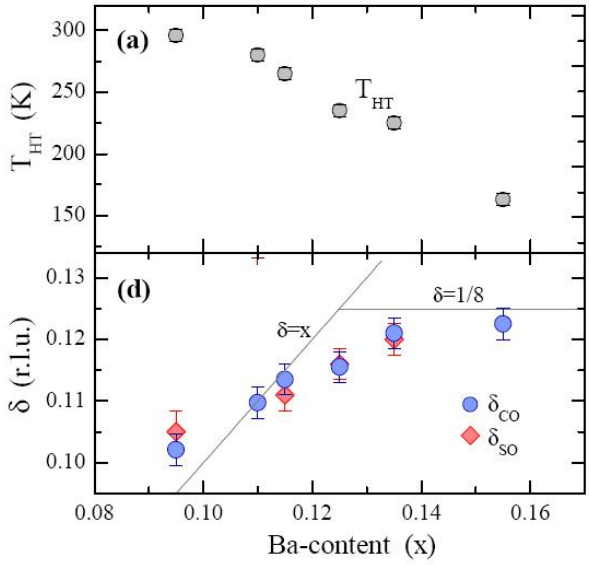

Figure 3.7: Crucial parameters of stripe phase and crystal structure in La2.xBaxCuO4 versus nominal Ba content. (a) HTT to LTO transition temperature T_{HT} (b) Incommensurability δ extracted with XRD from the charge order peak and with neutron scattering from the spin order peak. The solid lines δ=x and δ=1/8 describe the low and high x reference of the stripe model. Fig. from Ref. [27]

LTO to LTT/LTLO transition, so T_{CO}=T_{LT}, for $x \leq$0.135 as shown in phase diagram Fig. 3.3. The peak intensity is maximum at x=1/8 and falls off rapidly for x apart from 1/8, similar to the case of the spin order peaks.

The summary of the doping dependence of transition temperature of bulk superconductivity T_c, low temperature structure phase T_{LT}, charge stripe order T_{CO} and spin stripe order T_{SO} give the phase diagram with Ba concentration near the 1/8 shown in Fig. 3.3 and listed in Table 3.1. Both intensities and order temperature of magnetic and the charge stripe order are maximum at x=1/8, where bulk superconductivity is most strongly suppressed. The stripe order seems to compete and coexist with the bulk superconductivity.

Table 3.1: Summary of the doping dependence in $La_{2-x}Ba_xCuO_4$. Doping x, transition temperature of bulk superconductivity T_c, high and low temperature structure phase T_{HT} and T_{LT}, charge stripe order T_{CO} and spin stripe order T_{SO}, incommensurability δ.

x (%)	T_c (K)	T_{HT} (K)	T_{LT} (K)	T_{co} (K)	T_{so} (K)	δ (r.l.u.)
9.5	32	310	27	27	27	0.105
11.5	13	271	52	51	38	0.112
12.5	3	235	55	54	42	0.118
13.5	7	223	58	55	39	0.120
15.5	30	157	45	45		0.123

3.3 Dynamic stripes in LBCO x=9.5%

The static spin stripe order correlates with decrease of bulk superconductivity, while the nature of magnetic excitation in high temperature superconductivity seems correlated with dynamic stripe. [29, 113, 114] Almost all observed features of the magnetic scattering from cuprate superconductors can be described by a universal magnetic excitation spectrum multiplied by a spin gap function. [113] The universal magnetic excitation spectrum seems correlated with dynamic stripe. [29]

Most previous inelastic neutron scattering works in LBCO system focus on x=1/8. In this section, we will present an investigation of low-energy magnetic excitations (up to 12 meV) in LBCO with x=0.095. Comparing to 1/8, LBCO with x=0.095 has the highest T_c in the LBCO system and comparatively weak static stripe order at low temperature. [27] The crystal with x=0.095 has a unique feature, where the structure phase transition occurs just below the superconducting (SC) transition. Fig. 3.8 (b) shows the field-cooled magnetic susceptibility measured by SQUID. After the initial onset of bulk SC in the LTO phase at T_c = 32 K, SC collapses below 30 K when both the LTO to LTLO and the charge stripe order (CO) transition occur, as shown

in Fig. 3.8 (a). Once the transformation is complete, bulk SC reappears.

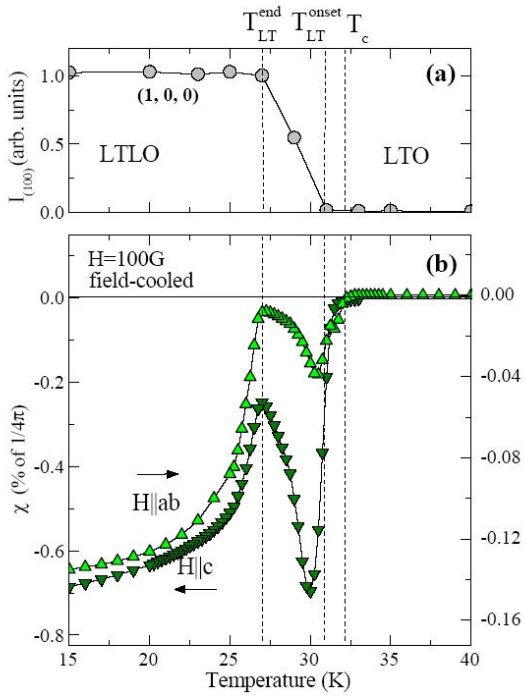

Figure 3.8: Superconductivity and structure transition in $La_{1.905}Ba_{0.095}CuO_4$. Temperature dependence of (a) Integrated intensity of the (1,0,0) superstructure reflection, (b) Field cooled signal for H = 100 G applied parallel to the c-axis and the ab-plane. T_c indicates the onset of bulk SC in the LTO phase. T_{LT}^{onset} and T_{LT}^{end} denote the onset and the completion of the LTO to LTLO transition, respectively. Fig. from Ref. [27]

LBCO with x=0.095 has a mix structure of LTT and LTO instead of pure LTT as LBCO with x=1/8 just below phase transition temperature. In Fig. 3.9, we plot the scans showing the temperature evolution of the peaks from the LTO to LTT phase. The scan direction and peak patterns are shown in the insets. At 54 K, there are two strong LTO peaks (open grey circles), so scan gives rise to the profile as shown in Fig. 3.9(a). With cooling, the orthorhombicity is decreasing, and the tetragonal peak [indicated by the closed circle in the inset] starts to show up at 33 K. Along with two

weaker LTO peaks, the scan has a three-peak shape around transition temperature. With further cooling to 27 K, the orthorhombic peaks are almost gone, and become shoulders of the LTT peak as shown in Fig. 3.9 (c). Below 27 K, the system is in the LTT phase, and scan results in a single-peak profile as shown in Fig. 3.9 (d). A high-resolution X-ray scattering study has shown a LTLO splitting of the Bragg peak at low temperature, [27] which cannot resolve by neutron scattering due to resolution limit.

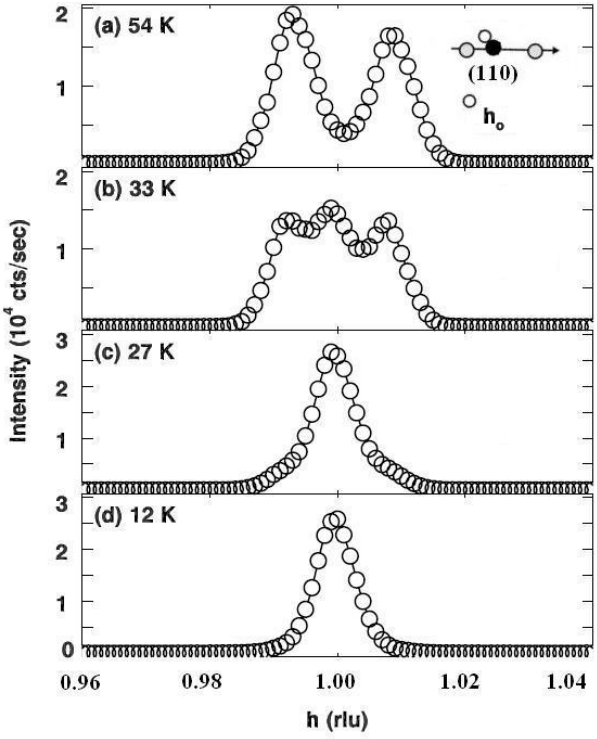

Figure 3.9: Evolution from LTO peaks at 54 K to the LTT peak at 12 K. Insets show the schematics of the peak patterns, and the scan direction. In the insets, closed circles: LTT peaks; open circles: LTO peaks.

The neutron scattering experiments were performed at triple-axis HB-1 (at HFIR,

Oak Ridge National Laboratory), BT-7 and Multi Axis Crystal Spectrometer (MACS) [115] (at NCNR, National Institute of Standards Technology). On HB-1, we used beam collimations 48'-60'-S-60'-240' and fixed final energy of 13.5 meV. On BT-7, we used beam collimations open-80'-S-50'-50' and fixed final energy of 14.7 meV. Pyrolytic graphite (PG) filters were put after the sample to reduce contamination from higher-order neutrons. On MACS, we used beam collimations of 100'-open-S-90'-open with E_f=5.0 meV and Be filter was put after the sample. The samples were mounted with *ab*-plane horizontal and the scattering plane ($HK0$) defined by vectors [100] and [010]. The scattering vectors $Q = (h, k, l)$ are specified in reciprocal lattice units (r.l.u.) of $(2\pi/a, 2\pi/b, 2\pi/c)$, where $a = b \approx$3.78 Åand $c \approx$13.2 Åare the lattice parameters of the HTT phase.

MACS is a new cold neutron spectrometer under development at NIST. Double focusing monochromator provides MACS very high neutron beam flux at sample position. The detection system for MACS consists of twenty independent monochromatic channels instead of one in conventional triple-axis. The multi-detector system allows MACS to measure a series of Q simultaneously. Here L is fixed at 0 for the scattering plane, whereas it is typically a function of H, K and E in time-of-flight spectra. In addition, Q and E resolution of MACS is also better due to using cold neutron source.

We performed constant-energy mesh scans to map out the cross-section of magnetic excitations by MACS for several energies and temperatures. Fig. 3.10 (a)-(c) show the 1 meV slices of the magnetic scattering near the antiferromagnetic wave vector, $\mathbf{Q}_{AF}$=(0.5, 0.5) below and above T_c. Four incommensurate peaks characteristic of stripe correlations are clearly seen in slices (a). Since we knew that static spin stripe order is present in the sample below structure transition temperature T_{LT} (T_{LT}^{end}, 27 K), [27, 30] the substantial peak intensities at 1.5 K suggest that no gap in

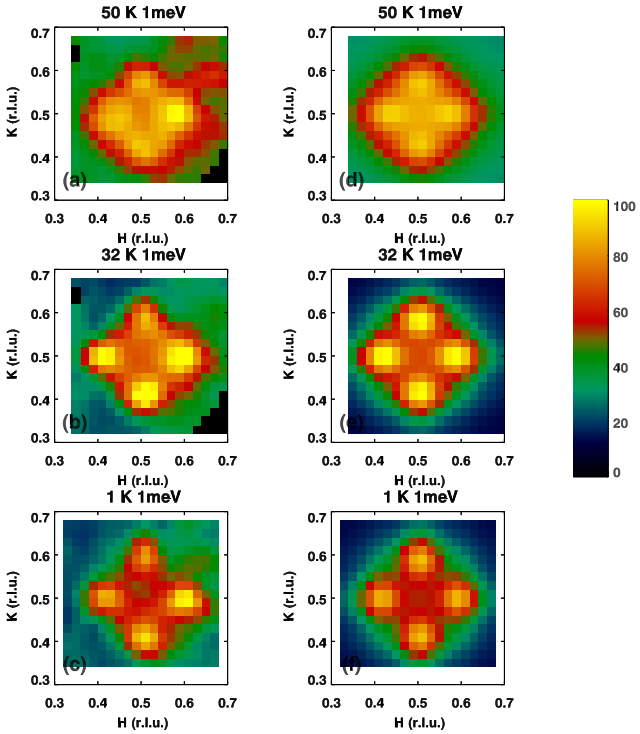

Figure 3.10: Image of constant-energy cross-section of magnetic scattering of $La_{1.905}Ba_{0.095}CuO_4$ measured on MACS . Intensity measured with $\hbar\omega$=1 meV at (a) 60 K, (b) 32 K, (c) 1.5 K. (d)-(f) are fits to the cross-section described by four lattice Lorentzian (LL) peaks at (0.5, 0.5$\pm\delta$) and (0.5$\pm\delta$, 0.5), where δ is the incommensurability.

the spin excitation spectrum is observed in the superconducting state for this compound. The distances between the pair of incommensurate peaks shorten and the peak width broadens with increasing temperature. The peaks appear to over-lap with increasing temperature as shown in panel (c).

The four incommensurate peaks have four-fold symmetric position about $\mathbf{Q}_{AF}$. Therefore we fit the data with a model described by four resolution corrected lattice Lorentzian (LL) peaks at (0.5$\pm\delta$,0.5) and (0.5,0.5$\pm\delta$), where δ is the incommensurability. The profile of the peak is product of Voigt functions, which is Lorentzian

function convoluted with the Gaussian resolution.

$$V(x) = \int_{-\infty}^{\infty} L(x - x')G(x')dx' \tag{3.1}$$

Where $L(x)$ is is Lorentzian function and $G(x')$ Gaussian function for resolution and Voigt function can be described as:

$$V(x) = \frac{1}{\sqrt{2\pi}\sigma} \cdot \frac{a}{\pi} \int_{-\infty}^{\infty} \frac{e^{-y^2}dy}{a^2 + (u - y)^2} \tag{3.2}$$

where $a = \kappa/\sqrt{2\pi}\sigma$ and $u = (x - x_0)/\sqrt{2\pi}\sigma$. Here x_0 is the peak center; κ is the peak width and σ is the resolution. The fitting results are plotted in Fig. 3.10 (d)-(f).

Due to limit of energy transfer at small-Q on MACS, energy transfer $\hbar\omega \geq$6 meV were measured on BT-7. Fig. 3.11 (a)-(b) show the linear constant-energy scans for $\hbar\omega$ =6 and 10 meV at 5 K. The incommensurate peaks were fitted by two Lorentzian functions. The peak center are plotted by open circles in panel (c) as well as the spin spectrum below 6 meV, which are real data measured on MACS. The spectrum disperses inward from the incommensurate elastic peaks below 6 meV and weakly changes above 6 meV. The dispersion is similar with results of LSCO, which have similar T_c and doping. [116–118] The dispersion also qualitatively agrees with the universal magnetic excitation spectrum found in hole-doped cuprates. [24, 113, 119]

Fig. 3.12 shows the energy dependence of dynamical magnetic susceptibility, $\tilde{\chi}$", incommensurability δ and peak width κ for a number of temperatures. The imaginary part of the spin susceptibility $\tilde{\chi}''(\omega)$, which integrate Q of $\chi''(\mathbf{Q},\omega) = S(\mathbf{Q},\omega)(1 - e^{-\hbar\omega/k_BT})$. The energy dependence of $\tilde{\chi}$" is shown in panel (a). $\tilde{\chi}$" is almost independent of ω for $\hbar\omega \geq$6 meV for all temperatures. $\tilde{\chi}$" above 6 meV has no difference

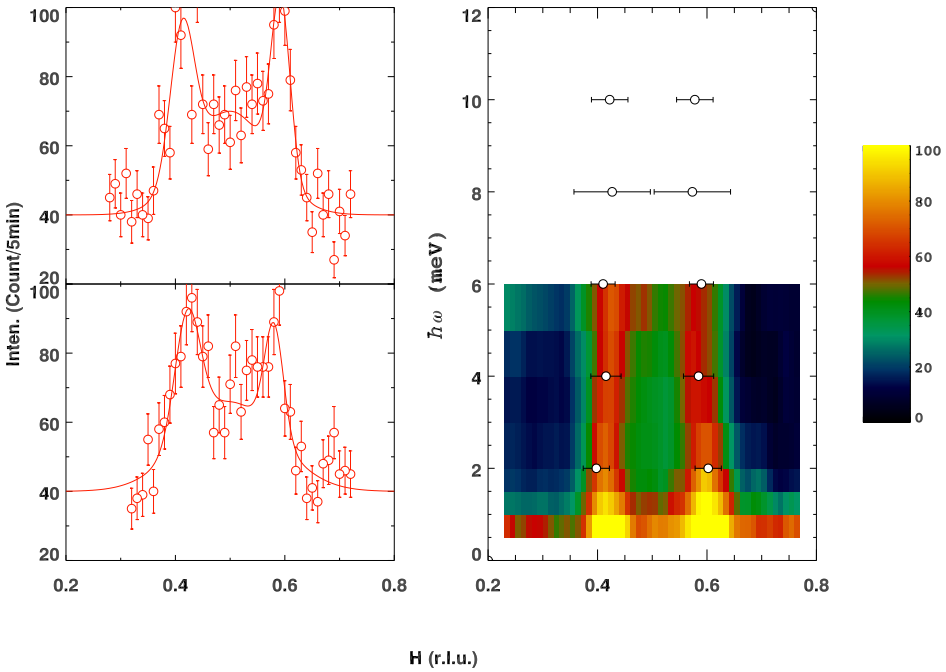

Figure 3.11: Magnetic excitations of $La_{1.905}Ba_{0.095}CuO_4$ at 5 K measured on BT-7. Linear scans through the spin stripe excitation peaks at (a) 10 meV, (b) 6 meV. The line are guide for the eye from fitting of 2 Lorentzian peaks. (c) Dispersion of the excitations, the image below 6 meV are data from MACS. The circle are peak centers from the fitting of linear scans as (a) and (b) from BT-7 data.

for temperature below and just above T_c. The behavior of $\tilde{\chi}$" with $\hbar\omega \leq 6$ meV is different. In the spin stripe order phase, there is a sharp increase of $\tilde{\chi}$" below 3 meV, which may correspond to presence of quasi static spin stripe order. In LSCO 16%, which has similar T_c, [116, 118] spin gap below 7 meV and resonance of 12 meV was observed in superconducting state. The $\tilde{\chi}$" of LSCO below T_c is almost equal to zero below 7 meV and sharply increase above 7 meV and has significant change above T_c. [118] The behavior of $\tilde{\chi}$" in superconducting state here is totaly different with results in LSCO 16%, suggests that there is no spin gap or resonance associated with superconductivity in this compound. At temperature above T_{LT}, $\tilde{\chi}$" is a linear

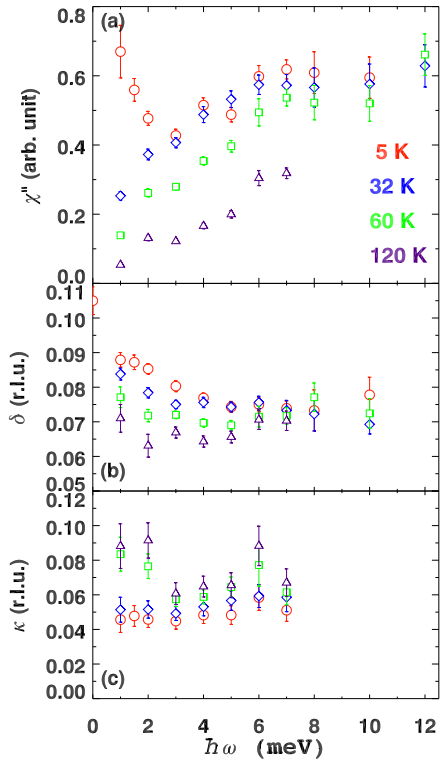

Figure 3.12: (a) Imaginary part of the dynamical magnetic susceptibility, $\tilde{\chi}$"(ω) (b) Incommensurability δ (c) resolution-corrected peak width (half width at half maximum) κ of IC peaks as a function of $\hbar\omega$ in $La_{1.905}Ba_{0.095}CuO_4$ at 1.5 K (red circle), 32 K (blue diamond), 60 K (green square) and 120 K (purple triangle). Points with $\hbar\omega \leq 7$ meV are from fitting of MACS data, points with $\hbar\omega \geq 8$ meV are from fitting of linear scans from BT-7.

decrease towards zero at lower energy. At higher temperatures, the overall magnitude of $\tilde{\chi}$" is gradually reduced with increasing temperature. The feature of $\tilde{\chi}$" above T_{LT} is what one expects to see for spin fluctuations in a disordered spin system and quite similar to what is observed in LBCO 1/8 and LSCO. [80, 116]

The energy dependence of incommensurability δ is shown in panel (b). For lower temperatures 1.5 K and 32 K, δ gradually decreases with increasing energy below 6 meV and weakly change above 6 meV. While δ is slightly smaller than the value found in static spin stripe peaks, [27] possibly due to some meandering or disorder

in stripes. The dispersion of δ almost disappears above 60 K, where δ are almost independent of energy at 60 K and 120 K. The energy dependence of resolution-corrected peak width κ are shown in panel (c). For lower temperatures 1.5 K and 32 K, κ is roughly independent of energy. On temperatures above 60 K, κ has a large value at low energy and decease with energy increasing, while changes relatively little for $\hbar\omega \geq 4$ meV.

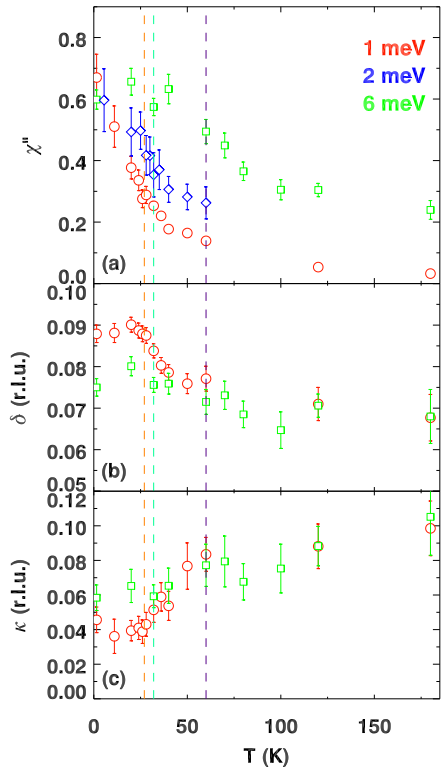

Figure 3.13: (a) Imaginary part of the dynamical magnetic susceptibility, $\tilde{\chi}"(\omega)$ (b) Incommensurability δ (c) resolution-corrected peak width (half width at half maximum) κ of IC peaks as a function of temperature in $La_{1.905}Ba_{0.095}CuO_4$ at 1 meV(red circle), 2 meV (blue diamond) and 6 meV (green square). Points of 1 and 6 meV are from fitting of MACS data, while points of 2 meV are from fitting of HB-1 data. Vertical lines indicate T_{SO} (orange), T_c (teal) and T_{2D} of 2D vortex liquid (purple).

Fig. 3.13 shows the temperature dependence of fitting parameters for 1 meV, 2 meV and 6 meV. The temperature dependence of $\tilde{\chi}"$ is shown in panel (a). The

temperature dependence of $\tilde{\chi}$" of 1 meV and 2 meV exhibit a sharp kink around T_{LT}, while $\tilde{\chi}$" starts to increase around T_c upon cooling due to the ordering of spin fluctuation. The temperature dependence of $\tilde{\chi}$" of 6 meV shows different behavior, which is not affected by the phase transition at T_c and T_{LT}. The $\tilde{\chi}$" of 6 meV starts to decrease around 60 K, which is consistent with the phase transition of 2D vortex liquid phase. [30]

The temperature dependence of incommensurability δ is shown in panel (b). There is a jump in δ for 1 meV at T_{LT} suggesting a lock-in effect, with the stripe spacing adjusting to be commensurate with the modulated lattice potential that pins the stripes in the LTT phase. Above T_{LT}, δ decreases with increasing temperature. The temperature dependence of resolution-corrected peak width κ is shown in panel (c). The κ of 1 meV is almost constant below T_{LT}, while it increase on warming up above T_{LT}. It seems the low energy spin fluctuations more easily lose coherence in the disordered state.

The low energy spin fluctuations of LBCO x=0.095 in the normal state are quantitatively similar to the results in LBCO x=1/8. [80] The feature of $\tilde{\chi}$", δ and κ in transition to spin stripe order phase is also similar in LBCO x=1/8. [80] However behavior of low energy spin fluctuations below T_{LT} is different. $\tilde{\chi}$" in LBCO x=1/8 is independent of energy, which is expectation for spin waves, while $\tilde{\chi}$" in LBCO x=0.095 shows an upturn below 3 meV, which may be due to the freezing of the low-frequency spin fluctuations. [120] On the other hand, the low energy spin fluctuations in LBCO x=1/8 are resolution limited and κ increases roughly linearly with energy, while κ in LBCO x=0.095 has a finite value and is almost independent with energy. This result suggests that the spin stripe order in LBCO x=0.095 may be short-range order since we known that the spin order is very weak and develops in

a somewhat glassy fashion in x=0.095 instead of a parameter-order-like behavior in LBCO x=1/8. [27, 80]

It is also interesting to compare our results with other underdoped cuprates. For underdoped LSCO, [116, 120, 121] the low energy spin fluctuations in the superconducting state are similar to these in LBCO x=0.095, although no static stripe order was found in the underdoped LSCO at low temperature without pinning by impurities or external magnetic field. [87, 122, 123] There is also no significant spin gap or resonance observed in superconducting state underdoped and overdoped LSCO. [116] Since underdoped LSCO and LBCO x=0.095 have similar T_c, the upturn of $\tilde{\chi}$" at low E may also due to freezing of the low-frequency spin fluctuations in superconducting state. [120]

Fermi-surface-nesting seems not to work well to understand the incommensurate spin fluctuations for LBCO system. [124] The missing of spin gap and resonance and hour-glass-like spectrum is beyond the explanation in terms of Fermi-surface-nesting of the shape of Fermi surface from photoemission measurements [**?**]. On the other hand, our measurements provide clear evidence of the dynamic stripe phase presence. The dynamic stripe scenario provides an approach for understanding the universal magnetic excitation spectrum in cuprates, such as YBCO, LSCO and LBCO. [24, 29, 113] The electrons in superconductivity and magnetism seem different. The couple of conducting electrons and local magnetic excitation leads to high temperature superconductivity. [124]

In summary, we have studied the energy and temperature dependence of the spin fluctuations for $La_{1.905}Ba_{0.095}CuO_4$ using neutron inelastic scattering. Incommensurate spin excitations observed in this compound below 180 K provide clear evidence for dynamic spin stripes. No clear spin gap or resonance is observed in the supercon-

ducting state even though this compound has the highest T_c in the LBCO system. The magnetic spectrum due to dynamic stripes seems to be universal in high temperature superconductors.

3.4 Magnetic field effect on Stripe order

One possible way to explore the correlation between the superconductivity and stripe order is study the impact of a magnetic field. A perpendicular magnetic field can penetrate the layers as quantized flux screened by superconducting vortices. This usually affects both the bulk superconductivity and the stripe order. [125–129] We have performed neutron scattering as well as static magnetization measurements on a $La_{1.905}Ba_{0.095}CuO_4$ single crystal under a magnetic field perpendicular to the *ab*-plane.

The neutron diffraction experiments were performed with triple-axis spectrometer, SPINS, located at NIST Center for Neutron Research, at National Institute of Standards Technology, using beam collimations of 55'-80'-S-80'-open (S =sample) with E_f=5 meV. To reduce contamination from higher-order neutrons, cooled Be filters put before and after the sample. The samples were mounted with *ab*-plane parallel to the scattering plane and $(HK0)$ plane defined by vectors [100] and [010]. The scattering vectors $Q = (h, k, l)$ are specified in reciprocal lattice units (r.l.u.) of $(2\pi/a, 2\pi/b, 2\pi/c)$, where $a = b \approx 3.78$ Åand $c \approx 13.2$ Å. are the lattice parameters of the HTT phase. A vertical-field superconducting magnet was used, and the applied field was perpendicular to the *ab*-plane.

Wen et.al [30] have measured the temperature dependence of the electrical resistivity in single crystals of LBCO x=0.095 by the standard four-probe technique, in a Physical Properties Measurement System (PPMS) from Quantum Design. The

resistance parallel ($\rho_{\parallel}$) and perpendicular ($\rho_{\perp}$) to the planes have been investigated under the impact of a magnetic field of $H_{\perp}$ applied to the planes. The temperature of zero resistivity for $\rho_{\parallel}$ and $\rho_{\perp}$ are plotted in Fig. 3.14. The field has a drastic effect on $\rho_{\perp}$, the transition temperature is highly suppressed from 32 K to around 5 K. In constrast the impact of field on $\rho_{\parallel}$ is rather weak, with T_c only decreasing to around 27 K. We find that there is a broad regime where $\rho_{\parallel}$ is zero but $\rho_{\perp}$ is not. This suggests there is a uniaxial resistivity caused by the perpendicular magnetic field.

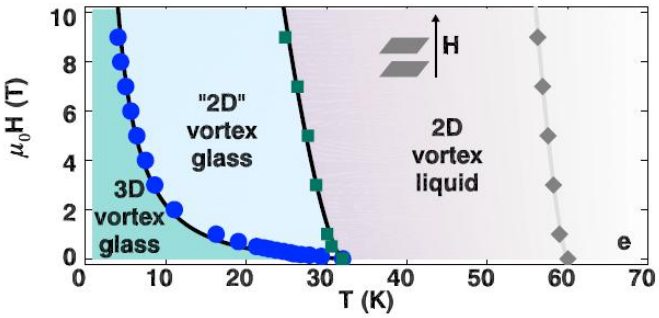

Figure 3.14: Phase diagram for vortex matter in a perpendicular field (H⊥ *ab*-plane). Experimentally-determined Zero-resistivity transition temperature for a range of magnetic fields. For $\rho_{\perp}$ (blue circles) and $\rho_{\parallel}$ (green squares). Fig. from Ref. [30]

Temperature dependence of intensity of spin stripe order peak is measured by neutron scattering and shown in Fig. 3.15 (a). The external magnetic field perpendicular to the *ab*-plane enhances the intensity of spin stripe order peak for whole temperature range. The way the order develops is almost the same as that without field and the onset temperature of spin stripe order seems unaffected under the field. Temperature dependence of intensity of charge stripe order peak and lattice Bragg peak (300) is measured by X-ray diffraction and shown in Fig. 3.15 (b)-(c). Similar enhancement is found for the charge stripe order peak intensities. On the other hand, the low temperature structure transition is not affected by the field and shows the

same phase transition at $T_{LT} \sim 27$ K.

The perpendicular magnetic field can penetrate the layers as quantized flux screened by superconducting vortices, and weakens the Josephson coupling, [130] and eventually leading to a loss of superconducting order. [131] While theory suggests that it is impossible for a homogeneous three-dimensional crystal to exhibit superconducting order in two directions but not in the third. [132–134] The crystal symmetry change in structure weakly pins charge and spin stripe order in zero field [99] and the enhancement of stripe order by a perpendicular magnetic field. The stripe order is presumably associated with the vortex cores [125, 127] and weakens the Josephson coupling between layers. [101, 135–137] Vortex-nucleated stripe order seems enhance the 2D pinning of vortices, which cause phase fluctuations between the layers and do not affect the superconducting correlations within each layers.

To summarize, perpendicular magnetic field induce a phase in which zero resistivity is observed parallel to the layers but application of a finite measurement current perpendicular to the layers results in a finite resistivity in $La_{1.905}Ba_{0.095}CuO_4$. We have demonstrated that the perpendicular magnetic field clearly enhance both spin and charge stripe order. The stripe order seems to be associated with vortex cores and weakens the Josephson coupling between layers, which eventually leading to the uniaxial loss of superconducting order.

3.5 Zn impurity effect on Stripe order

To better understand the interplay between stripe correlations and superconductivity in cuprates, doping Zn into LBCO (x=0.095) is one way to examine the coexistence and competitions between stripe order and superconductivity, since it is

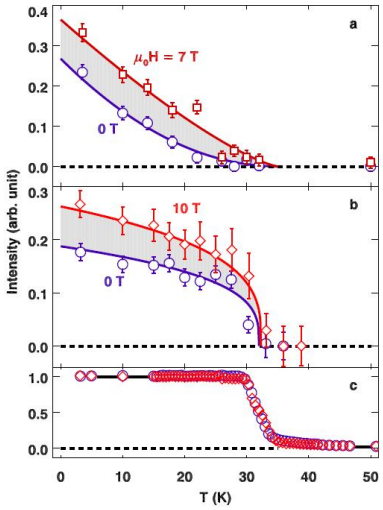

Figure 3.15: Impact of a perpendicular magnetic field on spin and charge order. a, Integrated intensity of the magnetic spin order superlattice peak at wave vector (0.6, 0.5, 0) in H=0 T (violet circles) and 7 T (red squares), obtained by neutron diffraction. b, Integrated intensity of the charge-order superlattice peak (0.2, 0, 8.5) in H=0 T (violet circles) and 10 T (red diamonds), obtained by X-ray diffraction. c, Integrated intensity of the (300) superlattice peak, characterizing the structural transition to the low-temperature phase, in 0 T and 10 T as in b. For a and b, intensities are normalized (approximately) to results for LBCO x=0.125 in zero field; [**?**] for c, intensities are normalized at low temperature. Error bars reflect counting statistics. Lines through the data points are guides to the eye. Gray regions emphasize the change induced by the magnetic field. Fig. from Ref. [30]

known that Zn doping will greatly suppress the superconductivity, such as in LSCO (x=0.15). [87] Small amounts of Zn was found to induce stabilization in particular for the spin stripe order (SO). [87, 138] To further elucidate the possible mechanisms by which stripes can be stabilized, we decided to study the effect of Zn-doping on LBCO, a system where CO and SO forms naturally without impurity doping or magnetic field. We have performed neutron scattering as well as static magnetization measurements on a pure $La_{1.905}Ba_{0.095}CuO_4$ and a Zn-doped $La_{1.905}Ba_{0.095}CuZn_{0.001}O_4$ single crystals samples.

The LBCO95 and LBCZO95 single crystals were grown with the traveling-solvent floating-zone technique. The neutron diffraction experiments with triple-axis spectrometer HB-1A at the High Flux Isotope Reactor, Oak Ridge National Laboratory, using beam collimations of 48'-48'-S-40'-136' with $E_f = 14.7$ meV. To reduce contamination from higher-order neutrons, pyrolytic graphite (PG) filters were put before and after the sample. The samples were mounted with *ab*-plane parallel to the scattering plane and $(HK0)$ plane defined by vectors [100] and [010]. The scattering vectors Q = (h, k, l) are specified in reciprocal lattice units (r.l.u.) of $(2\pi/a, 2\pi/b, 2\pi/c)$, where $a = b \approx 3.78$ Åand $c \approx 13.2$ Å. are the lattice parameters of the HTT phase.

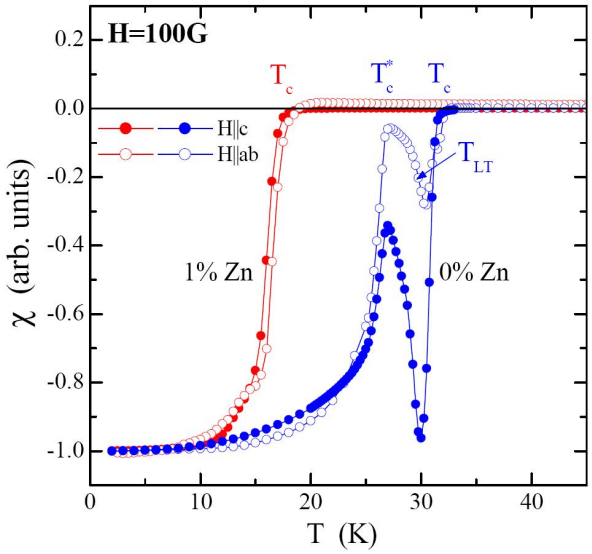

Figure 3.16: Normalized field cooled susceptibility vs T of pure and Zn doped $La_{1.905}Ba_{0.095}CuO_4$ at H = 100 G applied parallel *ab*-plane and c-axis. Fig. from Ref. [31]

The SC properties of two samples have been characterized with a SQUID-magnetometer for H parallel and perpendicular to the CuO_2 planes. The normalized magnetic susceptibility, $\chi = M/H$ with H = 100 G, are displayed in Fig. 3.16. LBCO95 shows a

peculiar sequence of transitions with T_c ∼32 K, same as shown in Fig. 3.8. Another dip at 27 K coincides with the completion of the LTO to LTLO transition. [27] As expect, the superconductivity is suppressed in the LBCZO95 crystal, which shows a much simpler behavior. There is only one transition at T_c ∼18 K, which is pushed below those in LBCO95 by the Zn.

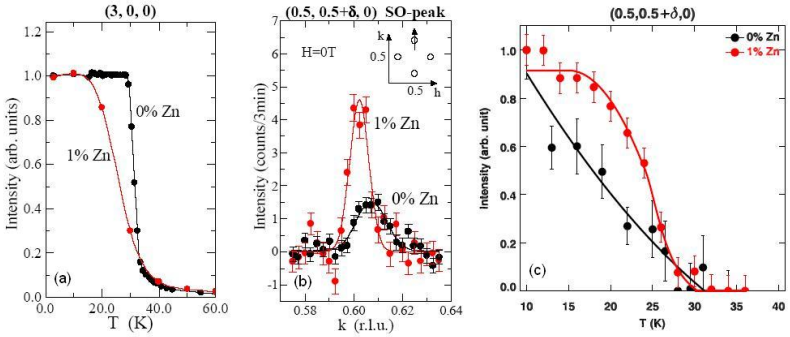

Figure 3.17: Crystal structure and stripe order of pure and Zn doped $La_{1.905}Ba_{0.095}CuO_4$. (a) Normalized integrated intensity of (3,0,0) peak. (d) Linear scans through (0.5, 0.5+δ, 0) spin order peak. Intensity take from difference of 10 K and 50 K data. Inset: spin order pea in ($HK0$) plane. Fig. from Ref. [31]

The LTO to LTLO transition has been analyzed by X-ray diffraction (XRD). [31] The temperature dependence of the (3,0,0) peak intensity, which is allowed in the LTLO phases, but not in the LTO phase, is plotted in Fig. 3.17 (a). The XRD data show a significant change of the curves by Zn. While the transition is very sharp in LBCO95, it is very broad in LBCZO95, even though the onset temperatures are about the same.

The neutron scattering scans through the SO-peak are shown in Fig. 3.17 (b). The weak spin-stripe order peak in LBCO95 is clearly enhanced in Zn-doped one. The stripe-order-peak intensity at 5 K is almost doubled. This enhancement of the peak intensity is consistent with previous works on Zn doped LSCO, which shows that Zn

will increase the spectral weight for low-energy and elastic magnetic scattering. [87, 109, 139] The peak width, corresponding to the spin-spin correlation length, remains roughly the same with and without Zn. The onset temperature of spin order is similar, while the temperature dependence of the spin order is rather different for these two samples, as can be seen from Fig. 3.17 (c). In the Zn-free sample, the stripe-order peak intensity increases slowly with cooling, showing a glassy behavior, while in the 1% Zn doped sample, the intensity increases much more rapidly, as in a second order transition. On the other hand, We have also applied magnetic field on the 1% Zn doped sample, It appears that the 7-T magnetic field can further enhance the peak intensity in the Zn-doped sample at low temperature, similar as for the Zn-free sample. Zn is non-magnetic element, and such a small impurity level should not affect the magnetic order too much itself, but by pinning the stripes, it can reduce the bulk superconductivity effectively.

The charge order peak at q=(2δ,0,8.5), which is the most intense CO reflection observed in LBCO95 by X-ray diffraction, is strangely absent. [27] According to the stripe model, SO and CO are intimately connected [28, 140]. Without charge stripes, which act as anti-phase domain boundaries between spin stripes, the incommensurate SO would disintegrate, or become commensurate. CO seems to be more sensitive to Zn impurities than SO. For charge carriers, Zn impurities act as localization centers, [141] and because of their random distribution may cause significant disorder in the CO pattern. If the associated broadening of the CO-peaks is strong they may become undetectable, because at x=0.095, the CO-peaks are much smaller than at x=0.125.

In summary, we have shown that Zn-doping suppresses the bulk superconductivity and enhances the spin stripe order. The spin stripe order peak intensity is doubled

from that of the Zn-free sample, and the order is developing more rapidly. The Zn doping has little effect on structural transition, while making charge stripe order surprisingly absent. Our study on the Zn-free sample and the Zn-substituted sample on the superconductivity and stripe order clearly demonstrate that spin stripe order is competing with the bulk superconductivity.

Chapter 4

$\mathbf{Fe_{1+\delta}Te_{1-x}Se_x}$

In this Chapter, I will present our experiments results in the $Fe_{1+y}Te_{1-x}Se_x$ system. The results include Se doping, Fe impurities and magnetic field effect on superconductivity and magnetic correlations in this system.

4.1 Phase diagram of $\mathbf{Fe_{1+\delta}Te_{1-x}Se_x}$

The discovery of iron-based superconductors in 2008, provide chance to extend the research of magnetic correlations in high temperature superconductivity. Among four systems of iron-based superconductors, only the "11" system has compounds $FeTe_{1-x}Se_x$ without Arsenic (As). My research works in iron-based superconductors are mainly focussed on the "11" system. The superconductivity in "11" system was first discovered in FeSe with $T_c \approx 8\ K$. [14] The transition temperature was found continuously to increase to $\sim$ 36 K under high pressure. [53] By replacing Se by Te, the T_c under ambient pressure was found to have maximum at $\sim$ 14 K with Te:Se ratio $\sim$ 1:1. [50, 51, 142, 143] No static magnetic order was found in FeSe, while FeTe

was found to be non-superconducting and exhibits long range static magnetic order below $\sim$ 70 K. [144–146] Therefore, FeTe, which is similar to undoped compound in cuprate and other iron-based superconductors, is considered as the parent compound for the "11" system. [32, 146]

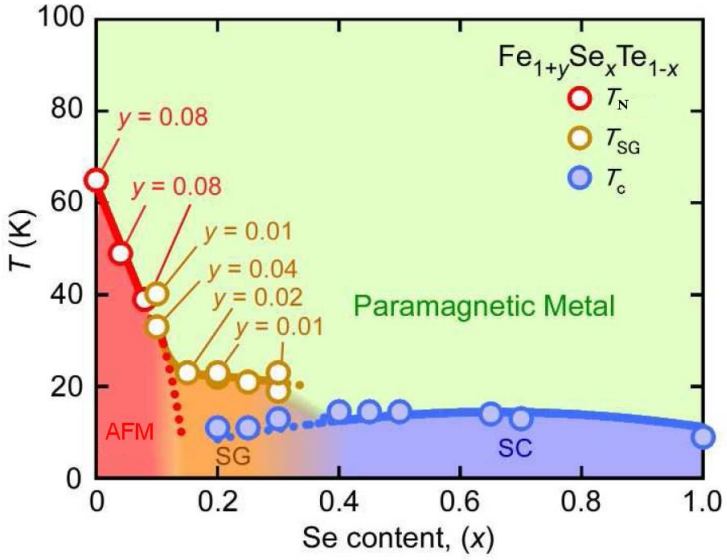

Figure 4.1: Phase diagram of $FeTe_{1-x}Se_x$ as a function of x and T, constructed from single crystal bulk magnetization data. For $x = 100\%$, the data point is from Refs. [14, 32, 33]. The nominal Fe content, $y = 0$ unless it is specified. Temperature labels are described in the text. Fig. from Ref. [34]

The phase diagram for $Fe_{1+\delta}Te_{1-x}Se_x$ based on doping x and temperature T obtained from the bulk susceptibility data of the single crystal samples is shown in Fig. 4.1. [34] The phase diagram clearly shows the trends and the existence of three distinct phases; the modulated antiferromagnetic (AFM) order phase for $x \lesssim 0.1$, the bulk superconducting phase for $x \gtrsim 0.4$, and the intermediate spin-glass phase. [34] In the pure FeTe, the long range commensurate antiferromagnetism abruptly sets in at

the same temperature as the crystal structure change from tetragonal to monoclinic simultaneously in a first-order transition. [146] Doping in the parent compounds gradually suppresses the long range magnetic order and induces superconductivity. In the spin-glass phase, short-range antiferromagnetic order appears to be associated with bulk superconductivity. [34] The transition of short-range magnetism is second-order, with no observable long-range structural phase transition. [34] Upon further doping of Se ions, the system becomes superconducting, for x=0.5 with the superconducting phase transition temperature of T_c=14.5 K. [34, 147, 148]

Neutron scattering studies on $Fe_{1+\delta}Te_{1-x}Se_x$ single crystals have been performed to determine the magnetic correlations in the superconducting phase. [34, 35, 65, 147–154] A "spin resonance" type magnetic excitation was discovered at the in-plane wave vector (0.5,0.5) (using the 2-Fe Tetragonal unit cell) below T_c. [147, 149, 150] The spin resonance and the associated spin gap appear simultaneously, when the system enters the superconducting phase, while the temperature dependence of the intensities of resonance exhibits a superconducting order-parameter-like transition. [149] The spin resonance and gap were also found at the same in-plane wave vector in a number of Iron-based superconductors system. [155–159]. The energy of spin resonance is always observed to scale with T_c around $\hbar\Omega \approx 5k_BT_c$. [149, 155–159] The common features of spin resonance across Iron-based superconductors suggest that the spin resonance and gap are internally associated with superconductivity. The magnetic excitations are believed by some to act as possible glue to pair the electrons. [160–165]

The Iron-based superconductors share similar low-energy magnetic excitations in superconducting phase, however "11" system is quite different in some aspects.

The doping of Te(2+) by Se(2+) in "11" system, which induces superconductivity, has equal valence. The doping here probably brings no extra holes or electrons, which

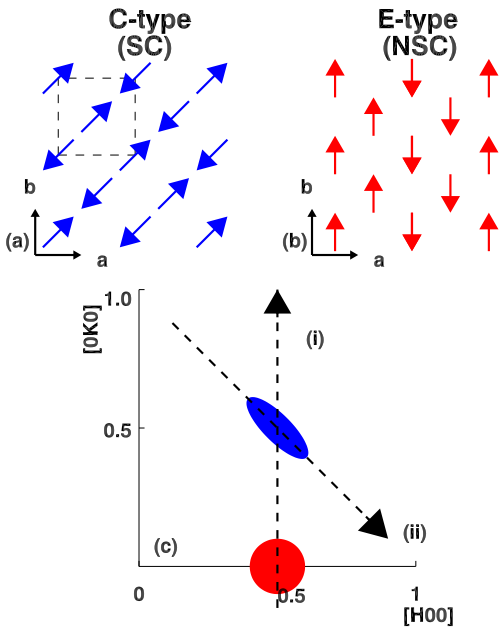

Figure 4.2: (a) Schematic of the "collinear" C-type AF spin structure, with scattering intensities mainly around $(0.5, 0.5)$. The square shows a unit cell with two Fe atoms. (b) Schematic of the "bicollinear" E-type AF spin structure, which contribute mainly to scattering intensities near $(0.5, 0)$. (c) The schematic diagram of the neutron scattering measurements in the $(HK0)$ zone. Dashed lines denote linear scans performed across $(0.5, 0)$ (i) and $(0.5, 0.5)$ (ii) in the text.

is refer as hole or electron doping in other systems. Furthermore, the doping does not directly modify the density of electrons in the conduction bands. The doping dependence of T_c is also quite different. The superconductivity survives even at $x = 100\%$, in the pure FeSe case in the "11" system. [14] While in the cupates and some other iron-based superconductors systems, the doping dependence of T_c always shows a dome shape and superconductivity disappears around doping $x \approx 30\%$. [25, 166, 167]

On the other hand, the magnetic structure in the parent compound FeTe is also

quite different with the superconducting ones. The in-plane antiferromagnetic ordering wave vector in the parent other is found around (0.5,0), which is corresponding to a "bicollinear" or "E-type" spin structure [see Fig. 4.2 (b)], instead of (0.5,0.5) for spin resonance, which is corresponding to a "collinear" or "C-type" spin structure [see Fig. 4.2 (a)]. The magnetic structure in the parent compound of "11" system is also different with the parent compound of other iron-based superconductors system, which have same "collinear" magnetic structure across the system.

4.2 Parent compound $Fe_{1+y}Te$

4.2.1 Evolution of extra Fe in parent compound

For the $Fe_{1+y}Te_{1-x}Se_x$ system, [14] the crystal structure is tetragonal at room temperature shown in Fig. 1.4. Crystallographically there are two available iron sites, one site is fully occupied as Fe(1) in Fig. 1.4, while another site is partially occupied by extra Fe y as Fe(2). [19] The Fe(2) sites are in the middle of each Te/Se square lattice in the Te/Se plane, which alternate with Fe(1) plane along c-axis. In addition, the two inequivalent Fe sites are both magnetically active. [19]

In the pure FeTe, the magnetic and structural transitions occur simultaneously in a first-order transition around 70 K. [19, 146] The structure distorts from tetragonal to monoclinic, while commensurate antiferromagnetic order abruptly sets up at the same temperature. From neutron diffraction experiments, the magnetic ordering wave-vector in the $Fe_{1+y}Te$ is found around q = (0.5,0,0.5). [146] The magnetic structure of Fe(1) sites is "bicollinear" in the ab-plane shown in Fig. 4.2 (b). [144, 148] The moment alignment along the c-axis is antiparallel. From one plane to the next along

the c-axis, magnetic moments simply alternate the direction. [146]

For the higher Fe content, the magnetic order wave vector in the *ab*-plane becomes incommensurate (0.5-δ, 0, 0.5), where the incommensurability δ depends on the extra Fe content. [146] The low temperature crystal structure becomes Orthorhombic instead of monoclinic. [168] On the other hand, the pure FeSe superconducting phase is stoichiometric with y=0. [169] Excess Fe (over $5 \sim 8\%$) in the FeTe/Se superconductors will suppress/destroy bulk superconductivity. [148, 170] The magnetic structure of parent compound in "11" system is different from "1111" and "122" systems. Here we discuss how extra Fe affects the magnetism in the parent compound $Fe_{1+y}Te$.

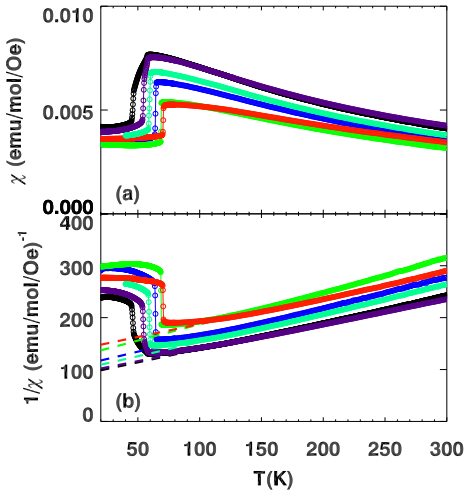

Figure 4.3: ZFC magnetization measured by SQUID for samples with nominal composition: $Fe_{1.00}Te$ (red), $Fe_{1.03}Te$ (green), $Fe_{1.07}Te$ (blue), $Fe_{1.10}Te$ (blue), $Fe_{1.12}Te$ (purple) and $Fe_{1.13}Te$ (black). Magnetic field with 0.1 T was perpendicular to the $a-b$ plane of each sample. (a) Susceptibility, the dashed lines are fits to Curie-Weiss function. (b) Inverse susceptibility, the dashed lines are fits of straight line.

In the present work, we study how the magnetization depends on the amount of extra Fe in parent compound. The single-crystal samples of $Fe_{1+y}Te$ (nominal compositions y = 0.00, 0.03, 0.05, 0.10, 0.12 and 0.13) used in the experiment were grown by a unidirectional solidification method. The exact compositions were determined using inductively coupled plasma spectrometry (ICP). The samples, their exact compositions and and various characteristic properties are listed in Table 4.1. The bulk susceptibility results were obtained using a superconducting quantum interference device (SQUID) magnetometer. Small well-cleaved samples were measured with vertical 0.1 T magnetic field applied perpendicular to the a-b plane.

The ZFC DC magnetic susceptibility χ of $Fe_{1+y}Te$ is plotted in Fig. 4.3 (a). The $\chi(T)$ decreases with increasing temperature in a Curie-Weiss-like fusion in the paramagnetic (PM) state, which is different from the monotonic linear increase of $\chi(T)$ with increasing temperature observed in iron arsenides. [171, 172] The temperature dependence of susceptibility χ in the paramagnetic regime (>100 K) can be well fitted by Curie-Weiss function.

$$\chi = \frac{C}{T - \Theta} \tag{4.1}$$

Where C is the material-specific Curie constant and Θ is the Curie-Weiss temperature. The fitting parameters are listed in Table 4.1 and plotted in Fig. 4.6 (a), (b).

The inverse of ZFC magnetic susceptibility is plotted in Fig. 4.3 (b). The temperature dependence of $1/\chi$ in paramagnetic regime can be well fitted by a straight line. The lines cut the temperature-axis at negative side, which reveals the negative Curie temperature corresponding to antiferromagnetic interactions. On the other hand, the fitting lines are nearly parallel to each other. Since the slope is inversely proportional to the square of the effective magnetic moment, effective moments are similar for all

samples.

Table 4.1: The nominal compositions of samples, the real compositions y, the Curie-Weiss temperature Θ, the effective μ_{eff} and spin moment per Fe derived from the fitting of the magnetic susceptibility data measured along c-axis and *ab*-plane with the modified Curie-Weiss function within the temperature range of 100 K to 300 K.

Sample	y	Θ C (K)	Θ ab (K)	μ_{eff} C (μ_B)	μ_{eff} ab (μ_B)	g C	g ab
$Fe_{1.00}Te$	0.025	-222	-273	3.80	4.25	1.96	2.19
$Fe_{1.03}Te$	0.035	-171	-229	3.46	4.02	1.79	2.07
$Fe_{1.07}Te$	0.062	-166	-192	3.67	4.01	1.89	2.07
$Fe_{1.10}Te$	0.065	-161	-186	3.74	4.07	1.93	2.10
$Fe_{1.12}Te$	0.081	-180	-186	4.04	4.23	2.09	2.19
$Fe_{1.13}Te$	0.097	-158	-165	3.89	4.12	2.01	2.13

The negative Curie-Weiss temperature Θ here suggests dominant antiferromagnetic interactions in these samples. The Curie constant C can be described in the CGS unit system as:

$$C = \frac{N\mu_{eff}^2}{3k_B} \tag{4.2}$$

Where N is the Avogadro number, μ_{eff} is the effective moment and k_B is the Boltzmann's constant. We found the effective magnetic moment is around $\mu_{eff} \sim 3.8\mu_B$, where μ_B is the Bohr magneton. We can obtain the Fe local spin from the effective magnetic moment by:

$$\mu_{eff}^2 = g^2 J(J+1) \tag{4.3}$$

Where g is the Lande g-factor and J is the angular momentum quantum number. Since the only paramagnetic contribution to the magnetic moment comes from the Fe^{2+} ions, assuming $g \approx 2$, the spin moment of each Fe^{2+} will be around 3/2. This is quite surprising, since Fe^{2+} ($4s^0 3d^6$) should give an integer spin moment. If all elec-

trons are localized, which obey Hund's rule, local magnetic moments corresponding to high local spin, S≈2, could be expected. If all electrons belong to coherent bands and are itinerant, local moments should quickly disappear above T_N. So the situation here may be intermediate between the two cases above.

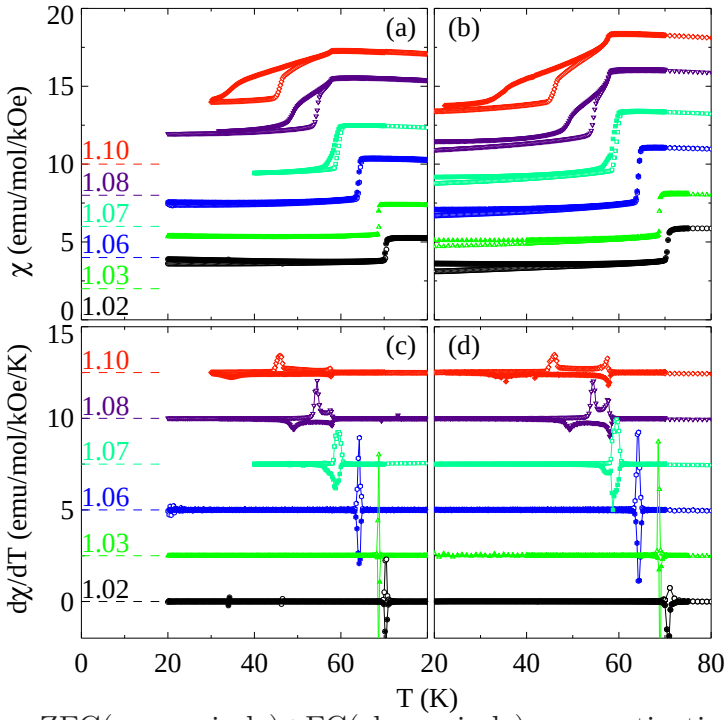

Figure 4.4: ZFC(open circle)+FC(close circle) magnetization measurements by SQUID for samples with nominal composition: $Fe_{1.00}Te$ (red), $Fe_{1.03}Te$ (green), $Fe_{1.07}Te$ (blue), $Fe_{1.10}Te$ (blue), $Fe_{1.12}Te$ (purple) and $Fe_{1.13}Te$ (black). Magnetic field with 0.1 T was perpendicular to the $a-b$ plane of each samples. (a) Susceptibility *vs* temperature. (c) Susceptibility derivative of T ($\partial\chi/\partial T$) *vs* temperature. (b) and (d) for Magnetic field parallel to the $a-b$ plane.

The ZFC+FC magnetic susceptibility χ of $Fe_{1+y}Te$ around the magnetic transition are plotted in Fig. 4.4 (a). For low non-stoichiometric Fe, the ZFC and FC susceptibility are identical and exhibit a sharp first-order magnetic-structure transition. The transition temperature T_N decreases with increasing extra Fe. When the extra Fe is

above critical composition around 0.06, the FC susceptibility clearly deviates from ZFC ones and the transition becomes wider in temperature. $\partial\chi/\partial T$ are plotted in Fig. 4.4 (b) to help determine the transition temperature. The wide transition for high extra Fe reveals two peaks, T_N and T_{N2}, which are also observed in specific heat measurements. [168] The disappearance of the discontinuity in $\partial\chi/\partial T$ suggests change from the first order transition to a continuous probably second order transition at T_N. The second magnetic transition at lower temperature T_{N2} shows clearly ZFC-FC history dependence. This behavior suggests a hysteresis phase between T_N and T_{N2}, whose origin is unclear.

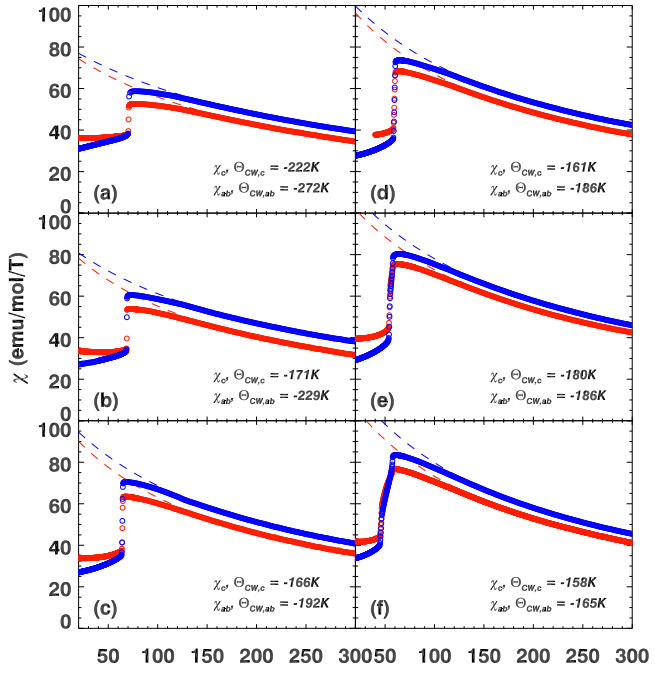

Figure 4.5: ZFC magnetization measurements by SQUID for 0.1 T magnetic field parallel to the *ab* plane (blue) and c-axis (red). For samples with nominal composition: (a) $Fe_{1.00}Te$, (b) $Fe_{1.03}Te$, (c) $Fe_{1.07}Te$, (d) $Fe_{1.10}Te$, (e) $Fe_{1.12}Te$ and (f) $Fe_{1.13}Te$.

We also measured the susceptibility χ_{ab} with magnetic field parallel to *ab* plane

instead of c-axis. The T_N is isotropic as shown in Fig. 4.5. Above T_N, the susceptibility χ_{ab} is systematically larger than χ_c , while χ_{ab} are systematically smaller below T_N. In the paramagnetic region of χ_{ab} can also be fitted by the Curie-Weiss law, the fitting parameters are also listed in Table 4.1 and plotted in Fig. 4.6 (a), (b). There is a consistence of anisotropy of the fitting parameters. There is a systematical increase of Θ_{ab} compared to Θ_c. The effective magnetic moment from χ_{ab}, which is around $4.1\mu_B$, is also systematically larger than from χ_c, which is around $3.8\mu_B$. If we assume the spin S=3/2, the Lande g-factor derived from magnetic moment is also slightly larger with magnetic field parallel to *ab* plane. Both anisotropy of Curie-Weiss temperature Θ and g are proportional to spin-orbit coupling parameters. The anisotropy arises from the spin-orbit coupling and the crystal field, which align spins with respect to the orbital moment.

The summary of the results are plotted in Fig. 4.6. The Curie-Weiss temperature Θ decreases with increasing Fe content y, below 0.06. Above 0.06, Θ is almost independent of increasing extra Fe. The transition temperatures T_N and T_{N2} are plotted in Fig. 4.6 (c). T_N decreases roughly linearly with increasing extra Fe for the whole range we measured. T_{N2} appear for extra Fe above $\approx$0.06 and decreases faster than T_N with increasing y. Some DFT calculations suggest that interstitial Fe donates charge to Te/Se layers, with strong tendency of moment formation on the excess Fe site. [173] The interstitial Fe(2) sites are also magnetically active, Fe(2) sites polarize ferromagnetic spins in nearby square clusters and frustrate the long range 3D "bicollinear" antiferromagnetic order. The magnetic order become weaker in samples with high extra Fe, where T_N decreases.

In conclusion, we have performed a series of magnetic measurements to study the effect of extra Fe y on magnetism of parent compound $Fe_{1+y}Te$. The effective

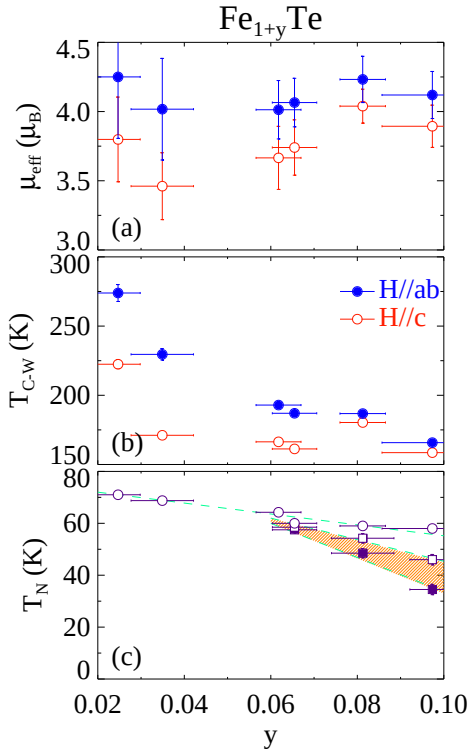

Figure 4.6: (a) Effective magnetic moment per Fe from Curie-Weiss fit for H parallel to the c-axis (red), and parallel to the *ab* plane (blue). (b) Curie-Weiss temperature. (c) Magnetic ordering temperature T_N (circles) and T_{N2} (squares) from ZFC susceptibility derivative of T in Fig. 4.4.

magnetic moment from fitting of paramagnetic susceptibility is almost constant in $Fe_{1+y}Te$ and gives the spin moment around 3/2 per Fe. The magnetic transition temperature T_N decreases nearly linearly with increasing extra Fe content and an anomalous transition appears below T_N for samples above y≈0.06. The extra Fe seems to frustrate the 3D antiferromagnetic order and suppress the long range order in the system.

4.2.2 Magnetic excitations in parent compound

Band structure calculations predict Fe(Te,Se) to be a metal with several bands crossing the Fermi energy. [162, 174, 175] Thus, the importance of strong correlation is in question, while the itinerant electrons and holes existing in small pockets of various bands could play the lead role in determining both transport and magnetic properties. As a result, there are three main scenarios, which are currently considered and debated for iron pnictides and chalcogenides. [176, 177] First, is the localized-moment picture, where strong correlation and Hund coupling win and electrons in parent material are localized, giving rise to large local magnetic moment and high local spin, S≈ 2. Second, is where all electrons belong to coherent bands and are itinerant. In this case local moments involved in low-energy magnetic fluctuations would quickly disappear above the magnetic ordering temperature, becoming a small fraction of Bohr's magneton at T $\sim$ 1.5-2 T_N. Finally, there is also a third possibility, which is intermediate between the two cases described above, where some of d-electrons are indeed itinerant, while the others are localized, giving rise to an intermediate-size local moment.

We have performed inelastic neutron scattering to study magnetic excitations in a $Fe_{1.1}Te$ single crystal. The $Fe_{1.1}Te$ sample used in our measurements was large crystalline piece with mass of 18.45 g. It was cleaved out of a boule grown by the Bridgeman method and consisted of two single crystals mutually misaligned by about 1. The total mosaic was about 2.2 full width at half maximum (FWHM). The sample was mounted on an aluminium sample holder attached to the cold head of the closed-cycle refrigerator in the evacuated scattering chamber of the ARCS spectrometer at the Spallation Neutron Source at Oak Ridge National Laboratory, USA. The sample

ab-plane was nearly vertical, with a direction at about 24 to the horizontal. The c direction was horizontal and aligned parallel to the incident neutron beam.

In direct geometry TOF neutron spectrometers such as ARCS, a pulse of monochromatic neutrons with energy E_i is incident on the sample and then the energy lost or gained by the neutron in the sample is ascertained by measuring the time taken for the neutrons to travel to the detector. By using time-resolved detectors, a large energy transfer range $E < E_i$ is measured in a single pulse. For each E, a slice of the sample's Q = (h, k, l) phase space is probed. We analyzed projections of such slices on the *ab*-plane. Examples are shown in Fig. 4.7 (a). Each (h, k) point there corresponds to a particular value of $l = l(h, k, E, E_i)$, since Q and E are coupled via energy-momentum conservation. Choosing $E_i = 40$ meV we can observe magnetic Bragg peaks arising from 3D magnetic ordering at wave vector $\approx$ (0.5,0,0.5) in the second Brillouin zone, Fig. 4.7(a), because $l(0.5, 1, 0, E_i = 40) \approx 0.5$. Previous studies have established that diffuse quasi-elastic and inelastic scattering is of a good two-dimensional character and has weak or no l-dependence, which can be neglected in our analysis.

Q-independent background (BG) arising from incoherent elastic scattering in the sample (same for all T) was subtracted from all data. It was estimated at several positions where magnetic scattering is nearly absent, and had the form of the resolution-limited (FWHM = 2 meV) Gaussian peak in energy. Fig. 4.7 and 4.8 show the BG subtracted data. Data was normalized by comparing the inelastic scattering intensity from acoustic phonon modes near the structural Bragg reflection τ = (1, 1, 1), which are present in all our data sets, with the calculated one-phonon scattering cross-section, $\frac{d^2\sigma}{d\Omega dE} = \frac{\hbar^2 (Q e_\alpha)^2}{2 M_{unitcell} E_\alpha(Q)} = \frac{|F(Q)|^2}{(1 - exp(-E_\alpha(Q)/(k_B T)))}$. Here $e_\alpha(Q)$ and $E_\alpha(Q)$ are the polarization and the energy of the phonon mode, $M_{unitcell}$ is the mass of $Fe_{1.1}Te$ unit cell, and $F(Q)$ its structure factor determining nuclear Bragg inten-

sities. Calibrations were performed for T = 10 K, 80 K and 300 K and using about 50 selected cuts at each T. The resulting mean value of the normalization coefficient was C_{norm} = (6.02±1.56) mbarn/Steradian/eV/Fe, where error is dominated by the spread between different cuts at each T (the spread between different T is less than 10%).

Fig. 4.7 presents an overview of low-energy magnetic excitations which we have measured in a large single crystal of $Fe_{1.1}Te$ using the ARCS neutron spectrometer at the Spallation Neutron Source (SNS), ORNL. Left column shows neutron intensity as a function of the 2D wave vector Q=(h,k) in the *ab*-plane for elastic, E = 0, (a), and inelastic, E = 7.5 meV, (b), and 20 meV, (c), scattering. Remarkably, general structure of scattering in the form of broad, diffuse peaks centered near (but not exactly at) ($\pm\pi$, 0) and (0, $\pm\pi$) positions, is retained at all energies covered in this measurement (E≤26 meV). Magnetic dynamics of this type is often explained by invoking a system of itinerant electrons, where wave vectors of magnetic excitations are determined by nesting properties of the Fermi surface(s). [175, 178, 179] Such explanation clearly fails for FeTe compounds, since there is no Fermi surface nesting near (π,0) - nesting occurs at (π,π) and (2π,0) [179]. In addition, as we will show later, the observed large magnetic intensity would require at 10 K nearly two fully spin-polarized itinerant electronic bands.

Magnetic excitations in Fig. 4.7 imply robust short-range correlations, whose well-defined real space structure persists in the broad range of time scales, down to 150 fs. In a system of local spins this might be a signature of an emergent degree of freedom, a cooperative spin texture which governs low-energy excited states, such as hexagon loops induced by spin frustration in $ZnCr_2O_4$. [180] We have investigated this conjecture for a number of possible cluster models and found that magnetic

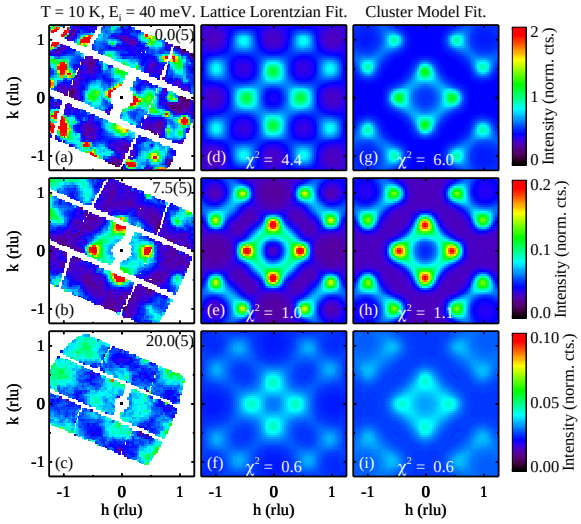

Figure 4.7: Magnetic scattering in $Fe_{1.1}Te$ at T = 10 K and for energy transfers (0 ± 0.5) meV, (7.5 ± 0.5) meV and (20 ± 0.5) meV. Left column, (a)-(c), shows intensity measured in the experiment. (d)-(f) are fits to the cross-section described by four lattice Lorentzian (LL) peaks at (0,±ζ) and (±ζ,0), where $\zeta < 0.5$. Panel (e) also includes Gaussian ring of scattering centered around (0,0), which accounts for the dispersive acoustic mode clearly visible in Fig. 4.8(a). (g)-(i) show two-parameter fits to the checkerboard cluster model, where plaquettes of four co-aligned spins are arranged in a short-range antiferromagnetic structure. All fits account for the magnetic form factor squared $|F_m(Q)|^2$ of Fe^{2+}. Intensity is shown in counts normalized to a unit phase space volume and color scale in each panel is adjusted to emphasize magnetic scattering.

scattering in $Fe_{1.1}Te$ can indeed be very accurately described by a local spin model of this kind. Right column of Fig. 4.7 shows fits of our data to the model where clusters of four ferromagnetically co-aligned nearest-neighbor Fe spins emerge as a new collective degree of freedom, with short-range antiferromagnetic correlations between the clusters. The absence of magnetic scattering along the sides of the square with vertices at (±1,0), (0,±1) provides direct fingerprint of the form factor of the cluster, $S_c(Q) \sim |cos(\pi(h+k)/2)cos(\pi(h-k)/2)|^2$. With only two parameters, the intensity and the correlation length ξ, this fit is nearly as good as the fit to the phenomenological

pattern of factorized Lorentzian peaks on the $Fe_{1.1}Te$ reciprocal lattice, Fig. 4.7, (d)-(f), which was used for quantifying intensity and position of magnetic scattering in Fig. 4.8 and 4.9.

Fig. 4.8 presents the energy dependence of the measured magnetic intensity at h≈0, corresponding to the vertical slice at the center of Fig. 4.7 (a)-(c). It shows striking resonant behavior, with pronounced maximum at E≈7 meV and a weak, acoustic-like mode dispersing from the resonance down to Q = 0. While the origin of the resonance is unclear, it appears at the same energy as spin resonance emerging at (π,π) in superconducting $FeTe_{1-x}Se_x$ samples. [146, 178] Our supplementary measurements have revealed that magnetic scattering pattern in $Fe_{1.1}Te$ begins noticeably changing above ≈ 30 meV, and at high energies has similar shape to that in $FeTe_{1-x}Se_x$, adding to the tantalizing similarity. We find that magnetic bandwidth in $Fe_{1.1}Te$ extends to ≈ 190 meV, an order of magnitude larger than Θ_{C-W}. This is a clear signature of competing interactions, where maximum energy gain resulting from long-range magnetic ordering, which is quantified by Θ_{C-W}, is much smaller than energy involved in coupling individual spin pairs. In $Fe_{1+y}Te$ it likely reflects frustration introduced by the next-nearest neighbor Fe-Te-Fe antiferromagnetic superexchange and ferromagnetic coupling between the nearest neighbors, which favors emergent ferromagnetic clusters, and is probably mediated by itinerant electrons.

It is tempting to pursue further the analogy with emergent excitations of frustrated spins in $ZnCr_2O_4$, where somewhat similar resonance behavior was also observed. There, it arises upon cooling as a result of interaction with lattice degrees of freedom, and is accompanied by a small lattice distortion and a weak long-range antiferromagnetic order. [180] In fact, $Fe_{1+y}Te$ materials also exhibit long-range magnetic order, which is coincident with small monoclinic distortion of the crystal lat-

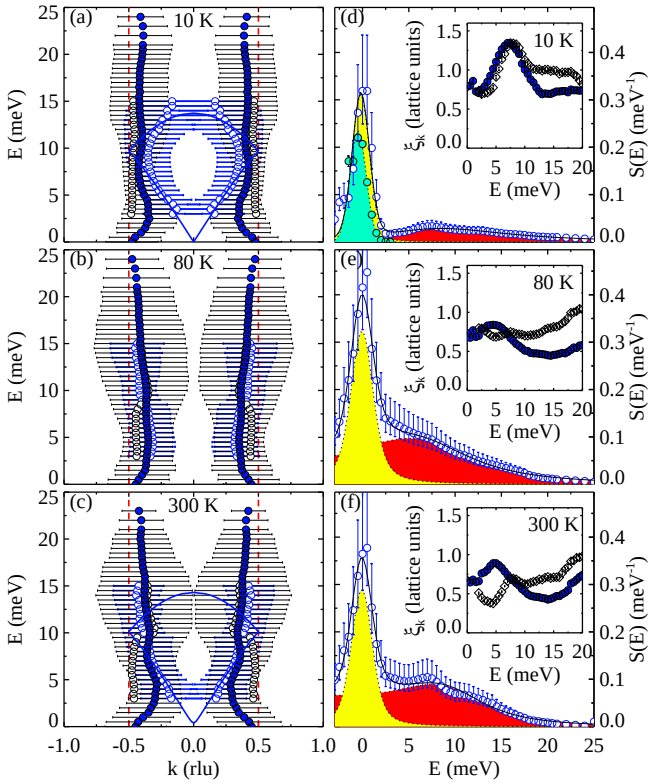

Figure 4.8: Imaginary part of the dynamical magnetic susceptibility, χ"(Q,E), of $Fe_{1.1}Te$ for T = 10 K, 80 K and 300 K, plotted as a function of wave vector along the b-axis and energy. The data, shown in (a), (d), (g), were accumulated for about eight hours for each temperature. χ"(Q,E) was obtained from the measured intensity via the fluctuation-dissipation theorem, $\chi"(Q,E) = \pi(1 - exp(-E/(k_BT)))S(Q,E)$, and is shown in normalized counts as in Fig. 4.7. It can be transformed to the absolute units by multiplying with the normalization prefactor, C_{norm} = (6.02±1.56) mbarn/Steradian/eV/Fe, which was obtained from the measured acoustic phonon intensity (see methods). (b), (e), (h) in the middle column and (c), (f), (i) in the right column show fits to the model consisting of LL peaks plus a dispersive acoustic mode, and to the checkerboard cluster model, respectively, similar to Fig. 4.7.

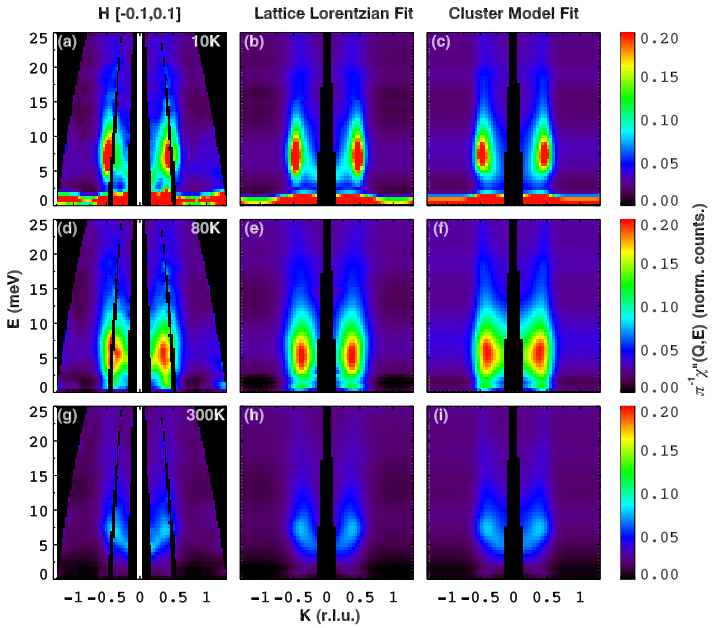

Figure 4.9: Position and intensity of magnetic excitations in $Fe_{1.1}Te$. Filled symbols in panels (a), (c), (e) on the left show peak position at T = 10 K, 80 K and 300 K, respectively, obtained by fitting constant-E slices, such as shown in Fig. 4.7, to a single-component LL cross-section. Wide black error bars show the full width at half maximum (FWHM) of LL peaks. Open symbols are positions of the LL (black) and the ring (blue with error bars) components in the two-component model shown in Fig. 2(b),(e),(h). Solid line in panel (a) shows a fit of the position of a ring mode to an acoustic dispersion, (q) $\sim \sin(\pi k/2)$, folded into small (magnetic) Brillouin zone, [-0.5,0.5]. (b), (d), (f) panels on the right show the integral intensity of magnetic scattering as a function of energy, normalized to meV^{-1} using the measured acoustic phonon intensity (see methods). Error bars include the $\approx 26\%$ uncertainty of absolute normalization. Solid lines are fits used to interpolate the data for the integration and serve as guides for the eye. They consist of a quasi-elastic (QE) central peak (shaded in yellow) and a damped harmonic oscillator (DHO, red). Green-shaded peak in panel (b) shows magnetic Bragg intensity existing below $T_N \approx 60$ K at l = 0.5, which was obtained by fitting Bragg scattering near (-1, 0.5, 0.5) and (-0.5, 1, 0.5), clearly visible in Fig. 4.7 (a), to resolution-limited peaks. Insets show the correlation length in lattice units for the single-component LL (closed circles) and the cluster (open rhombi) models.

tice. [144, 181] At high temperatures both systems have similar effective Curie-Weiss fluctuating moment $4\mu_B$ corresponding to S = 3/2, and in both cases only a fraction of it participates in the long-range antiferromagnetism.

Magnetic order and lattice distortion in our $Fe_{1.1}Te$ sample are weaker than in samples with lower y (≤ 0.06). [144] Ordering occurs at a $\approx$ 10 K lower temperature, $T_N \approx 58$ K, and without sharp discontinuities characteristic of first order transition, which suggests that Fe interstitials are a source of additional frustration. Analysis of magnetic Bragg intensities, which are visible in 10 K data of Fig. 4.7(a) near (± 1, ± 0.5), yields long range ordered moment $\approx 1\mu_B$, about twice smaller than for y=0.05. [144, 181] However, there is also significant amount of elastic or nearly elastic 2D magnetic diffuse scattering near (0,$\pm$0.5), ($\pm$0.5,0) in our sample, which results from frozen, or very slow, short-range correlations between the clusters. Total spectral weight of magnetic Bragg and diffuse scattering adds to $\approx 2.3\mu_B$, which is similar to the ordered moment in samples with lower y. The distribution of magnetic intensity between different components at T = 10 K is shown in Fig. 4.9(d). The total intensity adds to a local magnetic moment of 2.7(7) μ_B, which, assuming Lande factor g = 2, is very close to $\mu_{eff} \approx 2.8\ \mu_B$ expected for local spins S = 1 ($\mu_{eff} = g\mu_B$). Magnetic Bragg peaks account for only $\approx$ 28% of the total intensity, while another$\approx$ 28% are carried by the inelastic spectrum, which again is surprisingly similar to numbers found in $ZnCr_2O_4$.

In order to establish the limits of this similarity and further explore the nature of the resonant behavior of emergent local-spin clusters, we have investigated the temperature dependence of magnetic scattering in $Fe_{1.1}Te$. That such limits must exist is already clear from the fact that our T = 10 K data only account for about a half of magnetic intensity expected for $\approx 4\mu_B$ fluctuating magnetic moments implicated

in CW susceptibility. Magnetic neutron scattering intensity is determined by the product of magnetic form factor, which accounts for atomic magnetization density, and dynamical correlation function S(Q, E), which describes cooperative motions of atomic spins. For a system of local atomic spins S total spectral weight of S(Q, E) obeys sum rule, $\int S(Q,E)dQ^3dE$=S(S+1)=$[\mu_{eff}/(g\mu_B)]^2$, where we omit polarization indices and imply trace over spin polarizations. This means that the integral S(Q, E) spectral weight must remain constant at all temperatures, and that dynamical spin susceptibility χ"(Q, E), which by the fluctuation-dissipation theorem is given by S(Q, E) multiplied by the detailed balance factor, (1-exp(-E/k_BT)), must decrease upon heating, as it is indeed the case in $ZnCr_2O_4$.

The behavior is dramatically different in $Fe_{1.1}Te$. We find that total magnetic INS intensity significantly increases upon heating. This is quite clear from 80 K and 300 K data and the corresponding fit results shown in two bottom rows of Figures 2 and 3. It is also clear from Fig. 4.8(d),(g) and Fig. 4.10(a) that χ"(Q, E) is not governed by the detailed balance factor. Moreover, total magnetic spectral weight at 300 K yields local moments $\approx 3.6\ \mu_B$, in good agreement with the susceptibility data. This would be consistent with a temperature-induced change from local spins S = 1 at 10 K to S = 3/2 at 300 K. This can only occur as a result of an effective change by 1 of the number of localized electrons, and therefore of itinerant band electrons, with the increasing T.

Having made this surprising discovery, we performed a more detailed survey of the temperature dependence of S(Q, E). Fig. 4.10(b) shows the resulting wave vector integrated correlation function S(E) on the logarithmic scale, which emphasizes the changing balance between semi-elastic and inelastic fluctuations. In contrast to the behavior of frustrated local spins in insulator $ZnCr_2O_4$, the resonance character of the

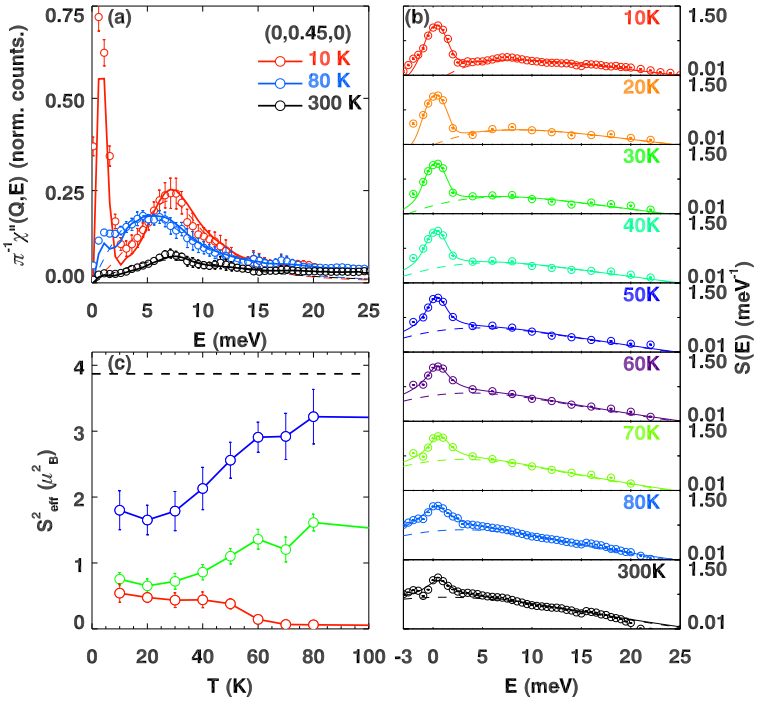

Figure 4.10: Temperature dependence of scattering intensity and the effective Fe spin in $Fe_{1.1}Te$. (a) Cuts from the data in Fig. 4.8(a),(d),(g) show χ"(Q,E) as a function of energy for Q = (0,0.45) at 10 K, 80 K and 300 K, respectively. Lines are from fits shown in Fig. 4.7 (b),(e),(h). (b) temperature dependence of normalized inelastic and quasielastic contributions to S(E), not including magnetic Bragg scattering, $\sim \delta$(E). Solid lines are same as in the right panels of Fig. 4.9, dashed lines show inelastic contribution modeled by DHO. (c) the upper (blue) symbols show temperature dependence of the effective local spin participating in low-energy fluctuations in $Fe_{1.1}Te$ shown in Fig. 4.7- 4.10, as determined by the sum rule, $S^2_{eff} = \int_{-\infty}^{+\infty} S(E)dE$. The bottom (red) symbols quantify the part involved in the long-range static order and appearing in the form of magnetic Bragg scattering at l = 0.5. Green symbols show contribution from the broad diffuse quasi-elastic scattering near (0,$\pm$0.5), ($\pm$0.5,0), i. e. the E = 0 central peak in Fig. 4.10(b). Horizontal dashed line shows $S^2_{eff} \approx 3.9$ obtained from the Curie-Weiss fit of static magnetic susceptibility.

inelastic spectrum is clearly retained at 300 K in $Fe_{1.1}Te$, Fig. 4.8(g), Fig. 4.10(a), and it is this resonance mode which is the main beneficiary of the additional temperature-induced spectral weight. We have also refined the long-range ordered moment at each T and found that its order-parameter-like decrease with the increasing temperature is correlated with an increase in l-independent 2D semi-elastic diffuse scattering, so that sum of the two components is nearly T-independent, Fig. 4.10(c). This suggests that both long-range antiferromagnetism and monoclinic distortion are likely just weak extrinsic perturbations to the emergent spin dynamics, which is governed by much stronger interactions of local spins and itinerant electrons.

Large numbers of theoretical models, involving both local and itinerant electrons, have been put forward in attempts to explain high-temperature superconductivity. Many of them suggested local spin frustration and emergent behavior as important ingredients in HTSC physics, and some features of these behaviors were observed in model spin systems. Others treated emerging magnetism as a signature of collective instability of the itinerant electrons and questioned the relevance of local spin picture. Here for the first time we present direct experimental evidence of both presence and strong and non-trivial coupling of emergent local spin magnetism and itinerant electrons in a system bearing immediate relation to HTSC. While ferromagnetic nature of emergent local spin clusters which govern magnetic fluctuations in $Fe_{1.1}Te$ up to $\sim$ 30 meV is clearly not favorable for the HTSC, slight change of electronic band structure in $FeTe_{1-x}Se_x$ perhaps modifies emergent modes and their interaction with itinerant electrons in a manner inductive for superconductivity. Never before to our knowledge has temperature enhanced magnetic response of localized electrons, such as we found in iron telluride, been observed. Our findings cannot be explained in a perturbation framework starting from either local or itinerant point, and call for

devising an entirely new theoretical paradigm.

4.3 Magnetic correlations around optimal-doping

4.3.1 Short-range incommensurate magnetic ordering near superconducting boundary

In this section, to address the evolution of the magnetic correlations with Se concentration, we have performed elastic neutron scattering and magnetization measurements on high quality single crystals with different Fe and Se contents. We show that there is short-range incommensurate magnetic order in both $Fe_{1.07}Te_{0.75}Se_{0.25}$ and $FeTe_{0.7}Se_{0.3}$ at low temperature. Broad magnetic peaks appear at positions slightly displaced from the antiferromagnetic (AFM) wave-vector $(0.5, 0, 0.5)$ in both samples when cooled below $\lesssim$40 K. The peak intensity increases with further cooling and persists into the superconducting phase. The magnetic peak intensity drops with more Se and less Fe content, and with strengthening superconductivity.

Single crystals with nice (001) cleavage planes were grown by a unidirectional solidification method with nominal compositions of $Fe_{1.07}Te_{0.75}Se_{0.25}$ and $FeTe_{0.7}Se_{0.3}$ and respective masses of 4.7 and 7.2 g. Neutron scattering experiments were carried out on the triple-axis spectrometer BT-9 located at the NIST Center for Neutron Research. The scattering plane $(H0L)$ is defined by two vectors [100] and [001] in tetragonal notation. The lattice constants for both samples are $a = b = 3.80(8)$ Å, and $c = 6.14(7)$ Å.

The bulk magnetization was characterized using a superconducting quantum interference device (SQUID) magnetometer. In the magnetization measurements, each

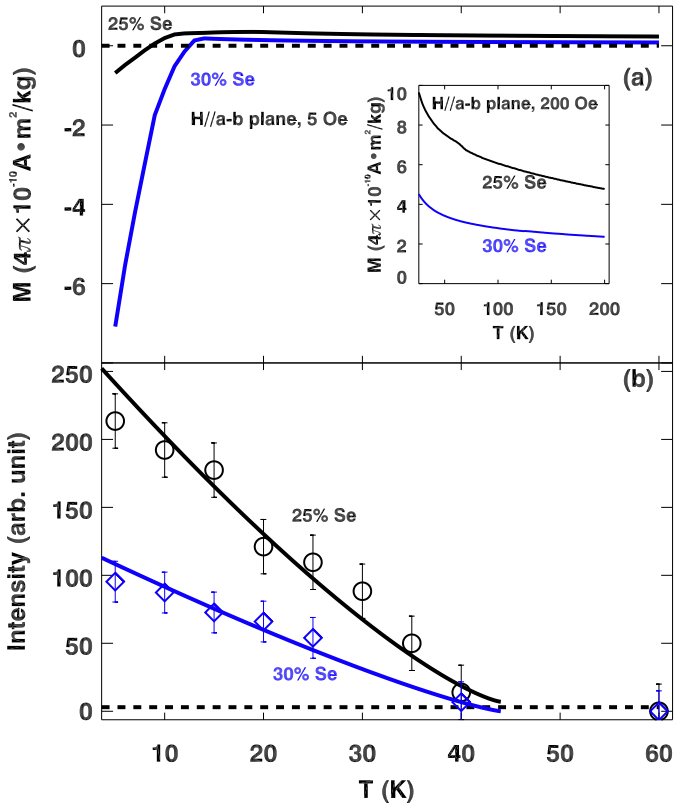

Figure 4.11: (a) ZFC magnetization, and (b) background subtracted magnetic peak intensity measured along [100] (normalized to the sample mass) as a function of temperature for $Fe_{1.07}Te_{0.75}Se_{0.25}$, and $FeTe_{0.7}Se_{0.3}$. Error bars indicate one standard deviation assuming Poisson statistics. Lines through data are guides for the eyes.

sample was oriented so that the (001) plane was parallel to the magnetic field. The zero-field-cooling (ZFC) magnetization *vs.* temperature for each sample is shown in Fig. 4.11(a), where one can see that the 25% Se sample only shows a trace of superconductivity, while the 30% Se sample clearly has a $T_c \sim 13$ K. We estimate that the superconducting volume fraction for the latter sample is $\sim 1\%$. The inset of Fig. 4.11(a) shows that the paramagnetic magnetization grows on cooling, and is greater in the sample with less Se (and more Fe). The paramagnetic response does not follow simple Curie-Weiss behavior, so it is not possible to make a meaningful

estimate of effective magnetic moments. For the 25% Se sample, there is a shoulder at $\sim$ 60 K which could be due to 2–3% of $Fe_{1+\delta}Te$ as a second phase, which has a magnetic phase transition temperature of $\sim$65 K. [144]

In our elastic neutron scattering measurements, each sample was aligned on the (200) and (001) nuclear Bragg peaks with an accuracy and reproducibility in longitudinal wave vector of better than 0.005 r.l.u.. For the magnetic peaks, linear scans were performed along [100] and [001] directions at various temperatures. The temperature dependence of the peak intensity is summarized in Fig. 4.11(b), and representative scans are shown in Fig. 4.12. No net peak intensity is observed at 60 K, but a weak magnetic peak appears at slightly lower temperature, growing in intensity with further cooling. For $Fe_{1.07}Te_{0.75}Se_{0.25}$, the magnetic structure is clearly incommensurate, and the peak position is determined to be $(0.5-\epsilon, 0, 0.5)$, with $\epsilon = 0.04$. From Fig. 4.12(a), we did not observe a peak at $(0.5+\epsilon, 0, 0.5)$. For $FeTe_{0.7}Se_{0.3}$, the magnetic peak center is at (0.48,0,0.5), although this differs from the commensurate position by less than the peak width. Our observations are qualitatively consistent with the previous result[146] for $Fe_{1.08}Te_{0.67}Se_{0.33}$, where the magnetic peak is at (0.438,0,0.5); it appears that both the Fe and Se concentrations impact the ordering wave-vector. We have also searched for SDW order around (0.5,0.5,0.5) in the (HHL) zone, but no evidence of magnetic peaks was found.

At 5 K, the peak width for $Fe_{1.07}Te_{0.75}Se_{0.25}$ [100] scan is 0.10 r.l.u., which corresponds to a correlation length of 6.1(1) Å. The width along [001] is 0.20 r.l.u., giving a correlation length of 4.9(1) Å. As can be seen from Fig. 4.12, the peaks for $FeTe_{0.7}Se_{0.3}$ along [100] and [001] are broader than their counterparts for $Fe_{1.07}Te_{0.75}Se_{0.25}$, and the correlation lengths are determined to be 3.8(1) Å along [100] and 3.3(1) Å along [001]. Also, from Fig. 4.11(b), one can see that the magnetic peak intensity for

$Fe_{1.07}Te_{0.75}Se_{0.25}$ is always higher than the other one. Although the SDW order is short-ranged in both compounds, and starts at around the same temperature, ~ 40 K, the order is apparently stronger in the 25% Se sample.

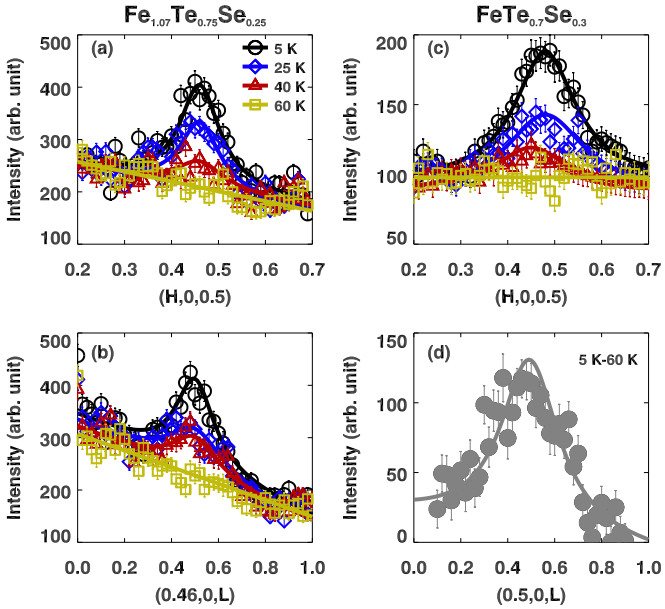

Figure 4.12: Short-range magnetic order in $Fe_{1+\delta}Te_{1-x}Se_x$. The left and right columns show the magnetic peak profiles for $Fe_{1.07}Te_{0.75}Se_{0.25}$ and $FeTe_{0.7}Se_{0.3}$, respectively. Top and bottom rows are scans along [100] and [001] respectively. (a), (b), and (c) are data taken at various temperatures. For the 30% Se sample, there is a temperature-independent spurious peak in the [001] scans, so in (d) we only plot 5 K data with the 60-K scan subtracted. All data are taken with 1 minute counting time and then normalized to the sample mass. Error bars represent the square root of the total counts. The lines are fits to the data using Lorentzian functions.

The magnetic structure of the parent compound $Fe_{1+\delta}Te$ can be described by the schematic diagram in the inset of Fig. 4.13(a), which is adopted from Refs. [144, 146]. Here the magnetic structure consists of two spin sublattices. The spins in both sublattices are found to be aligned along b-axis. Within each sublattice, the spins have an antiferromagnetic alignment along a and c-axes, and ferromagnetic along the

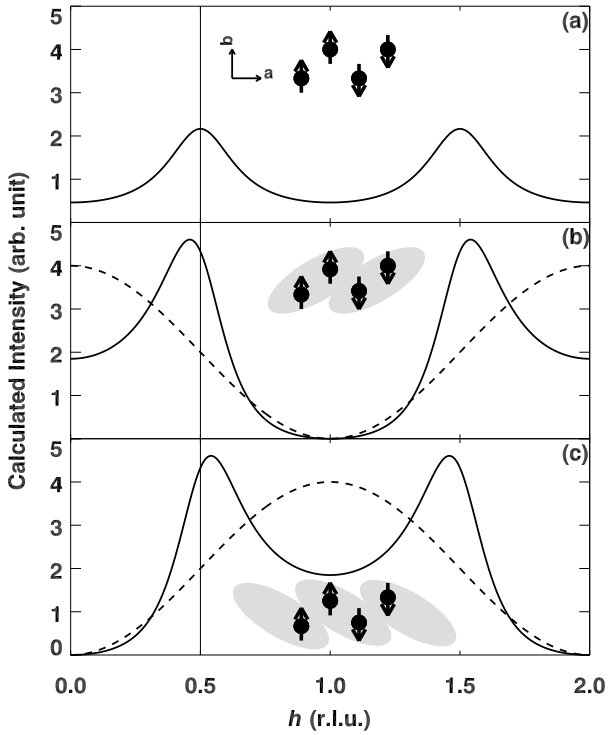

Figure 4.13: (a) Inset shows the commensurate magnetic unit cell within a single layer of $Fe_{1+\delta}Te$, with spin arrangements in a-b plane; solid line shows the calculated scattered intensity assuming uniform exponential decay of spin correlations. (b) Dashed line shows the magnetic structure factor $|F|^2$ and solid line shows calculated intensity for exponential decay of correlations between ferromagnetic spin pairs (inset). (c) Same as (b) but for exponential decay of correlations between antiferromagnetic spin pairs.

b-axis. The spins have a small out-of-plane component, but here, for simplicity, we are only considering the components in the a–b plane. With low excess Fe, [144] this configuration gives rise to magnetic Bragg peaks at the commensurate AFM wave-vector (0.5,0,0.5). The extra Fe is considered to reside in the interstitial sites of the Te/Se atoms. [146] With more excess Fe, the ordering wave-vector becomes incommensurate, which can be explained by a modulation of the ordered moment size and orientation, propagating along the a-axis. [146] The connection between

excess Fe and the transition from commensurate to incommensurate order has been modeled theoretically. [182]

With Se doping, the magnetic order is depressed and becomes short ranged. It is intriguing that magnetic order can survive without a lowering of the lattice symmetry from tetragonal, although perhaps there are local symmetry reductions on the scale of the magnetic correlation length. The incommensurability is also interesting. A uniform sinusoidal modulation of the spin directions or magnitudes will give incommensurate peaks at $(0.5 \pm \epsilon, 0, 0.5)$, whereas we see a peak only on the $-\epsilon$ side. One can model this with phase shifted modulations on the two sublattices, but the modulation length required to describe the incommensurability is much greater than the correlation length.

We have found that a simple description of the incommensurability can be obtained when the decay of correlations between ferromagnetic nearest-neighbor spins is different from that of antiferromagnetic spin neighbors. We will consider correlations only along the modulation direction within an a–b plane, and assume that they are independent of correlations in the orthogonal directions. Let us break the spin system into perfectly correlated nearest-neighbor pairs, with exponential decay of the spin correlations from one pair to the next along the a-axis. The neutron scattering intensity can then be expressed as [183]

$$I \propto |F|^2 \frac{1 - p^2}{1 + p^2 - 2p\cos(2\pi h)}, \tag{4.4}$$

where F is the structure factor for the selected pair of spins, h is the wave-vector

component along the a-axis, and

$$p = -e^{-a/\xi}; \tag{4.5}$$

p is the correlation function between neighboring pairs, where the negative sign suggests that the inter-pair corrlation is antiferromagnetic; and ξ is the correlation length. (In all cases discussed below, we set $\xi = a$.)

Let us first consider the case of ferromagnetic spin pairs with exponentially decaying correlations between pairs, as illustrated in Fig. 4.13(b). The structure factor for this case corresponds to

$$|F|^2 = 4\cos^2(\tfrac{1}{2}\pi h), \tag{4.6}$$

as indicated by the dashed line in Fig. 4.13(b). Plugging this into Eq. (4.4) gives the solid line shown in Fig. 4.13(b). Note that the calculated peaks are incommensurate, with the peak near $h = 0.5$ shifted to lower h. Alternatively, we can start with an antiferromagnetic spin pair, in which case

$$|F|^2 = 4\sin^2(\tfrac{1}{2}\pi h). \tag{4.7}$$

This yields the result shown in Fig. 4.13(c), with the peaks shifted in the opposite direction. If the decay of correlations is identical for ferromagnetic and antiferromagnetic nearest neighbors, then we can average over these two cases, obtaining $|F|^2 = 2$; the resulting commensurate peaks are shown in Fig. 4.13(a).

Our experimental results look similar to Fig. 4.13(b). This suggests that the ferromagnetic correlations are stronger than the antiferromagnetic ones. For the model illustrated in Fig. 4.13(b), the incommensurability grows as the correlation

length gets shorter. The trend in our two samples does not follow this relationship; however, one could describe a more general relationship between the ferromagnetic and antiferromagnetic correlations by taking a weighted average of Eqs. (4.6) and (4.7).

In summary, we have observed short-range magnetic order in $Fe_{1.07}Te_{0.75}Se_{0.25}$ and $FeTe_{0.7}Se_{0.3}$. In both samples, the magnetic order is incommensurate and only observed on one side of the commensurate wave-vector (0.5,0,0.5), which is likely a result of the imbalance of ferromagnetic/antiferromagnetic correlations between neighboring spins. The parent compound $Fe_{1+\delta}Te$ is not superconducting, [144, 146] and the optimally doped sample with 50% Se has no static magnetic order [148, 149]. Our samples have Se content lying in the middle, where we see that with larger Se doping, the SDW order becomes weaker, while the superconductivity is enhanced. This could imply the coexistence and competition between SDW order and superconductivity in this system, similar to other Fe-based [21, 163, 166, 184, 185] and cuprate superconductors [25, 106, 186]. Interestingly, in the $Fe_{1+\delta}Te_{1-x}Se_x$ system, the SDW order and superconductivity can be tuned not only by doping Se, but also by adjusting the Fe content. [145, 169, 187] It has been reported that the excess Fe acts as a magnetic electron donor, [187] suppresses the superconductivity, and induces a weakly localized electronic state. [188] Our results are completely consistent with these results—with less Fe and more Se, the SDW order is weaker; with more excess Fe and less Se, superconductivity is weaker, but to really distinguish the role of Fe and Se, samples only varying one element are certainly required for future work. We also note that recent studies of superconducting $FeTe_{0.6}Se_{0.4}$ (Ref. [149]) and $FeTe_{0.5}Se_{0.5}$ (Ref. [189]) show evidence of a spin gap and resonance peak at the wave vector $(0.5, 0.5, L)$. It should be interesting to study how the magnetic correlations

evolve with Se concentration between 30% and 40%.

4.3.2 Evolution of spin fluctuations depend on doping and extra Fe

Since the spin "resonance" in the superconducting compounds occur around the in-plane wave vector (0.5,0.5) , (using the 2-Fe unit cell), suggesting a "collinear" or "C-type" AF structure [see Fig. 4.2 (a)]. [144, 190, 191] While the parent compound of "11" system has a "bicollinear" or "E-type" AF order around the in-plane wave vector (0.5, 0) [see Fig. 4.2(b)], [35, 144, 146, 154, 190] Therefore, understanding how the magnetic structure (static or dynamic) evolves from the E-type bicollinear configuration of the parent compound to the C-type collinear configuration in the superconducting region in the 1:1 system is an important problem.

We present our work using neutron scattering to probe the magnetic order/fluctuations in a few samples from the 1:1 family for Se dopings ranging from 30% to 50% and with varying superconducting properties, the latter anticorrelated with excess Fe content. Our results suggest that static magnetic order exists in all non-superconducting samples. (Here, by non-superconducting we mean an absence of bulk superconductivity.) This order is short-ranged and occurs at in-plane wave vectors $\mathbf{Q}$ of the type $(0.5, 0)$. For the fully superconducting samples, no static magnetic order is found. With the disappearance of static magnetic order, the associated low energy magnetic excitations near $(0.5, 0)$ also go away, as one might expect. Magnetic excitations near $(0.5, 0.5)$ gradually become dominant as the material becomes more superconducting. While Se doping does play an essential role, it is clearly not the only determining factor regarding the superconductivity and the magnetic correlations. Samples with

similar Se doping but differing in Fe content can have very different superconducting properties and corresponding magnetic structures/fluctuations. Our results clearly indicate that the static short-range magnetic order competes with and suppresses superconductivity. Superconductivity only appears when the system evolves toward fluctuating magnetic correlations characterized by $\mathbf{Q} = (0.5, 0.5)$, which appears to be universal across all known Fe-based superconductor families. The situation has similarities to that in the high-T_c cuprate systems where a "resonance" is also detected in the magnetic excitation spectrum for various cuprate families, [90, 192–195] and static antiferromagnetic order suppresses bulk superconductivity. However, there is a clear difference between the two families: the local magnetic correlations in the cuprate system are always based on a G-type antiferromagnetic configuration, [190] even when spatial segregation occurs. [28, 29, 80, 124] The versatility of spin configurations in the Fe-based superconductor families is therefore very different and extremely interesting.

Table 4.2: List of the $Fe_{1+\delta}Se_xTe_{1-x}$ samples used in our measurements, with their composition (δ, x), superconducting transition temperature (T_c), room-temperature lattice parameters (from powder X-ray diffraction), crystal mass and ordered moment of Fe ion. The absolute value of ordered moment in NSC30 is undetermined because the measurements necessary for absolute normalization were not performed on that sample.

Sample	δ	x	T_c (K)	a (Å)	c (Å)	mass (g)	moment per Fe (μ_B)
SC30	0.00 ± 0.03	0.3	14	3.815	6.140	12.7	0.10
NSC30[a]	0.05 ± 0.03	0.3	–	3.808	6.120	7.4	unknown
SC50[b]	0.00 ± 0.03	0.5	14	3.811	6.129	9.0	$\sim$0
NSC45	0.05 ± 0.03	0.45	–	3.807	6.047	6.4	0.15

The single-crystal samples used in the experiment were grown by a unidirectional

solidification method. The samples, their compositions (nominal compositions, based on starting materials, with error bars for δ reflecting anticipated range of actual composition), and various characteristic properties are listed in Table 4.2. The bulk susceptibility results in Fig. 4.14 were obtained using a superconducting quantum interference device (SQUID) magnetometer. Small well-cleaved samples were measured with vertical 5 Oe magnetic field applied perpendicular to the a-b plane. From the magnetization measurements we can see that, although both superconducting samples show evidence of diamagnetic response at around 14 K, SC50 is clearly better in quality as far as superconducting volume fraction is concerned. [Note that our zero-field-cooling (ZFC) measurements provide only an upper limit on superconducting volume fraction.] With a considerable portion of its bulk volume being non-superconducting, it is possible that there is phase separation in SC30. In fact, when measuring different small pieces ($\sim$ 1 mm size) from the same SC30 sample, the superconducting volume can vary from $\lesssim 10\%$ to $\sim 80\%$, suggesting that the superconducting and nonsuperconducting phases could be macroscopically separated in this sample. The other samples, NSC30 and NSC45, are mostly non-superconducting, with no more than 1% of the volume giving a superconducting response.

Neutron scattering experiments have been carried out on the triple-axis spectrometers SPINS (inelastic scattering measurements of magnetic excitations for SC30 and NSC30, and all elastic measurements for static magnetic order), and BT-7 (inelastic scattering measurements for SC50 and NSC45) located at the NIST Center for Neutron Research. We used horizontal beam collimations of Guide-open-S-80′-240′ (S represents "sample") for the inelastic scattering measurements on SPINS with fixed final energy of 5 meV and a cooled Be filter after the sample to reduce higher-order neutrons; collimations of Guide-80′-S-80′-240′ were used for the elastic measurements

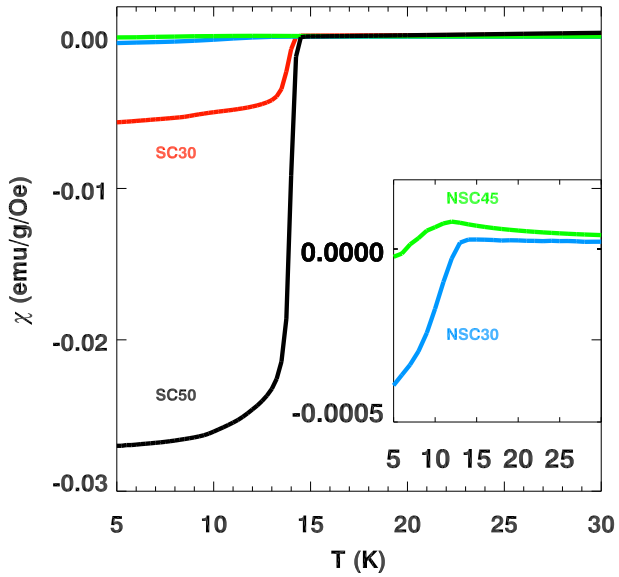

Figure 4.14: ZFC magnetization measurements by SQUID for SC30 (red), NSC30 (blue), NSC45 (green) and SC50 (black). The inset shows the same data from the non-superconducting samples with different scale.

on SPINS, with an additional Be filter before the sample. At BT7, we used beam collimations of open-50′-S-50′-240′ with fixed final energy of 14.7 meV and two pyrolytic graphite filters after the sample. The inelastic scattering measurements have been performed in the $(HK0)$ scattering plane, as indicated in Fig. 4.2(c). The data are described in reciprocal lattice units (r.l.u.) of $(a^*, b^*, c^*) = (2\pi/a, 2\pi/b, 2\pi/c)$. The elastic scattering measurements have been taken in the $(H0L)$ scattering plane instead, since the order in the parent compound occurs at half integer L values (AF order along the c-axis). All data have been normalized into absolute units ($\mu_B{}^2$·eV^{-1}/Fe), using incoherent elastic scattering intensities from the samples.

The static long-range magnetic order in the parent compound $Fe_{1+\delta}Te$ appears

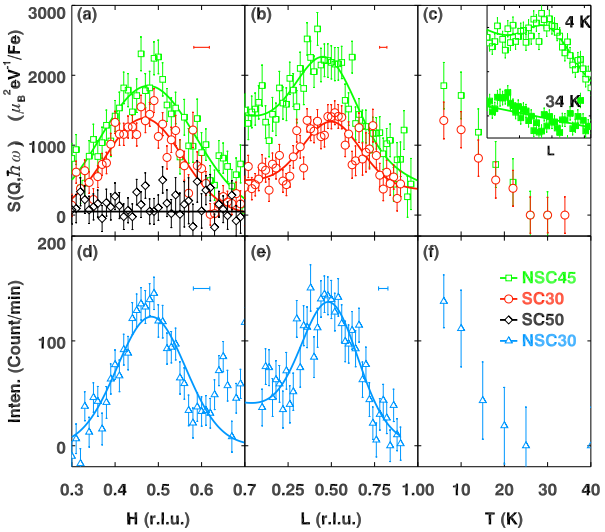

Figure 4.15: Elastic neutron scattering measurements performed on SC30 (red circle), NSC30 (blue triangle), NSC45 (green square) and SC50 (black diamond) near $(0.5, 0, 0.5)$. (a, d) Intensity profiles along [100] direction (H-scans) at $T = 4$ K; (b, e) Scans along [001] direction (L-scans) at $T = 4$ K. The horizontal bars represent the H and L resolution at SPINS (a, b) and BT-9 (d, e). The solid lines are based on least square fits to the data with single Gaussian peak and sloping background. (c) shows the magnetic peak intensity (from fitted Gaussian peak intensity) at $(0.5, 0, 0.5)$ vs. temperature. Corresponding scans measured at $T = 34$ K are used as background, and have been subtracted from all the data shown. The inset in (c) shows the 4 K (open) and 34 K (close) raw data used in (b) for NSC45. (d-f) Data from Ref. [35]). The error bars represent the square root of the number of counts.

near $(0.5, 0, 0.5)$, corresponding to bicollinear E-type AF structure. With small Se doping, it has been observed that the order gradually becomes short-ranged [34, 35, 154] and eventually disappears. Our results, however, suggest that the order can still remain with relatively large Se dopings (and excess Fe).

We performed elastic magnetic scattering measurements on all samples. For the SC50 sample, there is no elastic magnetic intensity at $(0.5, 0, 0.5)$, while magnetic peaks are observed for all three other samples. In Fig. 4.15, we plot H and L scans

through this AF wave-vector for all samples at $T = 4$ K. The measurements for NSC30, Fig 4.15 (d)–(f), are from a previous report (see Fig. 2 of Ref. [35]). Unfortunately, no absolute normalization was performed on that sample. The temperature dependence [Fig. 4.15 (c) and (f)] for the NSC45, SC30, and NSC30 samples are very similar, with the order gradually disappearing with heating. [For the SC50 sample, there is no elastic scattering intensity as shown in Fig. 4.15 (a) for the whole temperature range measured.] The H and L scans performed at higher temperature (T=34 K) show no peak structure and are therefore used as backgrounds to be subtracted from the data. All peaks are much broader than the resolution, indicating the short-ranged nature of the magnetic order. The H-scans are peaked near but not exactly at $H = 0.5$, similar to the results reported for NSC30 and another sample with 27% Se doping. [35] The L-scans, however, are qualitatively different. In previous reports on lower Se doped 1:1 compounds, [35, 65] the L-scan peaks around $L = 0.5$, and intensity always goes to zero at $L = 0$. In those cases, the magnetic order is always AF along the L-direction, whether short- or long-ranged. Here we see that after background subtraction, the scattering intensity at $L = 0$ is still appreciable. This suggests that although the magnetic order still has a modulation along the L-direction, which peaks around $L = 0.5$, favoring an AF configuration between Fe planes, the order has become much more two-dimensional. In the NSC45 sample, the 3D long-range bicollinear AF magnetic order of the parent compound has not been entirely destroyed, but rather greatly reduced to 2D short-range order. The ordered moment per Fe is 0.15(4) μ_B, much less than the value in the parent compound with long-range order. [146] It is, nevertheless, enough to destroy superconductivity. With this static magnetic order present, even with 45% Se doping, bulk superconductivity is still not achieved. In the SC30 sample, although the sample does show a supercon-

ducting phase transition at around 14 K, the superconducting volume is smaller than for the SC50 sample. The ordered moment is about 0.10(1) μ_B/Fe, smaller than that in the NSC45 sample, indicating that this order may be coming from only part of the sample.

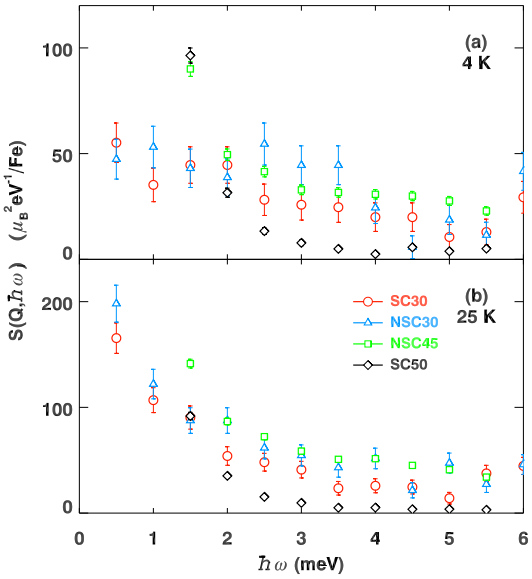

Figure 4.16: Constant-Q scans at $(0.5, 0, 0)$ taken at (a) 4 K (1.5 K for SC30 and NSC30) and (b) 25 K. A background, determined from constant-energy scans as in Fig. 4.17 has been subtracted from all data sets. The error bars correspond to the square root of the number of counts.

With the tendency towards developing static short-range magnetic order in the non-superconducting samples, it is natural to expect to see magnetic excitation spectra around the (0.5,0) in-plane wave vector as well. Previous work has shown that the energy dispersion and intensity modulation along the L direction for magnetic excitations in the 1:1 compound is small. [65, 149] We therefore chose to perform the inelastic scattering measurements in the $(HK0)$ plane. In Figs. 4.16 and 4.17, we

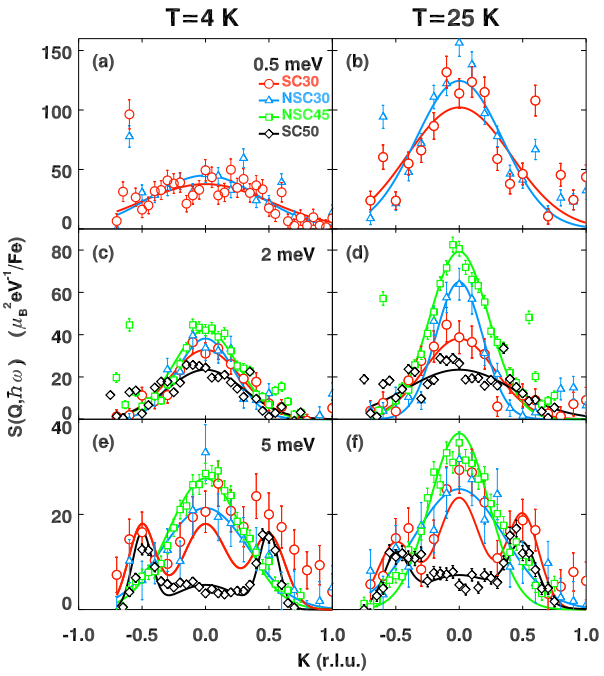

Figure 4.17: Magnetic excitations for $Fe_{1+\delta}Se_xTe_{1-x}$ measured around $(0.5, 0, 0)$. The left and right columns show the magnetic peak profiles for 4 K (1.5 K for SC30 and NSC30) and 25 K respectively. Constant-energy scans at $(0.5, K, 0)$ [as shown by (i) in Fig. 4.2 (c)] at $\hbar\omega$ = (a-b) 0.5 meV, (c-d) 2 meV and (e-f) 5 meV. The solid lines are based on least square fits to the data with one main Gaussian peak at K=0, plus sometimes two small Gaussian peaks at K=$\pm$0.5, which represent intensities from Q=(0.5,0.5), and a constant background. The fitted K-independent background has been subtracted from all data sets. The error bars correspond to the square root of the number of counts.

plot our results taken near $(0.5, 0, 0)$. Figure 4.16 shows energy scans at $(0.5, 0, 0)$ for T = 4 K and 25 K. Measurements for NSC45 and SC50 were taken on BT7 with a relatively coarse energy resolution (FWHM $\sim$ 1.7meV) compared to those on SPINS (NSC30 and SC30, FWHM $\sim$ 0.3 meV), and have a large, resolution-limited tail from scattering at $\hbar\omega = 0$. Constant-energy scans at $\hbar\omega$ = 0.5, 2, and 5 meV [Fig. 4.17 (a) to (f)] along the K direction across $(0.5, 0, 0)$ clearly show that for NSC30, SC30 and NSC45, there is significant spectral weight at low energies here. For both 30%-Se

samples, where we have measurements with higher energy resolution, one can see that the intensity at $\hbar\omega = 0.5$ meV increases on warming from 4 K to 25 K. The increase is much less pronounced at $\hbar\omega = 5$ meV. This behavior is likely due to a transfer of spectral weight from the elastic peak into low energy channels when the static order dissolves with heating. For SC50, the low-energy spin excitations near $(0.5, 0, 0)$ are weak, and not strongly temperature dependent, which is consistent with the fact that there is no static order near (0.5,0) in this sample. The two small peaks near $K = \pm 0.5$ observed from samples SC30 and SC50 at $\hbar\omega = 5$ meV, suggest that there is additional spectral weight developing near the (0.5,0.5) wave-vector, corresponding to dynamic collinear spin correlations in the superconducting samples.

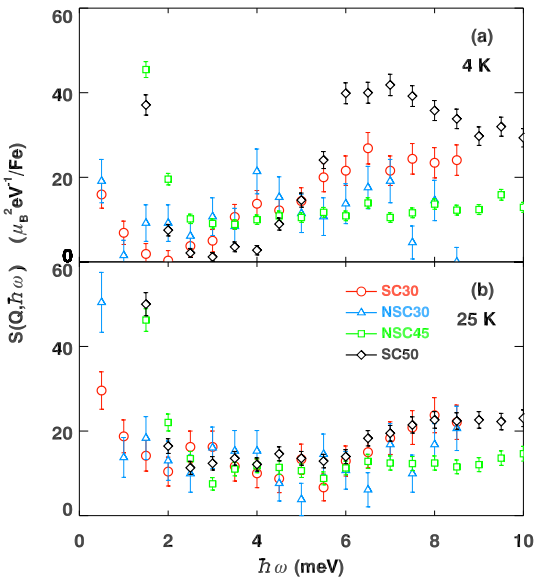

Figure 4.18: Constant-Q scans at $(0.5, 0.5, 0)$ taken at (a) 4 K (1.5 K for SC30 and NSC30) and (b) 25 K. A background, determined from constant-energy scans as in Fig. 4.19 has been subtracted from all data sets. The error bars corresonds to the square root of the number of counts.

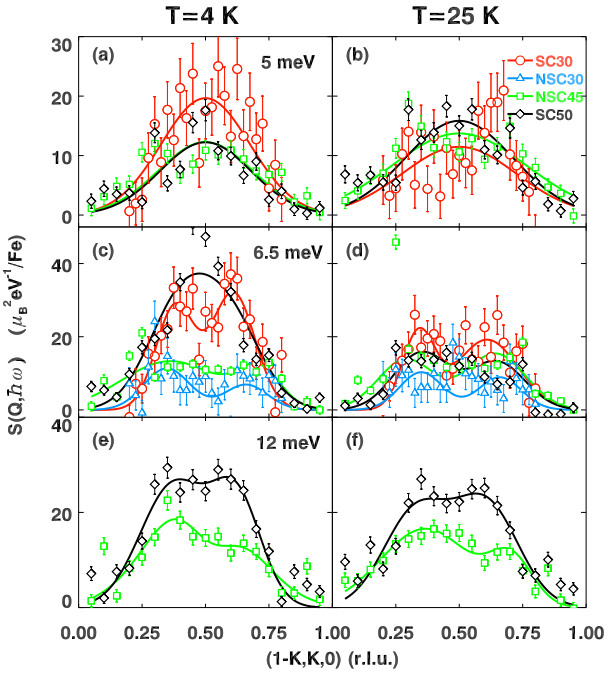

Figure 4.19: Magnetic excitations for $Fe_{1+\delta}Se_xTe_{1-x}$ measured around $(0.5, 0.5, 0)$. The left and right columns show the magnetic peak profiles for 4 K (1.5 K for SC30 and NSC30) and 25 K respectively. Constant-energy scans at $(0.5, 0.5, 0)$, taken along the transverse direction [as shown by (ii) in Fig. 4.2 (c)] at $\hbar\omega$ = (a-b) 5 meV, (c-d) 6.5 meV and (e-f) 12 meV. The solid lines are based on least square fits to the data with two Gaussian peaks and a constant background. The fitted constant background has been subtracted from all data sets. The error bars corresponds to the square root of the number of counts.

In Figs. 4.18 and 4.19, we show measurements near $(0.5, 0.5, 0)$. For SC50, a clear "resonance" is observed when comparing the energy scans performed at 4 K and 25 K [see Fig. 4.18]. In Fig. 4.19 (a) to (f), constant-energy scans at $\hbar\omega$ =5, 6.5 and 12 meV performed in the direction transverse to $\mathbf{Q} = (0.5, 0.5)$ are shown. Similar to SC50, but less pronounced, we can also see a "resonance" feature in SC30 in the scans of $\hbar\omega = 6.5$ and 5 meV.

For the non-superconducting samples, there is no temperature effect observed for data taken between 4 K and 25 K. For NSC30, we did a constant-energy scan near

$(0.5, 0.5)$ only at $\hbar\omega = 6.5$ meV, and the intensity is very low compared to either its own magnetic scattering near $(0.5, 0)$ or those from the other samples near $(0.5, 0.5)$. It is clear that the low energy spin excitations are mostly focused around $(0.5, 0)$ for NSC30. The NSC45 sample has Se doping very close to SC50, and also very similar magnetic excitation spectrum near $(0.5, 0.5)$ compared to that from the latter in its normal state ($T = 25$ K). However, with no superconducting transition, its spectrum at low temperature ($T = 4$ K) does not differ much from that at $T = 25$ K.

The implications of our results are very clear for NSC30 and SC50. For NSC30, a short-ranged static magnetic order is present at low temperature near $(0.5, 0)$, corresponding to a 3D bicollinear E-type spin structure. Its low energy magnetic excitations are also focused near $(0.5, 0)$. With the static order present, no superconductivity is achieved in this sample. For the SC50 sample, there is no static order and the low energy magnetic excitation spectrum is mostly shifted to the $(0.5, 0.5)$ region, corresponding to collinear C-type spin correlations. Similar to the situation in the "122" [21, 196] or "1111" systems, [54, 184, 191, 197–199] this collinear configuration without static order appears to favor superconductivity.

The results for NSC45 are more complicated. Here, with Se doping close to SC50, the magnetic excitations near the $(0.5, 0.5)$ point are rather similar to the superconductor, except that the "resonance" feature is missing. Apparently, having magnetic excitations near $(0.5, 0.5)$ associated with the collinear spin configuration is not sufficient for superconductivity to emerge. The presence of static 2D-like magnetic order is correlated with the suppression of superconductivity. Of course, the tetragonal crystal structure gives no energetic distinction between the ordering wave vectors $(0.5, 0)$ and $(0.5, 0.5)$, so that the magnetic configuration is relatively soft. We suggest that the greater concentration of Fe in this sample is the likely key to the magnetism at

(0.5,0). It is possible that there is a mixed phase where the two types of magnetic correlations coexist on a microscopic level, similar to that of the mixed C-E phase in manganites, [200] as suggested in Ref. [190].

The case for SC30 is, in fact, quite intriguing. A 2D-like short-range static order exists at low temperature, while low energy magnetic excitations are found both around $(0.5, 0)$ and $(0.5, 0.5)$ with comparable spectral weight. Therefore, the magnetic excitation spectrum actually looks very similar to that in NSC45, yet there is bulk superconductivity in SC30 when the static magnetic order is also present. Compared to NSC45, the ratio of spectral weight near (0.5,0.5) to that near (0.5,0) is higher in SC30, indicating a larger volume of the sample favoring collinear spin correlations. The "resonance" occurs below T_c, showing an enhancement of spectral weight only near $(0.5, 0.5)$. This indicates that superconductivity only exists in the part of the sample with dynamic collinear spin correlations. Although it is conceivable that the static order and superconductivity could coexist in the same domains as suggested by previous μSR work, [201] it is also possible to have a system with macroscopic phase separation, where the volume of local collinear or bicollinear regions are large enough to form separate domains. In this case, the features near $(0.5, 0)$ (elastic magnetic peak and low energy magnetic excitations), and those near $(0.5, 0.5)$ come from different regions. This scenario would be consistent with the (varying) susceptibility results for different small pieces taken at different locations from this sample, and agrees with results from all other samples where static magnetic order and superconductivity do not coexist locally.

Why would samples with similar Se content (*e.g.*, NSC30 vs. SC30, NSC45 vs. SC50) show dramatically different behaviors? It is clear from previous work that the Fe content has a significant impact on the magnetism. [35, 146] For example, higher

Fe content in the parent compound can drive the order from commensurate to incommensurate, [146] while its effect has been less clear for the superconducting region. It seems unlikely that the excess Fe atoms act simply as isolated magnetic moments that destroy the superconductivity, since our observations of variations in static magnetic order and low energy spin excitations cannot be explained in such a simple manner. Theoretically, it has been predicted that lowering the height of the chalcogen (Te/Se) positions can drive the "1:1" system from the bicollinear to the collinear spin configuration, [190, 202] and Fe interstitials will certainly have an impact on Fe-Te/Se-Fe bond lengths and bond angles. There are several reports concerning the effect of excess Fe on the lattice parameters [169, 170, 203]; our results indicate that the lattice parameters a and c both decrease slightly with increased Fe content (holding Se constant), which does not appear to be entirely consistent with the trends reported by others. To make further progress on this issue, it will likely be necessary to characterize the microstructure associated with specific compositions.[168, 170] For example, it has been suggested that the excess Fe atoms most likely reside around (0.25,0.25,0.7) [144] which is on the opposite side to the Fe/Se sides in respect to the Fe planes. Since these Fe atoms are not ordered in any way, diffraction measurements are not very sensitive to their positions. EXAFS or X-ray/neutron PDF (pair distribution function) measurements may be more useful in order to probe the locations of these Fe atoms and their effect on the local structures.

We have studied the relationship between superconductivity and the character of magnetic correlations in the 1:1 system. If the magnetic correlations in the system are characterized by $\mathbf{Q} = (0.5, 0)$, which generally leads to static order, superconductivity is suppressed. We find that such correlations are enhanced in samples with excess Fe. Magnetic fluctuations at $\mathbf{Q} = (0.5, 0.5)$, as found in other Fe-based superconductor

families, are necessary, but not sufficient, for the emergence of bulk superconductivity. There are cases where magnetic correlations of both types coexist and compete. Overall, our results confirm that the nature of the magnetic correlations is crtical to the occurrence of superconductivity in $Fe_{1+\delta}Se_xTe_{1-x}$.

4.3.3 Magnetic excitations in normal state

In this section, we present our work to study the magnetic excitations in normal state. In contrast to the Mott-insulating parent compounds of the cuprates, the parent compounds of the Fe-based superconductors are poor metals. This naturally leads to the suggestion of itinerant magnetism resulting from the nesting of the Fermi surface, or more generally, enhancement of non-interacting susceptibility. [160, 161, 204, 205] Disregarding the apparent failure of such itinerant picture in producing the so-called bi-collinear magnetic structure of $Fe_{1+y}Te$, [144, 146] the spin-fluctuation picture of superconductivity [160, 161, 204, 205] is qualitatively appealing, and appears to give a natural explanation for the spin resonance and spin gap . [206] Nevertheless, there are theoretical analyses that suggest that there may be a significant local-moment character to the magnetism [190, 207–210] A direct way to test the different theoretical perspectives is to evaluate the instantaneous moment from inelastic magnetic neutron scattering measurements.

We report an inelastic neutron scattering study on the temperature evolution of the low-energy magnetic excitation of an $FeTe_{1-x}Se_x$ sample with x=65%. The magnetic excitations below $T_c \sim 14$ K are almost identical to those measured previously on superconducting $FeTe_{1-x}Se_x$ samples with $x \lesssim 50\%$ [65, 147, 149, 151, 154], having a spin gap of ~ 5 meV and a resonance at ~ 7 meV, with anisotropic disper-

sion along the direction transverse to $\mathbf{Q}_0$. On heating to $T = 25$ K, the resonance disappears, with spectral weight moving into the gap, and the dispersion resembles an "hour-glass" shape like those observed in the cuprates [117, 211–213]. With further heating, the spin excitations near the saddle point (5 meV) start to split in $\mathbf{Q}$ and become clearly incommensurate, exhibiting a "waterfall" structure at 100 K and above, similar to the situation in underdoped $YBa_2Cu_3O_{6+x}$ [212]. However, the integrated spectral weight below $\hbar\omega = 12$ meV remains almost unchanged as a function of temperature, indicating a large energy scale associated with the stability of the instantaneous magnetic moment. The absolute normalization of the low-energy weight gives a lower limit (not counting the strong spectral weight at higher energies [154]) of the magnetic moment per Fe site to be $\sim 0.26\mu_B$/Fe. Such a robust and sizable moment is apparently beyond the standard consideration of spin-density-wave picture [160, 161, 204, 205], and strongly suggests that local moment magnetism is present (and likely dominant) in the Fe-based superconductors [190, 207–209].

The single-crystal sample used in the experiment was grown by a unidirectional solidification method with composition of $Fe_{0.98}Te_{0.35}Se_{0.65}$ (8.6g). The bulk susceptibility results in Fig. 4.20 (b) shown $T_c \sim 14$ K was characterized using a superconducting quantum interference device (SQUID) magnetometer. Neutron scattering experiments were carried out on the triple-axis spectrometer BT-7 located at the NIST Center for Neutron Research. We used beam collimations of open-50′-S- 50′-open (S present sample) with fixed final energy at 14.7 meV and pyrolytic graphite filters after the sample. The lattice constants for the sample are $a = b = 3.81$ Å, and $c = 6.02$ Å, using the notation where there are two Fe atoms in one unit cell. The inelastic scattering measurements have been performed in the $(HK0)$ scattering plane [Fig. 4.20 (a)]. The data are described in reciprocal lattice units (r.l.u.) of

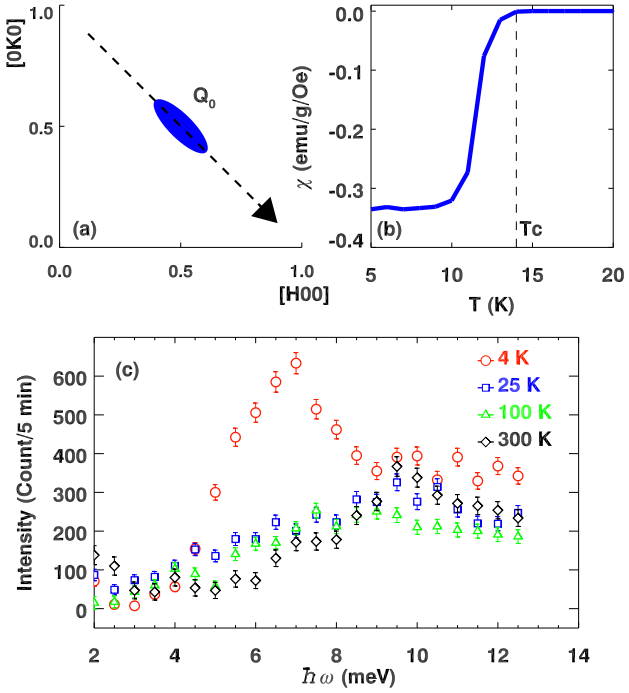

Figure 4.20: (a) The schematic diagram of the neutron scattering measurements in the $(HK0)$ zone. Dashed lines denote linear scans performed across $\mathbf{Q}_0 = (0.5, 0.5, 0)$ in the text. (b) ZFC magnetization measurements by SQUID with vertical 5 Oe. field perpendicular to the $a-b$ plane. T_c ~14K is marked by a dash line. (c) Constant Q scans at $\mathbf{Q}_0$ taken at different temperatures: 5 K (Red circle), 25 K (Blue square), 100 K (Green triangle), and 300 K (Black diamond). Fitted background obtained from constant energy scans has been subtracted from all data sets.

$(a*, b*, c*) = (2\pi/a, 2\pi/b, 2\pi/c)$. Absolute normalizations are performed based on incoherent elastic scattering measurements from the sample.

Low energy spin excitations are mainly distributed near $\mathbf{Q}_0$ in-plane wave-vector, similar to the case in the 50% Se doped sample [c][148]. In Fig. 4.20(c), we show constant-$\mathbf{Q}$ scans at $\mathbf{Q}_0$ from 4 K to 300 K. There is a clear resonance peak for data taken in the superconducting phase ($T = 4$ K, red circles). When heated above T_c,

[c]There is no elastic magnetic intensity found near $(0.5, 0, 0.5)$, which is the antiferromagnetic ordering wave vector in the parent compound, and very little spectral weight near $(0.5, 0, 0)$ at low energies and low temperature.

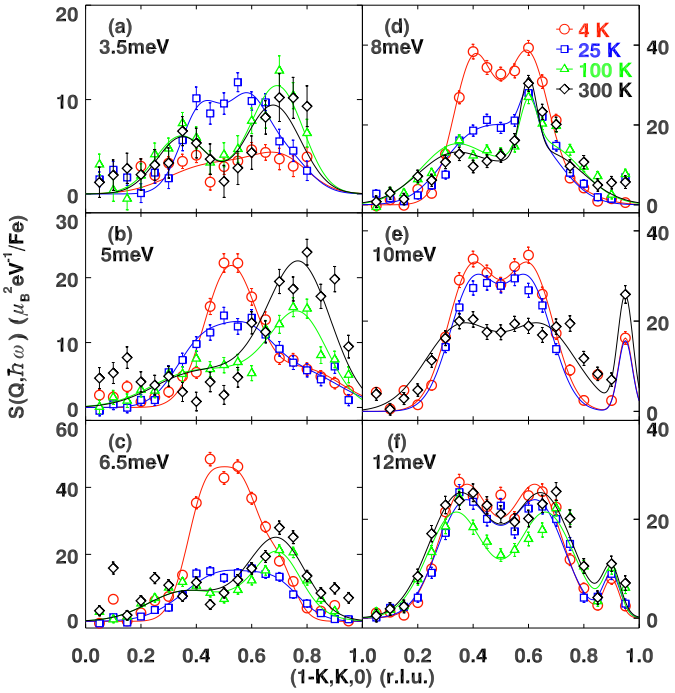

Figure 4.21: Constant energy scans at (1-k,k,0) with different temperature: 5 K (Red circle), 25 K (Blue square), 100 K (Green triangle) and 300 K (Black diamond) at different $\hbar\omega$: (a) 3.5 meV, (b) 5 meV, (c) 6.5 meV, (d) 8 meV, (e) 10 meV, and (f) 12 meV. A flat fitted background has been subtracted from all data sets. The solid lines are based on the fit described in the text. The error bars represent the square root of the number of counts.

the resonance peak disappears, and spectral weight starts to fill in the gap below $\Delta \sim 5$ meV. For the normal state, the intensity at $\mathbf{Q}_0$ appears to peak at around $\hbar\omega \sim 10$ meV. These results are in good agreement with previous neutron scattering measurements [65, 149], indicating that further Se doping above the optimal value of 50% does not significantly alter the low-energy magnetic excitations in the system.

Constant energy scans across $\mathbf{Q}_0$, performed in the transverse direction, are plotted in Fig. 4.21. One can see how the resonance disappears with heating in Fig. 4.21 (c) and (d). For $\hbar\omega \leq 6.5$ meV, Fig. 4.21 (a)-(c), we note that the peak on the right

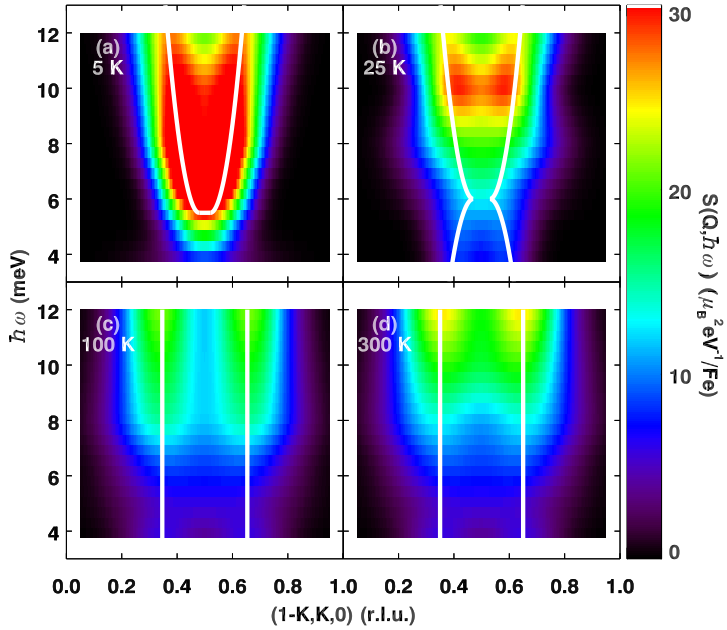

Figure 4.22: Contour intensity maps showing the fitted magnetic scattering intensity versus $\hbar\omega$ and q at different temperature: (a) 5 K, (b)25 K, (c) 100 K and (d) 300 K.

side [larger K side, near $(0.25, 0.75, 0)$] is further out in $\mathbf{Q}$, with respect to Q_0, compared to its counter-part on the left (small K) side, and becomes disproportionately strong. This behavior is inconsistent with crystal symmetry, which magnetic or simple phonon scattering must follow. The nature of this spurious peak is not entirely known. It is very likely not associated with magnetic scattering from the sample; its growth with temperature suggests that it arises from multi-scattering processes involving certain phonon modes. Fortunately, it only appears on the large K side, leaving the small K side uncontaminated. In our data analysis, we fit the magnetic signal using a double Gaussian function, with two peaks split symmetrically about $\mathbf{Q}_0$, plus a single Gaussian function for the spurious peak. The fitted magnetic intensities are presented as contour maps in Fig. 4.23. With the spurious peak removed, one can

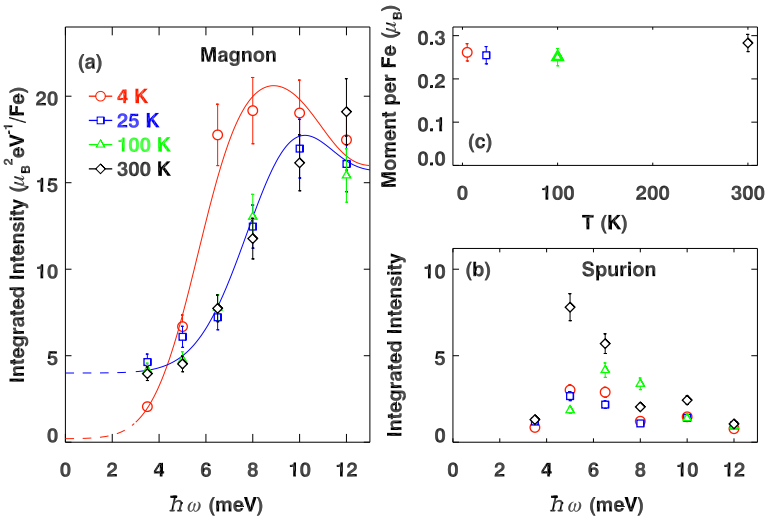

Figure 4.23: (a) Q-integrated (integrated only in one-dimension, along the transverse direction) magnetic intensity, obtained based on the fit described in the text, plotted vs. temperature. (b) Q-integrated intensity for the spurious peak around (0.25,0.75,0), plotted vs. temperature. (c) Magnetic moment per Fe site vs. temperature.

easily see the evolution of the magnetic excitation spectrum with temperature.

In the superconducting phase, Fig. 4.22(a), there is very little spectral weight below 5 meV, while the excitations disperse outwards at higher energies. As a function of temperature [Fig. 4.22(a)-(d)], the dispersion at the highest energies changes little, and one can still observe well defined magnetic excitations at $\hbar\omega = 12$ meV up to $T = 300$ K. The temperature effect on the dispersion below the resonance energy is much more pronounced. On warming from 4 K to 25 K, intensity that emerges below the gap appears to disperse outwards slightly, as shown in Fig. 4.22 (b). Our results are consistent with those in in Ref. [151], where the spectrum is narrowest in **Q** at

the saddle point around 5 meV, and becomes broader for energy transfers both above and below for $T > T_c$.

With further heating, the Q-dependence of the spectrum changes most dramatically near the saddle point. At $T = 100$ K, the lower part of the dispersion clearly moves outwards from $\mathbf{Q}_0$, as shown in Fig. 4.22(c). The saddle point at 5 meV actually disappears, and the dispersion becomes clearly incommensurate and almost vertical. There is little change between 100 K and 300 K. The change in dispersion from 4 K to 100 K is qualitatively similar to behavior reported for underdoped $YBa_2Cu_3O_{6+x}$ [212].

In Fig. 4.23 (a) and (b), we plot the intensities, integrated along $\mathbf{Q} = (1-K, K, 0)$, of the magnetic scattering and the spurious peak. The effect of the resonance in the superconducting phase is observable up to $\hbar\omega \sim 10$ meV. The plot of the spurious-peak intensity shows signs of temperature activation, and is peaked near 5 meV; in any case, its scale is generally small compared to the magnetic signal.

The magnetic response in the normal state shows little temperature dependence and the main spectral weight is always located at higher energies ($\gtrsim$ 6 meV). Compared to that in the superconducting stat, the low energy spectral weight (below the gap) does appear to increase in the normal state when "resonance" near 6.5 meV disappear, but remains almost unchanged with further heating for T up to 300 K This is consistent with the system having no static magnetic order at low temperature, and therefore no shift of spectral weight from elastic channel into those at low energy transfers upon heating. The lack of temperature dependence for the magnetic excitation spectrum in the normal state for T between 25 K and 300 K, suggest a large energy scale associated with the magnetic response. We also note that the dispersion changes from a near hour-glass shape at low temperature (T=4 K and 25 K) to a "wa-

terfall" shape at high temperature (T=100 K and 300 K). This change in dispersion is qualitatively similar to the behavior reported for underdoped $YBa_2Cu_3O_{6+x}$ [212], but occurs at temperature well within the normal state, and its origin is not entirely understood.

Our key result is obtained by integrating the magnetic signal over $\mathbf{Q}$ and $\hbar\omega$. For the $\mathbf{Q}$ integration, we assume the peak width along the longitudinal direction is same as transverse direction and that the response is uniform along L. For energy, we integrated over the interval 0 meV$\leq \hbar\omega \leq$ 12 meV, using the low-energy extrapolation indicated by the dashed lines in Fig. 4.23(a). From this integral, we obtain an instantaneous magnetic moment of 0.26(7) μ_B per Fe. The temperature dependence of this quantity is negligible, as shown in Fig. 4.23(c).

The moment we have evaluated is only a fraction of the total moment per site, considering that previous measurements have shown significant spectral weight all the way up to a few hundred meV [154]. Nevertheless, such a large low-energy magnetic response is already an order of magnitude larger than what is expected from a simple itinerant picture. For example, the density of states at the Fermi energy (E_{F}) has been calculated to be $\sim$ 1.5 ev^{-1} per Fe for FeSe [214]. If we assume that the electronic states within an energy range of 12 meV are fully spin polarized, then obtain an estimated moment of $\sim$ 0.02 μ_B. Of course, photoemission studies have reported band renormalizations in the range of 3 to 20 [215, 216], which would substantially increase the available density of states at E_{F}; however, one must also consider the cause of the renormalizations. In theory, one can include interactions that enhance the magnetic response using the random phase approximation; however, at least one attempt to do this [217] has found that the strength of the low-energy magnetic weight is strongly temperature dependent, in contrast to our experimental result.

The observed lack of temperature dependence suggests that electronic states over a large energy range contribute to the effective moment, which is consistent with having a significant local moment, as suggested by recent theoretical work [190, 207–210].

This leads to an interesting question. For the itinerant picture, the spin gap and resonance come out naturally from the pairing gap for the quasiparticles—although they are sensitive to the symmetry of the order parameter. If the magnetic moments involve states at high binding energies, then one must reconsider the evaluation of the resonance. It is clear that the magnetic correlations are sensitive to the development of pairing and superconductivity; however, the electrons involved in the pairing and in the magnetism are not necessarily identical. Similar issues have been raised in the case of cuprates [192]. These issues also raise questions concerning the nature of the pairing mechanism.

4.4 Magnetic field effect on magnetic excitations.

In this section, we present our work to study the magnetic field effect on the magnetic excitations, especially on the spin resonance in iron-based superconductor. Since the resonance in the magnetic excitations are believed closely relate to the onset of superconductivity. [148, 149, 189] While superconductivity, and hence the pairing, is sensitive to magnetic field, one would naturally expect that an external magnetic field can also impact the resonance accordingly, as seen in $YBa_2Cu_3O_{6.6}$ (Ref. [218]) and in $La_{1.82}Sr_{0.18}CuO_4$ (Ref. [219]).

We have carried out an inelastic neutron scattering study on an optimally-doped 1:1 material—a single crystal of $FeTe_{0.5}Se_{0.5}$, with $T_c \approx$14 K. We find that a resonance with energy $\hbar\Omega_0 \approx 6$ meV$= 5k_BT_c$ appears below T_c, consistent with previous find-

ings. [149, 189] In a 7-T magnetic field parallel to the a-b plane, the superconductivity is partially suppressed, with reduced T_c of 12 K. In the field, the resonance starts to appear at the reduced T_c, with lower intensity than that measured in zero field. This behavior demonstrates that the magnetic excitations have a close association with the superconductivity.

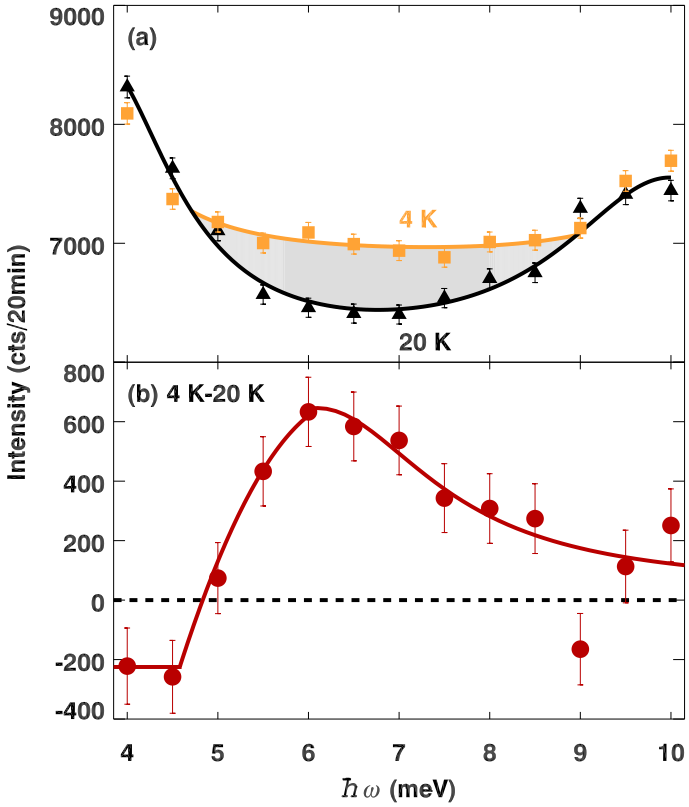

Figure 4.24: (a) Constant **Q** scans at $(0.5, 0.5, 0)$ for temperatures below ($T = 4$ K) and above ($T = 20$ K) T_c. Shading indicates the difference between scans. (b) Data obtained by subtracting 20 K data from 4 K data. Error bars represent square root of total counts. Lines through data are guides for the eye.

The single-crystal sample was grown by a unidirectional solidification method with nominal composition of $FeTe_{0.5}Se_{0.5}$. The bulk susceptibility was characterized using a superconducting quantum interference device (SQUID) magnetometer. In the

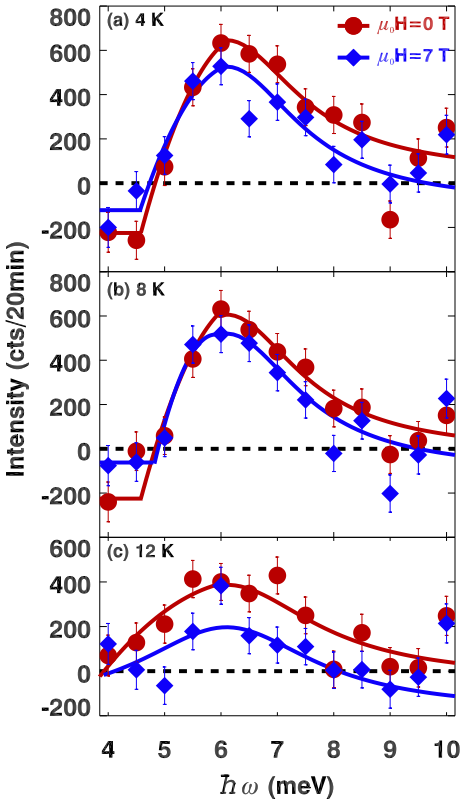

Figure 4.25: Constant **Q** scans at (0.5,0.5,0), after subtraction of the zero-filed scan at 20 K. (a) $T = 4$ K, (b) 8 K, (c) 12 K, for $\mu_0 H = 0$ T (circles), and 7 T (diamonds). Error bars represent square root of total counts. Lines through data are guides for the eye.

susceptibility measurements, the sample was oriented so that a-b plane was parallel to the magnetic field. Neutron scattering experiments were carried out on the triple-axis spectrometer BT-7 located at the NIST Center for Neutron Research. A single crystal with mass of 8.9 g was used in the neutron experiment and firmly fixed to an aluminum plate. The lattice constants are $a = b = 3.80(8)$ Å, and $c = 6.14(7)$ Å using the notation where there are two Fe atoms in one unit cell. The data were collected in (HHL) scattering plane, defined by two vectors [110] and [001], and described in reciprocal lattice units (r.l.u.) of $(a^*, b^*, c^*) = (2\pi/a, 2\pi/b, 2\pi/c)$. A vertical magnetic

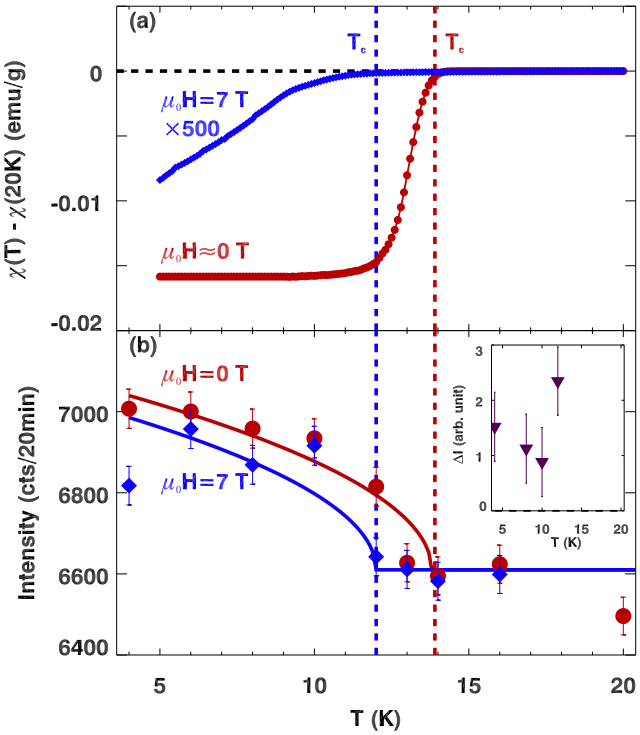

Figure 4.26: (a) Susceptibility measured with $\mu_0 H = 0.0005$ T (red circles) and 7 T (blue diamonds), with field parallel to the a-b plane. Dashed lines indicate the T_cs. (b) Resonance intensity at $(0.5, 0.5, 0)$ integrated from 6 meV to 7 meV. The solid lines are fits using mean-field theory (described in the text), with T_cs obtained from (a). Inset shows the difference of the resonance intensities for 0 T and 7 T, integrated from 5 meV to 8 meV. Error bars represent square root of total counts.

field of 7 T was applied parallel to the a-b plane (along $[1\bar{1}0]$) in the field-cooling (FC) measurements.

Energy scans have been performed at $\mathbf{Q} = (0.5, 0.5, 0)$, as shown in Fig. 4.24(a). There is a large background at low energies coming from the superconducting magnet in which the sample resides, and this obscures the magnetic response in the raw data. However, if we compare the scans taken at 4 K and 20 K, a significant amount of spectral weight shows up between 5 meV and 9 meV for the spectrum measured at low temperature (as indicated by the shading). If we subtract the 20 K data from the

4 K data as in Fig. 4.24(b), one can see a broad peak at ~ 6 meV. This is consistent with that observed in 40% and 50% Se doped samples, in which resonance energies of 6.5 meV and 7 meV, respectively, were reported. [149, 189] Although a spin gap is not directly observed in the raw data, we do see from the background subtracted data in Fig. 4.24(b) that the difference of the intensity ($I_{4K} - I_{20K}$) becomes negative below 5 meV, which suggests that a gap opens below this energy at 4 K, consistent with the gap value obtained by Qiu *et al.*. [149]

To test the impact of a magnetic field, a 7-T field was applied at 20 K, and the sample was cooled in the field. In Fig. 4.25, we show background (20 K data, zero field) subtracted scans performed at different temperatures. At $T = 12$ K, the difference between data taken with and without the field is very clear. With further cooling, the difference is still observable but becomes less pronounced. At $T = 4$ K, the peak intensity for the 7-T scan is about 10% to 20% smaller than that of the zero-field data, while the 7-T spectrum seems to have more intensity filled in below the gap (~ 5 meV). We have also performed Q-scans at the resonance energy with and without field. Due to the large background, the results are inconclusive and therefore are not shown.

There is a sum rule for scattering from spin-spin correlations, and hence one might expect that the reduction of the resonance intensity by the field should result in an increase of spectral weight below the gap, as commonly seen in cuprates, [220–223] as well as in $BaFe_{1.9}Ni_{0.1}As_2$ (Ref. [224]). As discussed above, it is consistent with our results in principle, but the large background makes it impossible to follow the behavior to lower energies. In cuprates, Demler *et al.* analyzed a model of coexisting but competing phases of superconductivity and SDW order, [106] and successfully predicted the field-induced static magnetic order observed experimentally. [93, 125,

186] We have searched for SDW order around (0.5,0.5,0), but no evidence of such field-induced order was found.

We have measured the bulk susceptibility in 0-T and 7-T field as well, and the results are shown in Fig. 4.26(a). In zero field, the system enters a superconducting state at 14 K, and becomes fully diamagnetic below 12 K. In the 7-T field, superconductivity is partially suppressed, and T_c has been reduced to 12 K. As a result of the suppressed superconductivity, the resonance intensity has also been reduced as shown in Fig. 4.25.

Fig. 4.26(b) gives another perspective of the impact of the field on the resonance. There we plot the intensity, integrated from 6 meV to 7 meV, as a function temperature obtained for the measurements with and without the field. The intensity $I(T)$ was fit with the mean-field theory [63] using T_cs determined by the onset of the diamagnetism in Fig. 4.26(a), with $I(T) = I(0)(1 - T/T_c)^{1/2} + A$, where $I(0)$, and A are constants. This formula results in the solid lines, which fit the data reasonably well. In both 0 T and 7 T, the resonance intensity starts to appear below respective T_c, and increases with cooling. At low temperatures, the intensity at 7 T is lower than the zero-field value. To confirm that the intensity is reduced at 7 T, we plot in the inset of Fig. 4.26(b) the difference between intensity at 0 T and 7 T, ΔI, integrated from 5 meV to 8 meV; one can see that the intensity difference is well above zero.

With Fig. 4.26, one can better understand the results in Fig. 4.25, especially the most pronounced field effect at 12 K. In zero field, the sample is in superconducting state at 12 K, where the resonance has finite intensity; in the 7-T field, the system is driven to normal state at this temperature, and the resonance intensity is approaching background level.

From the data, it is clear that the magnetic field depresses the superconductivity,

and also reduces the onset temperature and intensity of the resonance. In principle, if the resonance is directly associated with the superconducting volume of the sample, the intensity ratio I_{7T}/I_{0T} should be roughly proportional to $1 - H/H_{c2}$, where H is the applied field, and H_{c2} is the upper critical field. [218] Our results showing a change $\sim 10\%$ in the resonance intensity, suggesting that H_{c2} is ~ 70 T, which is comparable to the range estimated in other studies. [142, 225] Although no significant change in the resonance with field was identified for the 40% Se sample in Ref. [149], we believe that our results are consistent with that study within the error bars. The fact that the field also suppresses the resonance intensity in $BaFe_{1.9}Ni_{0.1}As_2$ [224] suggests that this should be common in Fe-based superconductors.

There are of course, still issues not fully resolved based on our results. For example, the quality of our data does not allow us to accurately determine the resonance energy. It is therefore hard to find out whether the resonance energy can be affected by the external magnetic field or not, although it has been shown that the former is the case in $BaFe_{1.9}Ni_{0.1}As_2$. [224] We have measured the susceptibility with field perpendicular to a-b plane, and compared it with the data in this work. [147] It is shown that there is only anisotropy in the superconducting state. It will be interesting to see how the resonance responds to a c-axis magnetic field. Another potentially interesting issue would be searching for the Zeeman splitting of the resonance mode under an external field, which is a good test of whether this is a singlet-triplet excitation. [150] Qiu *et al.* [149] applied a 7-T magnetic field on a 40% Se doped sample, but no splitting is visible from their results. Zhao *et al.* [224] also tried to tackle this problem using a 14.5-T field, but still the results are inconclusive—the resonance broadens in the field, but no clear split was observed, probably due to the finite resonance width and coarse energy resolution. A detailed investigation of the field effect on the low-energy

(< 10 meV) spin excitations in higher fields with improved background, and better energy resolution, will be necessary to elucidate these issues.

In summary, we observed a resonance at $\hbar\Omega_0 \approx 6$ meV in $FeTe_{0.5}Se_{0.5}$ ($T_c = 14$ K). The temperature dependence of the intensity is consistent with the scaling $1-(T/T_c)^{1/2}$. A 7 T magnetic field partially suppresses superconductivity, and lowers T_c to about 12 K, determined from the bulk susceptibility. In the field, the resonance starts to appear at the lowered T_c, 12 K, with intensity reduced. These results are consistent with the picture that the resonance is related to quasiparticle scattering in the superconducting phase, and is reduced when superconductivity becomes weaker, either by heating or applying an external magnetic field.

Bibliography

[1] H. K. Onnes, Commun. Phys. Lab. **12**, 120 (1911).

[2] B. T. Matthias, T. H. Geballe, and V. B. Compton, Rev. Mod. Phys. **35**, 1 (1963).

[3] L. R. Testardi, J. H. Wernick, and W. A. Royer, Solid State Commun. **15**, 1 (1974).

[4] J. Nagamatsu, N. Nakagawa, T. Muranaka, Y. Zenitani, and J. Akimitsu, Nature **410**, 63 (2001).

[5] J. G. Bednorz and K. A. Müller, Z. Phys. B **64**, 189 (1986).

[6] Z. X. Zhao, L. Q. Chen, C. G. Cui, Y. H. Huang, J. X. Liu, G. H. Chen, S. L. Li, S. Q. Guo, and Y. Y. He, Kexue Tongbao **32**, 522 (1987).

[7] M. K. Wu, J. R. Ashburn, C. J. Torng, P. H. Hor, R. L. Meng, L. Gao, Z. J. Huang, Y. Q. Wang, and C. W. Chu, Phys. Rev. Lett. **58**, 908 (1987).

[8] H. Maeda, Y. Tanaka, M. Fukutomi, and T. Asano, Jpn. J. Appl. Phys. **27**, L209 (1988).

[9] Z. Z. Sheng and A. M. Hermann, Nature **332**, 138 (1988).

[10] C. W. Chu, L. Gao, F. Chen, Z. J. Huang, R. L. Meng, and Y. Y. Xue, Nature **365**, 323 (1993).

[11] L. Gao, Y. Y. Xue, F. Chen, Q. Xiong, R. L. Meng, D. Ramirez, C. W. Chu, J. H. Eggert, and H. K. Mao, Phys. Rev. B **50**, 4260 (1994).

[12] Y. Kamihara, H. Hiramatsu, M. Hirano, R. Kawamura, H. Yanagi, T. Kamiya, and H. Hosono, J. Am. Chem. Soc. p. 10012 (2006).

[13] H. Takahashi, K. Igawa, K. Arii, Y. Kamihara, M. Hirano, and H. Hosono, Nature **453**, 376 (2008).

[14] F.-C. Hsu, J.-Y. Luo, K.-W. Yeh, T.-K. Chen, T.-W. Huang, P. M. Wu, Y.-C. Lee, Y.-L. Huang, Y.-Y. Chu, D.-C. Yan, et al., Proc. Natl. Acad. Sci. USA **105**, 14262 (2008).

[15] J. H. Tapp, Z. Tang, B. Lv, K. Sasmal, B. Lorenz, P. C. W. Chu, and A. M. Guloy, Phys. Rev. B **78**, 060505 (2008).

[16] M. Rotter, M. Tegel, and D. Johrendt, Phys. Rev. Lett. **101**, 107006 (2008).

[17] Z.-A. Ren, W. Lu, J. Yang, W. Yi, X.-L. Shen, C. Zheng, G.-C. Che, X.-L. Dong, L.-L. Sun, F. Zhou, et al., Chin. Phys. Lett. **25**, 2215 (2008).

[18] J. Orenstein and A. J. Millis, Science **288**, 468 (2000).

[19] J. W. Lynn and P. Dai, Physica C **469**, 469 (2009).

[20] H. Luetkens, H. H. Klauss, M. Kraken, F. J. Litterst, T. Dellmann, R. Klingeler, C. Hess, R. Khasanov, A. Amato, C. Baines, et al., Nat. Mater. **8**, 305 (2009).

[21] H. Chen, Y. Ren, Y. Qiu, W. Bao, R. H. Liu, G. Wu, T. Wu, Y. L. Xie, X. F. Wang, Q. Huang, et al., Euro. Phys. Lett. **85**, 17006 (2009).

[22] G. Dhanaraj, K. Byrappa, V. Prasad, M. Dudley, H. A. Dabkowska, and A. B. Dabkowski, *Crystal Growth of Oxides by Optical Floating Zone Technique*, Springer Handbook of Crystal Growth (Springer Berlin Heidelberg, 2010).

[23] G. Shirane, S. M. Shapiro, and J. M. Tranquada, *Neutron Scattering with a Triple-Axis Spectrometer: Basic Techniques.* (Cambridge University Press, Cambridge, 2002).

[24] J. M. Tranquada, arXiv:cond-mat/0512115 (2005).

[25] A. R. Moodenbaugh, Y. Xu, M. Suenaga, T. J. Folkerts, and R. N. Shelton, Phys. Rev. B **38**, 4596 (1988).

[26] N. Yamada and M. Ido, Physica C **203**, 240 (1992).

[27] M. Hücker, M. v. Zimmermann, G. D. Gu, Z. J. Xu, J. S. Wen, G. Xu, H. J. Kang, A. Zheludev, and J. M. Tranquada, Phys. Rev. B **83**, 104506 (2010).

[28] J. M. Tranquada, B. J. Sternlieb, J. D. Axe, Y. Nakamura, and S. Uchida, Nature **375**, 561 (1995).

[29] J. M. Tranquada, H. Woo, T. G. Perring, H. Goka, G. D. Gu, G. Xu, M. Fujita, and K. Yamada, Nature **429**, 534 (2004).

[30] J. Wen, Q. Jie, Q. Li, M. Huecker, M. v. Zimmermann, S. J. Han, Z. Xu, D. K. Singh, L. Zhang, G. Gu, et al., arXiv:1009.0031 (2010).

[31] M. Hücker, M. Zimmermann, Z. Xu, J. Wen, G. Gu, W. Tian, J. Zarestky, and J. Tranquada, Journal of Superconductivity and Novel Magnetism **24**, 1229 (2010).

[32] Y. Mizuguchi, F. Tomioka, S. Tsuda, T. Yamaguchi, and Y. Takano, J. Phys. Soc. Jpn. **78**, 074712 (2009).

[33] U. Patel, J. Hua, S. H. Yu, S. Avci, Z. L. Xiao, H. Claus, J. Schlueter, V. V. Vlasko-Vlasov, U. Welp, and W. K. Kwok, Appl. Phys. Lett. **94**, 082508 (2009).

[34] N. Katayama, S. Ji, D. Louca, S.-H. Lee, M. Fujita, T. J. Sato, J. S. Wen, Z. J. Xu, G. D. Gu, G. Xu, et al., arXiv:1003.4525v1 (2010).

[35] J. Wen, G. Xu, Z. Xu, Z. W. Lin, Q. Li, W. Ratcliff, G. Gu, and J. M. Tranquada, Phys. Rev. B **80**, 104506 (2009).

[36] *The nobel prize in physics 1913* (Nobel Foundation.).

[37] W. Meissner and R. Ochsenfeld, Naturwissenschaften **21**, 787 (1933).

[38] *The nobel prize in physics 1987* (Nobel Foundation.).

[39] E. Itskevich and I. Morozov, JETP Letters **78**, 72 (2003).

[40] K. Ishida, Y. Nakai, and H. Hosono, J. Phys. Soc. Jpn. **78**, 062001 (2009).

[41] X. H. Chen, T. Wu, G. Wu, R. H. Liu, H. Chen, and D. F. Fang, Nature **453**, 761 (2008).

[42] G. Wu, Y. L. Xie, H. Chen, M. Zhong, R. H. Liu, B. C. Shi, Q. J. Li, X. F. Wang, T. Wu, Y. J. Yan, et al., Journal of Physics: Condensed Matter **21**, 142203 (2009).

[43] A. S. Sefat, R. Jin, M. A. McGuire, B. C. Sales, D. J. Singh, and D. Mandrus, Phys. Rev. Lett. **101**, 117004 (2008).

[44] P. M. Shirage, K. Miyazawa, H. Kito, H. Eisaki, and A. Iyo, Applied Physics Express **1**, 081702 (2008).

[45] G. F. Chen, Z. Li, G. Li, W. Z. Hu, J. Dong, X. D. Zhang, P. Zheng, N. L. Wang, and J. L. Luo, Chin. Phys. Lett. **25**, 3403 (2008).

[46] X. C. Wang, Q. Q. Liu, Y. X. Lv, W. B. Gao, L. X. Yang, R. C. Yu, F. Y. Li, and C. Q. Jin, Solid State Commun. **148**, 538 (2008).

[47] M. J. Pitcher, D. R. Parker, P. Adamson, S. J. C. Herkelrath, A. T. Boothroyd, and S. J. Clarke, Chem. Commun. **45**, 5918 (2008).

[48] C. W. Chu, F. Chen, M. Gooch, A. M. Guloy, B. Lorenz, B. Lv, K. Sasmal, Z. J. Tang, J. H. Tapp, and Y. Y. Xue, Physica C **469**, 326 (2009).

[49] S. J. Zhang, X. C. Wang, Q. Q. Liu, Y. X. Lv, X. H. Yu, Z. J. Lin, Y. S. Zhao, L. Wang, Y. Ding, H. K. Mao, et al., Euro. Phys. Lett. **88**, 47008 (2009).

[50] B. C. Sales, A. S. Sefat, M. A. McGuire, R. Y. Jin, D. Mandrus, and Y. Mozharivskyj, Phys. Rev. B **79**, 094521 (2009).

[51] K.-W. Yeh, T.-W. Huang, Y.-l. Huang, T.-K. Chen, F.-C. Hsu, P. M. Wu, Y.-C. Lee, Y.-Y. Chu, C.-L. Chen, J.-Y. Luo, et al., Euro. Phys. Lett. **84**, 37002 (2008).

[52] Y. Mizuguchi, F. Tomioka, S. Tsuda, T. Yamaguchi, and Y. Takano, Appl. Phys. Lett. **93**, 152505 (2008).

[53] S. Medvedev, T. M. McQueen, I. Trojan, T. Palasyuk, M. I. Eremets, R. J. Cava, S. Naghavi, F. Casper, V. Ksenofontov, G. Wortmann, et al., Nat. Mater. **8**, 630 (2009).

[54] J. Zhao, Q. Huang, C. de la Cruz, J. W. Lynn, M. D. Lumsden, Z. A. Ren, J. Yang, X. Shen, X. Dong, Z. Zhao, et al., Phys. Rev. B **78**, 132504 (2008).

[55] B. I. Zimmer, W. Jeitschko, J. H. Albering, R. Glaum, and M. Reehuis, **229**, 238 (1995).

[56] R. Pottgen and D. Johrendt, **63**, 1135 (2008).

[57] N. Kumar, S. Chi, Y. Chen, K. G. Rana, A. K. Nigam, A. Thamizhavel, W. Ratcliff, II, S. K. Dhar, and J. W. Lynn, Phys. Rev. B **80**, 144524 (2009).

[58] P. C. Lauterbur, Nature **242**, 190 (1973).

[59] I. I. Rabi, J. R. Zacharias, S. Millman, and P. Kusch, Phys. Rev. **53**, 318 (1938).

[60] J. Bardeen, L. N. Cooper, and J. R. Schrieffer, Phys. Rev. **108**, 1175 (1957).

[61] *The nobel prize in physics 1972* (Nobel Foundation.).

[62] N. F. Mott and R. Peierls, Proc. Phys. Soc. London **49**, 72 (1937).

[63] C. Kittel, *Introduction to Solid State Physics* (Wiley, 2004).

[64] K. Binder and A. P. Young, Rev. Mod. Phys. **58**, 801 (1986).

[65] S. H. Lee, G. Xu, W. Ku, J. S. Wen, C. C. Lee, N. Katayama, Z. J. Xu, S. Ji, Z. W. Lin, G. D. Gu, et al., Phys. Rev. B **81**, 220502 (2010).

[66] T. Adachi, T. Noji, and Y. Koike, Phys. Rev. B **64**, 144524 (2001).

[67] G. D. Gu, K. Takamuku, N. Koshizuka, and S. Tanaka, J. Crystal Growth **130**, 325 (1993).

[68] G. D. Gu, T. Egi, N. Koshizuka, P. A. Miles, G. J. Russell, and S. J. Kennedy, Physica C **263**, 180 (1996).

[69] J. S. Wen, Z. J. Xu, G. Y. Xu, M. Hücker, J. M. Tranquada, and G. D. Gu, J. Crystal Growth **310**, 1401 (2008).

[70] D. E. Thomas, Journal of Scientific Instruments **16**, 222 (1939).

[71] G. L. Squires, *Introduction to the Theory of Thermal Neutron Scattering* (Dover, Mineola, NY, 1996).

[72] R. Pynn, *Neutron Scattering: A Primer* (Los Alamos Science, 1990).

[73] Y. Koike, S. Takeuchi, H. Sato, Y. Hama, M. Kato, Y. Ono, and S. Katano, J. Low. Temp. Phys. **105**, 317 (1996).

[74] Y. Koike, A. Kobayashi, T. Kawaguchi, M. Kato, T. Noji, Y. Ono, T. Hikita, and Y. Saito, Solid State Commun. **82**, 889 (1992).

[75] N. Kakinuma, Y. Ono, and Y. Koike, Phys. Rev. B **59**, 1491 (1999).

[76] M. Akoshima and Y. Koike, J. Phys. Soc. Jpn. **67**, 3653 (1998).

[77] J. M. Tranquada, J. D. Axe, N. Ichikawa, A. R. Moodenbaugh, Y. Nakamura, and S. Uchida, Phys. Rev. Lett. **78**, 338 (1997).

[78] D. Vaknin, S. K. Sinha, D. E. Moncton, D. C. Johnston, J. M. Newsam, C. R. Safinya, and H. E. King, Phys. Rev. Lett. **58**, 2802 (1987).

[79] R. Coldea, S. M. Hayden, G. Aeppli, T. G. Perring, C. D. Frost, T. E. Mason, S. W. Cheong, and Z. Fisk, Phys. Rev. Lett. **86**, 5377 (2001).

[80] M. Fujita, H. Goka, K. Yamada, J. M. Tranquada, and L. P. Regnault, Phys. Rev. B **70**, 104517 (2004).

[81] M. v. Zimmermann, A. Vigliante, T. Niemller, N. Ichikawa, T. Frello, J. Madsen, P. Wochner, S. Uchida, N. H. Andersen, J. M. Tranquada, et al., Europhys. Lett. **41**, 629 (1998).

[82] T. Niemoeller, N. Ichikawa, T. Frello, H. Huennefeld, N. H. Andersen, S. Uchida, J. R. Schneider, and J. M. Tranquada, Eur. Phys. J. B **12**, 509 (1999).

[83] N. Ichikawa, S. Uchida, J. M. Tranquada, Niem, ouml, T. ller, P. M. Gehring, S. H. Lee, and J. R. Schneider, Phys. Rev. Lett. **85**, 1738 (2000).

[84] J. Kim, A. Kagedan, G. D. Gu, C. S. Nelson, and Y.-J. Kim, Phys. Rev. B **77**, 180513 (2008).

[85] P. Abbamonte, A. Rusydi, S. Smadici, G. D. Gu, G. A. Sawatzky, and D. L. Feng, Nat. Phys. **1**, 155 (2005).

[86] M. Fujita, H. Goka, K. Yamada, and M. Matsuda, Phys. Rev. B **66**, 184503 (2002).

[87] H. Kimura, H. Goka, M. Fujita, Y. Noda, K. Yamada, and N. Ikeda, Phys. Rev. B **67**, 140503 (2003).

[88] M. Hucker, G. D. Gu, J. M. Tranquada, M. v. Zimmermann, H. H. Klauss, N. J. Curro, M. Braden, and B. Buchner, Physica C **460-462**, 170 (2007).

[89] J. Fink, E. Schierle, E. Weschke, J. Geck, D. Hawthorn, V. Soltwisch, H. Wadati, H.-H. Wu, H. A. Durr, N. Wizent, et al., Phys. Rev. B **79**, 100502 (2009).

[90] H. A. Mook, P. Dai, S. M. Hayden, G. Aeppli, T. G. Perring, and F. Dogan, Nature **395**, 580 (1998).

[91] P. Dai, H. A. Mook, and F. Dougan, Phys. Rev. Lett. **80**, 1738 (1998).

[92] P. Dai, H. A. Mook, R. D. Hunt, and F. Dougan, Phys. Rev. B **63**, 054525 (2001).

[93] D. Haug, V. Hinkov, A. Suchaneck, D. S. Inosov, N. B. Christensen, C. Niedermayer, P. Bourges, Y. Sidis, J. T. Park, A. Ivanov, et al., Phys. Rev. Lett. **103**, 017001 (2009).

[94] H. A. Mook, P. Dai, and F. Dogbrevean, Phys. Rev. Lett. **88**, 097004 (2002).

[95] C. Stock, W. J. L. Buyers, Z. Tun, R. Liang, D. Peets, D. Bonn, W. N. Hardy, and L. Taillefer, Phys. Rev. B **66**, 024505 (2002).

[96] C. Stock, W. J. L. Buyers, R. Liang, D. Peets, Z. Tun, D. Bonn, W. N. Hardy, and R. J. Birgeneau, Phys. Rev. B **69**, 014502 (2004).

[97] C. Howald, H. Eisaki, N. Kaneko, M. Greven, and A. Kapitulnik, Phys. Rev. B **67**, 014533 (2003).

[98] J. E. Hoffman, E. W. Hudson, K. M. Lang, V. Madhavan, H. Eisaki, S. Uchida, and J. C. Davis, Science **295**, 466 (2002).

[99] V. J. Emery and S. A. Kivelson, Nature **374**, 434 (1995).

[100] J. M. Tranquada, J. D. Axe, N. Ichikawa, Y. Nakamura, S. Uchida, and B. Nachumi, Phys. Rev. B **54**, 7489 (1996).

[101] Q. Li, uuml, M. cker, G. D. Gu, A. M. Tsvelik, and J. M. Tranquada, Phys. Rev. Lett. **99**, 067001 (2007).

[102] K. Yamada, C. H. Lee, K. Kurahashi, J. Wada, S. Wakimoto, S. Ueki, H. Kimura, Y. Endoh, S. Hosoya, G. Shirane, et al., Phys. Rev. B **57**, 6165 (1998).

[103] A. V. Balatsky and P. Bourges, Phys. Rev. Lett. **82**, 5337 (1999).

[104] V. J. Emery, S. A. Kivelson, and O. Zachar, Phys. Rev. B **56**, 6120 (1997).

[105] M. K. Crawford, R. L. Harlow, E. M. McCarron, W. E. Farneth, J. D. Axe, H. Chou, and Q. Huang, Phys. Rev. B **44**, 7749 (1991).

[106] E. Demler, S. Sachdev, and Y. Zhang, Phys. Rev. Lett. **87**, 067202 (2001).

[107] E. G. Moon and S. Sachdev, Phys. Rev. B **80**, 035117 (2009).

[108] M. Hücker, M. v. Zimmermann, M. Debessai, J. S. Schilling, J. M. Tranquada, and G. D. Gu, Phys. Rev. Lett. **104**, 057004 (2010).

[109] J. M. Tranquada, N. Ichikawa, K. Kakurai, and S. Uchida, Journal of Physics and Chemistry of Solids **60**, 1019 (1999).

[110] J. M. Tranquada, G. D. Gu, uuml, M. cker, Q. Jie, H. J. Kang, R. Klingeler, Q. Li, N. Tristan, J. S. Wen, et al., Phys. Rev. B **78**, 174529 (2008).

[111] A. T. Savici, A. Fukaya, I. M. Gat-Malureanu, T. Ito, P. L. Russo, Y. J. Uemura, C. R. Wiebe, P. P. Kyriakou, G. J. MacDougall, M. T. Rovers, et al., Phys. Rev. Lett. **95**, 157001 (2005).

[112] M. Hücker, G. D. Gu, and J. M. Tranquada, Phys. Rev. B **78**, 214507 (2008).

[113] J. M. Tranquada, H. Woo, T. G. Perring, H. Goka, G. D. Gu, G. Xu, M. Fujita, and K. Yamada, Journal of Physics and Chemistry of Solids **67**, 511 (2006).

[114] E. Arrigoni, E. Fradkin, and S. A. Kivelson, Phys. Rev. B **69**, 214519 (2004).

[115] J. A. Rodriguez and et al., Measurement Science and Technology **19**, 034023 (2008).

[116] C.-H. Lee, K. Yamada, Y. Endoh, G. Shirane, R. J. Birgeneau, M. A. Kastner, M. Greven, and Y. J. Kim, J. Phys. Soc. Jpn. **69**, 1170 (2000).

[117] B. Vignolle, S. M. Hayden, D. F. McMorrow, H. M. Ronnow, B. Lake, C. D. Frost, and T. G. Perring, Nat. Phys. **3**, 163 (2007).

[118] N. B. Christensen, D. F. McMorrow, oslash, H. M. nnow, B. Lake, S. M. Hayden, G. Aeppli, T. G. Perring, M. Mangkorntong, M. Nohara, et al., Phys. Rev. Lett. **93**, 147002 (2004).

[119] M. Matsuda, M. Fujita, S. Wakimoto, J. A. Fernandez-Baca, J. M. Tranquada, and K. Yamada, Phys. Rev. Lett. **101**, 197001 (2008).

[120] O. J. Lipscombe, B. Vignolle, T. G. Perring, C. D. Frost, and S. M. Hayden, Phys. Rev. Lett. **102**, 167002 (2009).

[121] J. Chang, A. P. Schnyder, R. Gilardi, oslash, H. M. nnow, S. Pailhes, N. B. Christensen, C. Niedermayer, D. F. McMorrow, A. Hiess, et al., Phys. Rev. Lett. **98**, 077004 (2007).

[122] G. Schmid and M. Troyer, Phys. Rev. Lett. **93**, 067003 (2004).

[123] T. Momoi, Phys. Rev. B **67**, 014529 (2003).

[124] S. A. Kivelson, I. P. Bindloss, E. Fradkin, V. Oganesyan, J. M. Tranquada, A. Kapitulnik, and C. Howald, Rev. Mod. Phys. **75**, 1201 (2003).

[125] B. Lake, H. M. Ronnow, N. B. Christensen, G. Aeppli, K. Lefmann, D. F. McMorrow, P. Vorderwisch, P. Smeibidl, N. Mangkorntong, T. Sasagawa, et al., Nature **415**, 299 (2002).

[126] S. Katano, M. Sato, K. Yamada, T. Suzuki, and T. Fukase, Phys. Rev. B **62**, R14677 (2000).

[127] J. Chang, C. Niedermayer, R. Gilardi, N. B. Christensen, oslash, H. M. nnow, D. F. McMorrow, M. Ay, J. Stahn, O. Sobolev, et al., Phys. Rev. B **78**, 104525 (2008).

[128] B. Khaykovich, Y. S. Lee, R. W. Erwin, S. H. Lee, S. Wakimoto, K. J. Thomas, M. A. Kastner, and R. J. Birgeneau, Phys. Rev. B **66**, 014528 (2002).

[129] B. Khaykovich, R. J. Birgeneau, F. C. Chou, R. W. Erwin, M. A. Kastner, S. H. Lee, Y. S. Lee, P. Smeibidl, P. Vorderwisch, and S. Wakimoto, Phys. Rev. B **67**, 054501 (2003).

[130] A. A. Schafgans, A. D. LaForge, S. V. Dordevic, M. M. Qazilbash, W. J. Padilla, K. S. Burch, Z. Q. Li, S. Komiya, Y. Ando, and D. N. Basov, Phys. Rev. Lett. **104**, 157002 (2010).

[131] T. Sasagawa, Y. Togawa, J. Shimoyama, A. Kapitulnik, K. Kitazawa, and K. Kishio, Phys. Rev. B **61**, 1610 (2000).

[132] A. E. Koshelev, L. I. Glazman, and A. I. Larkin, Phys. Rev. B **53**, 2786 (1996).

[133] V. Oganesyan, D. A. Huse, and S. L. Sondhi, Phys. Rev. B **73**, 094503 (2006).

[134] D. S. Fisher, M. P. A. Fisher, and D. A. Huse, Phys. Rev. B **43**, 130 (1991).

[135] S. Tajima, T. Noda, H. Eisaki, and S. Uchida, Phys. Rev. Lett. **86**, 500 (2001).

[136] A. Himeda, T. Kato, and M. Ogata, Phys. Rev. Lett. **88**, 117001 (2002).

[137] B. Erez, New J. Phys. **11**, 115004 (2009).

[138] K. Hirota, K. Yamada, I. Tanaka, and H. Kojima, Physica B **241-243**, 817 (1997).

[139] S. Wakimoto, R. J. Birgeneau, A. Kagedan, H. Kim, I. Swainson, K. Yamada, and H. Zhang, Phys. Rev. B **72**, 064521 (2005).

[140] S. A. Kivelson, E. Fradkin, and V. J. Emery, Nature **393**, 550 (1998).

[141] M. Hücker, V. Kataev, J. Pommer, J. Harrab, A. Hosni, C. Pflitsch, and B. Buchner, Phys. Rev. B **59**, 725R (1999).

[142] W. Si, Z.-W. Lin, Q. Jie, W.-G. Yin, J. Zhou, G. Gu, P. D. Johnson, and Q. Li, Appl. Phys. Lett. **95**, 052504 (2009).

[143] K. W. Yeh, C. T. Ke, T. W. Huang, T. K. Chen, Y. L. Huang, P. M. Wu, and M. K. Wu, Cryst. Growth Des. **9**, 4847 (2009).

[144] S. Li, C. de la Cruz, Q. Huang, Y. Chen, J. W. Lynn, J. Hu, Y.-L. Huang, F.-C. Hsu, K.-W. Yeh, M.-K. Wu, et al., Phys. Rev. B **79**, 054503 (2009).

[145] M. H. Fang, H. M. Pham, B. Qian, T. J. Liu, E. K. Vehstedt, Y. Liu, L. Spinu, and Z. Q. Mao, Phys. Rev. B **78**, 224503 (2008).

[146] W. Bao, Y. Qiu, Q. Huang, M. A. Green, P. Zajdel, M. R. Fitzsimmons, M. Zhernenkov, S. Chang, M. Fang, B. Qian, et al., Phys. Rev. Lett. **102**, 247001 (2009).

[147] J. Wen, G. Xu, Z. Xu, Z. W. Lin, Q. Li, Y. Chen, S. Chi, G. Gu, and J. M. Tranquada, Phys. Rev. B **81**, 100513(R) (2010).

[148] Z. Xu, J. Wen, G. Xu, Q. Jie, Z. Lin, Q. Li, S. Chi, D. K. Singh, G. Gu, and J. M. Tranquada, Phys. Rev. B **82**, 104525 (2010).

[149] Y. Qiu, W. Bao, Y. Zhao, C. Broholm, V. Stanev, Z. Tesanovic, Y. C. Gasparovic, S. Chang, J. Hu, B. Qian, et al., Phys. Rev. Lett. **103**, 067008 (2009).

[150] W. Bao, A. T. Savici, G. E. Granroth, C. Broholm, K. Habicht, Y. Qiu, J. Hu, T. Liu, and Z. Mao, arXiv:1002.1617v1 (2010).

[151] S. Li, C. Zhang, M. Wang, H.-q. Luo, X. Lu, E. Faulhaber, A. Schneidewind, P. Link, J. Hu, T. Xiang, et al., Phys. Rev. Lett. **105**, 157002 (2010).

[152] Z. Xu, J. Wen, G. Xu, S. Chi, W. Ku, G. Gu, and J. M. Tranquada, arXiv:1012.2300 (2010).

[153] Y. Liu and et al., Superconductor Science and Technology **24**, 035012 (2010).

[154] M. D. Lumsden, A. D. Christianson, E. A. Goremychkin, S. E. Nagler, H. A. Mook, M. B. Stone, D. L. Abernathy, T. Guidi, G. J. MacDougall, C. de la Cruz, et al., Nat. Phys. **6**, 182 (2010).

[155] A. D. Christianson, E. A. Goremychkin, R. Osborn, S. Rosenkranz, M. D. Lumsden, C. D. Malliakas, I. S. Todorov, H. Claus, D. Y. Chung, M. G. Kanatzidis, et al., Nature **456**, 930 (2008).

[156] M. D. Lumsden, A. D. Christianson, D. Parshall, M. B. Stone, S. E. Nagler, G. J. MacDougall, H. A. Mook, K. Lokshin, T. Egami, D. L. Abernathy, et al., Phys. Rev. Lett. **102**, 107005 (2009).

[157] S. Chi, A. Schneidewind, J. Zhao, L. W. Harriger, L. Li, Y. Luo, G. Cao, Z. A. Xu, M. Loewenhaupt, J. Hu, et al., Phys. Rev. Lett. **102**, 107006 (2009).

[158] S. Li, Y. Chen, S. Chang, J. W. Lynn, L. Li, Y. Luo, G. Cao, Z. Xu, and P. Dai, Phys. Rev. B **79**, 174527 (2009).

[159] D. S. Inosov, J. T. Park, P. Bourges, D. L. Sun, Y. Sidis, A. Schneidewind, K. Hradil, D. Haug, C. T. Lin, B. Keimer, et al., Nat. Phys. **6**, 178 (2010).

[160] I. I. Mazin, D. J. Singh, M. D. Johannes, and M. H. Du, Phys. Rev. Lett. **101**, 057003 (2008).

[161] K. Kuroki, S. Onari, R. Arita, H. Usui, Y. Tanaka, H. Kontani, and H. Aoki, Phys. Rev. Lett. **101**, 087004 (2008).

[162] F. Ma, W. Ji, J. Hu, Z.-Y. Lu, and T. Xiang, Phys. Rev. Lett. **102**, 177003 (2009).

[163] J. Dong, H. J. Zhang, G. Xu, Z. Li, G. Li, W. Z. Hu, D. Wu, G. F. Chen, X. Dai, J. L. Luo, et al., Europhys. Lett. **83**, 27006 (2008).

[164] V. Cvetkovic and Z. Tesanovic, Europhys. Lett. **85**, 37002 (2009).

[165] S. Graser, T. A. Maier, P. J. Hirschfeld, and D. J. Scalapino, New J. Phys. **11**, 025016 (2009).

[166] M. Rotter, M. Pangerl, M. Tegel, and D. Johrendt, Angew. Chem. Int.. Ed. **47**, 7949 (2008).

[167] J.-H. Chu, J. G. Analytis, C. Kucharczyk, and I. R. Fisher, Phys. Rev. B **79**, 014506 (2009).

[168] R. Hu, E. S. Bozin, J. B. Warren, and C. Petrovic, Phys. Rev. B **80**, 214514 (2009).

[169] T. M. McQueen, Q. Huang, V. Ksenofontov, C. Felser, Q. Xu, H. Zandbergen, Y. S. Hor, J. Allred, A. J. Williams, D. Qu, et al., Phys. Rev. B **79**, 014522 (2009).

[170] T. M. McQueen, A. J. Williams, P. W. Stephens, J. Tao, Y. Zhu, V. Ksenofontov, F. Casper, C. Felser, and R. J. Cava, Phys. Rev. Lett. **103**, 057002 (2009).

[171] X. F. Wang, T. Wu, G. Wu, H. Chen, Y. L. Xie, J. J. Ying, Y. J. Yan, R. H. Liu, and X. H. Chen, Phys. Rev. Lett. **102**, 117005 (2009).

[172] R. Klingeler, N. Leps, I. Hellmann, A. Popa, U. Stockert, C. Hess, V. Kataev, H. J. Grafe, F. Hammerath, G. Lang, et al., Phys. Rev. B **81**, 024506 (2010).

[173] L. Zhang, D. J. Singh, and M. H. Du, Phys. Rev. B **79**, 012506 (2009).

[174] A. Subedi, L. Zhang, D. J. Singh, and M. H. Du, Phys. Rev. B **78**, 134514 (2008).

[175] I. I. Mazin, Nature **464**, 183 (2010).

[176] Z. Tesanovic, Physics **2**, 60 (2009).

[177] A. V. B. a. D. Parker, Physics **2**, 59 (2009).

[178] D. N. Argyriou, A. Hiess, A. Akbari, I. Eremin, M. M. Korshunov, J. Hu, B. Qian, Z. Mao, Y. Qiu, C. Broholm, et al., Phys. Rev. B **81**, 220503 (2010).

[179] T. Hanaguri, S. Niitaka, K. Kuroki, and H. Takagi, Science **328**, 474 (2010).

[180] S. H. Lee, C. Broholm, W. Ratcliff, G. Gasparovic, Q. Huang, T. H. Kim, and S. W. Cheong, Nature **418**, 856 (2002).

[181] A. Martinelli, A. Palenzona, M. Tropeano, C. Ferdeghini, M. Putti, M. R. Cimberle, T. D. Nguyen, M. Affronte, and C. Ritter, Phys. Rev. B **81**, 094115 (2010).

[182] C. Fang, B. A. Bernevig, and J. Hu, Euro. Phys. Lett. **86**, 67005 (2009).

[183] A. Guinier (Dover, New York, 1994).

[184] J. Zhao, Q. Huang, C. de la Cruz, S. Li, J. W. Lynn, Y. Chen, M. A. Green, G. F. Chen, G. Li, Z. Li, et al., Nat. Mater. **7**, 953 (2008).

[185] A. J. Drew, C. Niedermayer, P. J. Baker, F. L. Pratt, S. J. Blundell, T. Lancaster, R. H. Liu, G. Wu, X. H. Chen, I. Watanabe, et al., Nat. Mater. **8**, 310 (2009).

[186] B. Lake, K. Lefmann, N. B. Christensen, G. Aeppli, D. F. Mcmorrow, H. M. Ronnow, P. Vorderwisch, P. Smeibidl, N. Mangkorntong, T. Sasagawa, et al., Nat. Mater. **4**, 658 (2005).

[187] L. Zhang, D. J. Singh, and M. H. Du, Phys. Rev. B **79**, 012506 (2009).

[188] T. J. Liu, X. Ke, B. Qian, J. Hu, D. Fobes, E. K. Vehstedt, H. Pham, J. H. Yang, M. H. Fang, L. Spinu, et al., Phys. Rev. B **80**, 174509 (2009).

[189] H. A. Mook, M. Lumsden, A. Christianson, B. C. Sales, R. Jin, M. A. McGuire, A. Sefat, D. Mandrus, S. Nagler, T. Egami, et al., arXiv:0904.2178v1 (2009).

[190] W.-G. Yin, C.-C. Lee, and W. Ku, Phys. Rev. Lett. **105**, 107004 (2010).

[191] C. de la Cruz, Q. Huang, J. W. Lynn, J. Li, W. R. Ii, J. L. Zarestky, H. A. Mook, G. F. Chen, J. L. Luo, N. L. Wang, et al., Nature **453**, 899 (2008).

[192] G. Xu, G. D. Gu, M. Hucker, B. Fauque, T. G. Perring, L. P. Regnault, and J. M. Tranquada, Nat. Phys. **5**, 642 (2009).

[193] H. F. Fong, B. Keimer, D. L. Milius, and I. A. Aksay, Phys. Rev. Lett. **78**, 713 (1997).

[194] H. F. Fong, P. Bourges, Y. Sidis, L. P. Regnault, A. Ivanov, G. D. Gu, N. Koshizuka, and B. Keimer, Nature **398**, 588 (1999).

[195] P. Dai, M. Yethiraj, H. A. Mook, T. B. Lindemer, and F. Doan, Phys. Rev. Lett. **77**, 5425 (1996).

[196] J. Zhao, D. T. Adroja, D.-X. Yao, R. Bewley, S. Li, X. F. Wang, G. Wu, X. H. Chen, J. Hu, and P. Dai, Nat. Phys. **5**, 555 (2009).

[197] Q. Huang, J. Zhao, J. W. Lynn, G. F. Chen, J. L. Luo, N. L. Wang, and P. Dai, Phys. Rev. B **78**, 054529 (2008).

[198] C.-H. Lee, A. Iyo, H. Eisaki, H. Kito, M. T. Fernandez-Diaz, T. Ito, K. Kihou, H. Matsuhata, M. Braden, and K. Yamada, J. Phys. Soc. Jpn. **77**, 083704 (2008).

[199] Y. Qiu, M. Kofu, W. Bao, S. H. Lee, Q. Huang, T. Yildirim, J. R. D. Copley, J. W. Lynn, T. Wu, G. Wu, et al., Phys. Rev. B **78**, 052508 (2008).

[200] T. Hotta, M. Moraghebi, A. Feiguin, A. Moreo, S. Yunoki, and E. Dagotto, Phys. Rev. Lett. **90**, 247203 (2003).

[201] R. Khasanov, M. Bendele, A. Amato, P. Babkevich, A. T. Boothroyd, A. Cervellino, K. Conder, S. N. Gvasaliya, H. Keller, H. H. Klauss, et al., Phys. Rev. B **80**, 140511(R) (2009).

[202] C.-Y. Moon and H. J. Choi, Phys. Rev. Lett. **104**, 057003 (2010).

[203] R. Viennois, E. Giannini, D. van der Marel, and R. Cern, J Solid State Chem. **183**, 769 (2010).

[204] M. Daghofer, A. Moreo, J. A. Riera, E. Arrigoni, D. J. Scalapino, and E. Dagotto, Phys. Rev. Lett. **101**, 237004 (2008).

[205] J. Knolle, I. Eremin, A. V. Chubukov, and R. Moessner, Phys. Rev. B **81**, 140506 (2010).

[206] T. A. Maier, S. Graser, D. J. Scalapino, and P. Hirschfeld, Phys. Rev. B **79**, 134520 (2009).

[207] I. I. Mazin and M. D. Johannes, Nat. Phys. **5**, 141 (2009).

[208] K. Su-Peng and et al., Euro. Phys. Lett. **88**, 17010 (2009).

[209] L. de Medici, S. Hassan, and M. Capone, Journal of Superconductivity and Novel Magnetism **22**, 535 (2009).

[210] R. Arita and H. Ikeda, J. Phys. Soc. Jpn. **78**, 113707 (2009).

[211] S. M. Hayden, H. A. Mook, P. Dai, T. G. Perring, and F. Dogan, Nature **429**, 531 (2004).

[212] V. Hinkov, P. Bourges, S. Pailhes, Y. Sidis, A. Ivanov, C. D. Frost, T. G. Perring, C. T. Lin, D. P. Chen, and B. Keimer, Nat. Phys. **3**, 780 (2007).

[213] G. Xu, J. M. Tranquada, T. G. Perring, G. D. Gu, M. Fujita, and K. Yamada, Phys. Rev. B **76**, 014508 (2007).

[214] K. W. Lee, V. Pardo, and W. E. Pickett, Phys. Rev. B **78**, 174502 (2008).

[215] A. Tamai, A. Y. Ganin, E. Rozbicki, J. Bacsa, W. Meevasana, P. D. C. King, M. Caffio, R. Schaub, S. Margadonna, K. Prassides, et al., Phys. Rev. Lett. **104**, 097002 (2010).

[216] Y. Zhang, F. Chen, C. He, L. X. Yang, B. P. Xie, Y. L. Xie, X. H. Chen, M. Fang, M. Arita, K. Shimada, et al., Phys. Rev. B **82**, 165113 (2010).

[217] T. Kariyado and M. Ogata, J. Phys. Soc. Jpn. **78**, 043708 (2009).

[218] P. Dai, H. A. Mook, G. Aeppli, S. M. Hayden, F. Dovgan, J. Yu, Y. Yanagida, H. Takashima, Y. Inaguma, M. Itoh, et al., Nature **406**, 965 (2000).

[219] J. M. Tranquada, C. H. Lee, K. Yamada, Y. S. Lee, L. P. Regnault, oslash, and H. M. nnow, Phys. Rev. B **69**, 174507 (2004).

[220] B. Lake, G. Aeppli, K. N. Clausen, D. F. McMorrow, K. Lefmann, N. E. Hussey, N. Mangkorntong, M. Nohara, H. Takagi, T. E. Mason, et al., Science **291**, 1759 (2001).

[221] M. Kofu, S. H. Lee, M. Fujita, H. J. Kang, H. Eisaki, and K. Yamada, Phys. Rev. Lett. **102**, 047001 (2009).

[222] J. Wen, Z. Xu, G. Xu, J. M. Tranquada, G. Gu, S. Chang, and H. J. Kang, Phys. Rev. B **78**, 212506 (2008).

[223] S. D. Wilson, S. Li, J. Zhao, G. Mu, H.-H. Wen, J. W. Lynn, P. G. Freeman, L.-P. Regnault, K. Habicht, and P. Dai, PNAS **104**, 15259 (2007).

[224] J. Zhao, L.-P. Regnault, C. Zhang, M. Wang, Z. Li, F. Zhou, Z. Zhao, C. Fang, J. Hu, and P. Dai, Phys. Rev. B **81**, 180505 (2010).

[225] T. Kida, T. Matsunaga, M. Hagiwara, Y. Mizuguchi, Y. Takano, and K. Kindo, J. Phys. Soc. Jpn **78**, 113701 (2009).